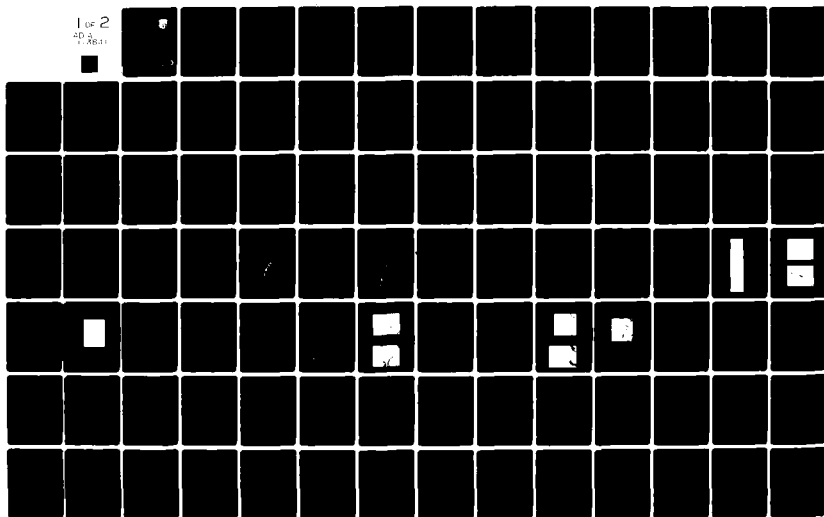


AD-A113 841

SYSTEMS RESEARCH LABS INC DAYTON OH RESEARCH APPLICA--ETC F/G 11/4  
MECHANICAL PROPERTY CHARACTERIZATION AND MODELING OF STRUCTURAL--ETC(U)  
FEB 82 N E ASHBAUGH, H L BERNSTEIN F33615-79-C-5025  
SRL-9799 AFWAL-TR-81-4187 NL

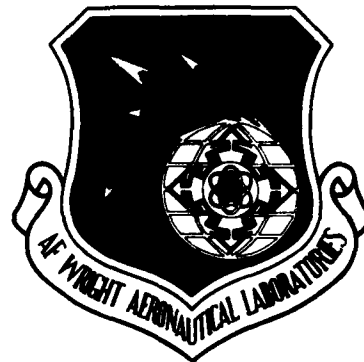
UNCLASSIFIED

1 of 2  
AD-A113 841



AD A113841

AFWAL-TR-81-4187



MECHANICAL PROPERTY CHARACTERIZATION  
AND MODELING OF STRUCTURAL MATERIALS

Noel E. Ashbaugh, Henry L. Bernstein, Bhaskar Majumdar,  
and Jalees Ahmad

Research Applications Division  
Systems Research Laboratories, Inc.  
2800 Indian Ripple Road  
Dayton, OH 45440

February 1982

Final Report for Period June 1979 to May 1981.

Approved for public release; distribution unlimited.

MATERIALS LABORATORY  
AIR FORCE WRIGHT AERONAUTICAL LABORATORIES  
AIR FORCE SYSTEMS COMMAND  
WRIGHT-PATTERSON AIR FORCE BASE, OHIO 45433

DTIC

APR 22 1982

H

DTIC FILE COPY

82 04 22 009

NOTICE

When Government drawings, specifications, or other data are used for any purpose other than in connection with a definitely related Government procurement operation, the United States Government thereby incurs no responsibility nor any obligation whatsoever; and the fact that the government may have formulated, furnished, or in any way supplied the said drawings, specifications, or other data, is not to be regarded by implication or otherwise as in any manner licensing the holder or any other person or corporation, or conveying any rights or permission to manufacture use, or sell any patented invention that may in any way be related thereto.

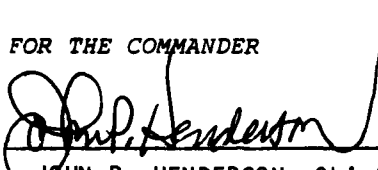
This report has been reviewed by the Office of Public Affairs (ASD/PA) and is releasable to the National Technical Information Service (NTIS). At NTIS, it will be available to the general public, including foreign nations.

This technical report has been reviewed and is approved for publication.



THEODORE NICHOLAS  
Project Engineer  
Metals Behavior Branch

FOR THE COMMANDER



JOHN P. HENDERSON, Chief  
Metals Behavior Branch  
Metals and Ceramics Division

"If your address has changed, if you wish to be removed from our mailing list, or if the addressee is no longer employed by your organization please notify AFWAL/MLLN, W-PAFB, OH 45433 to help us maintain a current mailing list".

Copies of this report should not be returned unless return is required by security considerations, contractual obligations, or notice on a specific document.

Unclassified

SECURITY CLASSIFICATION OF THIS PAGE (When Data Entered)

REPORT DOCUMENTATION PAGE		READ INSTRUCTIONS BEFORE COMPLETING FORM
1. REPORT NUMBER AFWAL-TR-81-4187	2. GOVT ACCESSION NO. AD-A113 841	3. RECIPIENT'S CATALOG NUMBER
4. TITLE (and Subtitle)  MECHANICAL-PROPERTY CHARACTERIZATION AND MODELING OF STRUCTURAL MATERIALS		5. TYPE OF REPORT & PERIOD COVERED Final Report June 1979 - May 1981
		6. PERFORMING ORG. REPORT NUMBER 9799 Final
7. AUTHOR(s) Noel E. Ashbaugh, Henry L. Bernstein, Bhashkar S. Majumdar, and Jalees Ahmad		8. CONTRACT OR GRANT NUMBER(s)  F33615-79-C-5025
9. PERFORMING ORGANIZATION NAME AND ADDRESS Systems Research Laboratories, Inc. 2800 Indian Ripple Road Dayton, OH 45440		10. PROGRAM ELEMENT, PROJECT, TASK AREA & WORK UNIT NUMBERS Prog. Element 61102F Proj. 2307, Task Area 2307P1 Work Unit 2307P112
11. CONTROLLING OFFICE NAME AND ADDRESS Materials Laboratory (AFWAL/MLLN) Air Force Wright Aeronautical Laboratories (AFSC) Wright-Patterson Air Force Base, OH 45433		12. REPORT DATE February 1982
		13. NUMBER OF PAGES 131
14. MONITORING AGENCY NAME & ADDRESS (if different from Controlling Office)		15. SECURITY CLASS. (of this report)  UNCLASSIFIED
		15a. DECLASSIFICATION/DOWNGRADING SCHEDULE
16. DISTRIBUTION STATEMENT (of this Report)  Approved for public release, distribution unlimited.		
17. DISTRIBUTION STATEMENT (of the abstract entered in Block 20, if different from Report)		
18. SUPPLEMENTARY NOTES		
19. KEY WORDS (Continue on reverse side if necessary and identify by block number) Fracture mechanics, fatigue-crack propagation, creep-fatigue interaction, life predictions, crack growth under spectrum loads, creep crack growth, finite- element analysis, elevated-temperature crack-growth testing, compliance, stress- intensity factor, oxidation, crack-growth mechanisms.		
20. ABSTRACT (Continue on reverse side if necessary and identify by block number) A comprehensive research and development program was conducted to investigate crack-growth behavior, to develop predictive models of crack-growth rates, and to generate data on mechanical properties of engine-disk materials at room and elevated temperatures. The program consisted of three concurrent tasks:  <ul style="list-style-type: none"> <li>• Research on crack-growth behavior,</li> <li>• Experimental investigations for determination of mechanical properties and reliability of structural materials.</li> </ul>		

DD FORM 1 JAN 73 1473

EDITION OF 1 NOV 65 IS OBSOLETE

Unclassified

SECURITY CLASSIFICATION OF THIS PAGE (When Data Entered)

Unclassified

SECURITY CLASSIFICATION OF THIS PAGE(When Data Entered)

20. Abstract Continued

Development, upgrading, and maintenance of the AFWAL Mechanical Test Facility.

In the first of these tasks, fundamental research was conducted on the crack-growth behavior of engine-disk nickel-base superalloys operating in the temperature range 538-760°C. Specific experimental and analytical research consisted of the effects of sustained load upon crack growth, crack growth in deleterious environments, and crack initiation and growth of short cracks. Crack-growth-rate models were developed based upon experimental results and upon analytical characterization of fundamental processes which occur during crack growth. To guide the development of the models and to aid the understanding of crack-growth behavior, extensive use was made of finite-element analysis, data-reduction schemes, and fractography and metallurgical analysis of crack-growth mechanisms.

In the second task extensive mechanical-property data were generated as required by on-going AFWAL programs. The tests included uniaxial tension, compression, bend, creep fatigue, low-cycle fatigue, crack initiation, sustained-load crack growth, and fatigue-crack growth. The materials which were tested included nickel-base superalloys, titanium, aluminum, and other structural materials. The tests were performed under conditions typical for engine disks in Air Force engines with temperatures up to 760°C (1400°F), controlled environments, and various loading spectra. Fractographic and metallurgical analyses were carried out to determine the mechanisms controlling the mechanical behavior.

Unclassified

SECURITY CLASSIFICATION OF THIS PAGE(When Data Entered)

## FOREWORD

The work described in this report was performed at the Metals Behavior Branch, Metals and Ceramics Division, Materials Laboratory, Air Force Wright Aeronautical Laboratories (AFWAL/MLLN), under Contract F33615-79-C-5025, "Mechanical Property Characterization and Modeling of Structural Materials." The contract was administered under the direction of AFWAL by Dr. Theodore Nicholas (MLLN). The program was conducted by the Research Applications Division, Systems Research Laboratories, Inc., Dayton, OH, with Dr. Noel Ashbaugh as the Principal Investigator.

The investigations of crack-growth behavior and modeling were conducted by Drs. Noel Ashbaugh, Jalees Ahmad, and Bhaskar Majumdar and by Mr. Henry Bernstein. Generation of data on mechanical behavior was accomplished under the direction of Messrs. Walter Tripp and Earnest Keppler by Messrs. Richard Klinger, James Paine, Charles Bell, George Mornhinweg, Douglas Deaton, Mark Rowe, Robert Lewis, Dale Opela, and Dennis Mummert. The work was performed during the period June 1979 to May 1981.

Accession For	
NTIS CRA&I	<input checked="checked" type="checkbox"/>
DTIC TAB	<input type="checkbox"/>
Unannounced	<input type="checkbox"/>
Justification	
By	
Distribution/	
Availability Codes	
Dist	Avail and/or Special



## TABLE OF CONTENTS

SECTION	PAGE
I INTRODUCTION	1
II RESEARCH ON CRACK-GROWTH BEHAVIOR	3
1. CREEP CRACK GROWTH IN SIDE-GROOVED SPECIMENS OF IN100	3
2. OXIDATION AND CRACK-GROWTH INTERACTION	4
a. Literature Survey on Creep Crack Growth and Oxidation	4
b. An Adsorption Model for the Effect of Environment Upon High-Temperature Crack Growth	16
c. Experimental Results for Baseline Creep Crack Growth (CCG) in Inconel 718	29
3. EVALUATION OF ENVIRONMENTAL AND WAVESHAPE EFFECTS	38
a. Experimental Fatigue-Crack-Growth Rates	38
b. Fractography	41
4. PRELIMINARY STUDIES ON THE PROPAGATION OF SHORT CRACKS AT NOTCHES	44
5. EVALUATION OF THRESHOLD TEST PROCEDURE	58
6. STUDY OF CRACK-GROWTH RESISTANCE USING POLYCARBONATE AS A MODEL MATERIAL	62
7. CHARACTERIZATION OF STABLE CRACK GROWTH USING POLYCARBONATE AS A MODEL MATERIAL	64
8. FINITE-ELEMENT ANALYSIS OF TEST SPECIMENS	69
a. Ring and Partial Ring Geometries	69
b. Keyhole and Wide-Notch Specimens	72
c. Three-Dimensional Results for Some Test-Specimen Configurations	72
d. Analytical Modeling of the Mechanical Aspects of Fatigue Crack Growth	76

## TABLE OF CONTENTS (Concluded)

SECTION	PAGE
III EXPERIMENTAL INVESTIGATIONS TO DETERMINE MECHANICAL PROPERTIES AND RELIABILITY OF STRUCTURAL MATERIALS	77
1. TYPES OF TESTS	77
2. INVESTIGATIONS SUPPORTED BY DATA OBTAINED IN FACILITY	78
3. MODULUS AND MECHANICAL PROPERTIES OF IN100 AT ELEVATED TEMPERATURES	83
IV DEVELOPMENT OF TESTING TECHNIQUES, EQUIPMENT, AND INSTRUMENTATION	87
1. AUTOMATION OF CREEP FRAME FOR SUSTAINED-CRACK-GROWTH TESTS	87
2. SOFTWARE DEVELOPMENT FOR COMPUTER DATA ACQUISITION, AUTOMATED CONTROL OF CRACK-GROWTH TESTS, AND DATA REDUCTION	89
a. Data Acquisition to Determine Compliance and Crack Length	90
b. Automated Computer Control of a Test System	91
c. Modifications to the Automatic Computer-Control Program	98
d. Monitoring and Control System	99
e. Crack-Growth Data Reduction	100
3. IMPROVED LABORATORY EQUIPMENT AND TEST PROCEDURES	102
a. Centorr Vacuum System	102
b. Evaluation of Schenck Machine and Development of Instrumentation for Threshold Tests	109
c. Electric-Potential Technique	110
d. Modulus Evaluation at Elevated Temperatures	114
e. Fatigue-Crack Extension of Tunneled Crack Formed Under Sustained Load	115
f. Fabrication of Environment Chamber	117
REFERENCES	119



## LIST OF ILLUSTRATIONS

FIGURE		PAGE
1	Diagram of Cavity Growth by Removal of Atoms from Cavity Surface and Deposition into Adjacent Boundaries; Growth is Accommodated by Rigid Body Displacement of the Two Half Crystals.	12
2	Diagram of Crack-Growth Rates in Air and Vacuum as a Function of Stress Intensity Factor.	17
3	Creep Crack Growth in Inconel 718 at 650°C.	26
4	Crack Propagation in Astroloy for 15-min. Hold Time at 650°C.	27
5	Fatigue-Crack Growth in Astroloy at 1 Hz.	28
6	Fatigue-Crack Propagation in Inconel 718 at 650°C, 1 Hz.	30
7	Fatigue-Crack Propagation in Inconel 718 at 650°C, 0.1 Hz.	31
8	Creep-Crack-Growth Rate in Inconel 718 at 650°C Using Optical Surface Crack-Length Measurements.	34
9	Creep-Crack-Growth Rate in Inconel 718 at 650°C Using Compliance Technique for Crack-Length Determination.	35
10	Creep-Crack-Growth Rate in Inconel 718 at 650°C Using Surface Measurements Where Crack Length is Longer Than for Results in Fig. 8.	36
11	Creep-Crack-Growth Rate in a Second Specimen of Inconel 718 at 650°C Using Surface Measurements.	37
12	Specimen 7ENWS-2 Cycled Alternately at 1/6 Hz and 5 Hz at 1350°F.	42
13	Higher-Magnification Micrograph from Region D (5Hz) in Figure 12.	43
14	Higher-Magnification Micrograph from Region E (1/6 Hz) in Figure 12.	43

# LIST OF ILLUSTRATIONS (Continued)

FIGURE		PAGE
15	Boundary Between Regions E and F in Figure 12.	45
16	Keyhole Specimen for Short-Crack Investigation (Dimensions in Inches).	47
17	Fatigue-Crack-Growth Rate for a Long Crack in 7075-T651 Aluminum.	49
18	SEM Micrograph of the Fracture Surface of Long-Crack Specimen at a Distance of 12 mm From the Machined Notch.	50
19	SEM Micrograph of the Fracture Surface of a Long-Crack Specimen at a Distance of 14.5 mm From the Machined Notch.	50
20	Schematic Diagram of Fracture Surface for Short-Crack Specimen.	52
21	Enlarged Sketch of Fatigue-Fracture Region from which SEM Micrographs were Taken.	52
22	SEM Micrograph of Fracture Surface of Short-Crack Specimen at Region ⑦ in Figure 21.	53
23	SEM Micrograph of Fracture Surface of Short-Crack Specimen at Region ⑧ in Figure 21.	53
24	SEM Micrograph of Fracture Surface of Short-Crack Specimen at Region ⑨ in Figure 21.	54
25	Wide-Notch Specimen (Dimensions in Inches).	57
26	Threshold Fatigue-Crack-Growth Rates under Decreasing-K Conditions for 2219-T851 Aluminum in Laboratory Air at 40 Hz.	60
27	Threshold and Higher Fatigue-Crack-Growth Rates under Increasing-K Conditions for 2219-T851 Aluminum in Laboratory Air at 40 Hz.	61
28	Plot of Time Rate of Change of Strain Energy Per Unit Thickness as a Function of Crack Length for Various Constant Load-Displacement Rates.	67
29	Log-Log Plot of Crack-Growth Rate as a Function of $C^*$ for Polycarbonate Three-Point-Bend Tests.	68

# LIST OF ILLUSTRATIONS (Concluded)

FIGURE		PAGE
30	Schematic Diagram of Rings and Partial Rings with Cracks.	70
31	Tensile Tests of IN100 at 1350°F and at Various Strain Rates.	86
32	Block Diagram of Major Steps in Initializing Control Program.	94
33	Block Diagram of Major Steps in Feedback Loop of Control Program.	95
34	Plot of Crack-Length Versus Cycle-Count Data Listed in Table 15.	103
35	Plot of $da/dN$ versus $\Delta K$ for a Nine-Point Least-Squares Fit of Data in Table 15.	105
36	Plot of $da/dN$ versus $\Delta K$ for Secant Method of Data Reduction in Table 15.	107
37	Specimen Geometry and Lead Attachments for Measuring Potential as a Function of Crack Length (Dimensions in inches).	111
38	Circuit and Instrumentation Used for Potential Measurements.	112
39	Calibration Curve of Total Crack Length as a Function of Electric Potential.	113
40	Measurement of Load-Line Deflection on C-Specimens.	116

# LIST OF TABLES

TABLE		PAGE
1	CCG Tests of Inconel 718 at 650°C - Precracking At Room Temperature, R = 0.1, $\nu$ = 10 Hz.	32
2	Preliminary Values of FCGR for IN100 in Laboratory Air and Dry Argon.	39
3	Comparison of Results for Short- and Long-Crack Fatigue-Crack-Growth Rates in 7075-T651 Aluminum.	55
4	Threshold K Obtained for 2219-T851 Aluminum in the ASTM Round-Robin Test-Procedure Evaluation.	63
5	PC Test Matrix for Crack-Growth Characterization.	65
6	Stress-Intensity Factors for a Wide-Notch Specimen.	73
7	Results for Three-Point-Bend Specimen (Three Dimensional).	74
8	Results for Ring Tension Specimen with Two Cracks (Three Dimensional).	75
9	Young's Modulus for IN100 at 0.004 in./in./min. Nominal Strain Rate.	84
10	Mechanical Properties of IN100 at 1350°F.	85
11	Compliance Data for Compact-Tension Specimen 7-5, IN100.	88
12	Mean and Standard Deviation of Crack Length Determined from Load-COD Data.	92
13	Optical and Compliance Crack Lengths for Trial Specimen Tested under Computer Control.	97
14	Computer Data-Reduction Programs.	101
15	Input Crack-Growth Data.	104
16	CGR Data Reduced using Nine-Point Least-Squares Fit.	106
17	CGR Data Reduced using Secant Method.	108

## SECTION I

### INTRODUCTION

If new materials are to be applied successfully in Air Force systems, the characteristics of these materials must be evaluated and assessed under conditions encountered in service. In addition, due to the increasing costs associated with the development and acquisition of advanced systems and also with the modification and maintenance of current systems, the Air Force has placed increased emphasis upon evaluating the durability of aircraft components in the airframe and in gas-turbine engines. As a result, the Materials Laboratory of the Air Force Wright Aeronautical Laboratories (AFWAL) is engaged in a number of research programs with the fundamental aim being to provide a technical assessment of the characteristics of materials which are used in airframes and in gas-turbine engines.

To aid in the accomplishment of this assessment, the following three tasks were performed by SRL under Contract F33615-79-C-5025 to the Metals and Ceramics Division (MLLN) of AFWAL:

- Research on crack-growth behavior in engine materials at elevated temperatures
- Experimental investigations to determine the mechanical properties and reliability of structural materials
- Development of test techniques and instrumentation applicable to life-prediction methodology.

New materials having superior mechanical properties are being developed to withstand more severe in-service conditions, for example, higher operating temperatures in aircraft engines which improve performance and operating efficiency. In order to make an accurate assessment of material behavior, the materials must be subjected to specialized and unique laboratory tests. In the first task fundamental research was conducted

on the crack-growth behavior of engine-disk nickel-base superalloys operating in the temperature range 538-760°C. The specific experimental and analytical research consisted of determining the effects of sustained load upon crack growth, the interaction of the sustained load and variable-amplitude load, and crack growth under various environmental conditions. The parameters which were evaluated for the characterization of crack-growth behavior were K, the J-integral, and  $C^*$ . Finite-element analysis was employed to analyze various test-specimen geometries and to aid in the development of crack-growth models. Fractography and metallurgical analysis were used in the characterization of crack-growth behavior.

In the third task advanced test techniques were developed to investigate crack-growth behavior, fatigue, and fracture. Specific accomplishments included crack-length determination by COD measurements, evaluation of electric-potential methods, improved compliance techniques, creep-facility updating, incorporation of the computer monitoring system, expansion of the computer signal-generator system including interactive capabilities, design of the environmental chamber, and design and fabrication of versatile resistive furnaces.

SECTION II  
RESEARCH ON CRACK-GROWTH BEHAVIOR

1. CREEP CRACK GROWTH IN SIDE-GROOVED SPECIMENS OF IN100

The object of this investigation was to determine the principal parameters which affect crack growth at elevated temperatures and under sustained loads. For some materials the crack-growth behavior is commonly called creep crack growth (CCG). The results provide a better understanding for the development of crack-growth models which improve the capability of predicting crack growth in materials which are used under extreme operating conditions such as those produced in gas-turbine engines.

Crack-growth behavior was investigated in a nickel-base superalloy (IN100) at 732°C (1350°F) in laboratory air under sustained load. The tests were conducted on side-grooved compact-type specimens. One of the purposes of the study was to evaluate the effect of the through-the-thickness stress distribution upon crack-growth behavior in grooved specimens by comparing it with the crack growth in smooth-sided specimens which have been studied extensively in other investigations. These previous studies have shown that the crack propagates faster in the center of a specimen than near the surface. Also in this study the effects of crack orientation and net thickness between the side grooves were evaluated.

Crack-growth rates were determined for several initial values of the stress-intensity factor and for various thicknesses. Since no tunneling occurred in the side-grooved specimens, the cause of tunneling in the smoothed-sided specimens was primarily attributed to the through-the-thickness stress distribution in the specimen ahead of the crack front. The crack-growth rates as a function of stress-intensity factor showed a slight dependence upon thickness and were independent of crack orientation. Also the rates at the same stress-intensity level in the grooved specimens were faster than the rates in the smooth specimens, which indicated that the "plane-stress region" near the sides of the smooth specimen tended to

2.

retard the crack growth in the interior of the specimen. A model for the crack-growth rates as a function of stress-intensity factor was developed. The model incorporated the dependence of growth rates upon initial loading conditions, and the effect of thickness and prior loading history could be taken into account in the model. The effect of overload ratios was considered. The results of this investigation were presented at the 14th National Symposium of Fracture Mechanics at the University of California at Los Angeles in June 1981 and were submitted to the American Society for Testing and Materials for publication in a Special Technical Publication.

## 2. OXIDATION AND CRACK-GROWTH INTERACTION

### a. Literature Survey on Creep Crack Growth and Oxidation

The environmental effects upon CCG have not been studied in detail. Currently, the literature mainly consists of CCG data in laboratory air and inert environments. Mathematical models for the effect of environment upon CCG were not found. Some degree of mathematical modeling was found for the related areas of stress-corrosion cracking (SCC) and environmental effects upon fatigue-crack growth (FCG).

CCG data for the effect of oxidation upon Ni-base superalloys was found in the work of Floreen and Kane,<sup>1</sup> Sadananda and Shahinian,<sup>2</sup> and Pelloux and Huang.<sup>3</sup> These studies showed that air accelerated the CCG rate (CCGR) from zero to 100 times, depending upon the material and temperature. At higher temperatures the effect of air was less. The component in the air that is responsible for this acceleration was found by Floreen and Kane<sup>4</sup> to be oxygen for FCG in Inconel 718 at 650°C (1200°F). Therefore, it is reasonable to assume that oxygen is also the deleterious component in CCG.

The effect of oxidation upon CCG is complicated by the fact that oxidation may affect the creep properties. Menon<sup>5</sup> found that a vacuum decelerated the minimum creep rate and increased the time to rupture for René 95 at



650°C (1200°F). However, Shahinian<sup>6</sup> found little environmental effect for smooth creep specimens but a very large reduction in rupture time for notched bars in a vacuum. A review paper by Cook and Skelton<sup>7</sup> discusses in more detail the effect of environment upon mechanical properties at elevated temperature. The conclusion to be drawn from this evidence is that CCG tests conducted in a vacuum do not necessarily isolate the creep component which would be obtained in an analogous air test because the creep behavior is altered by the inert environment.

Fractographic evidence<sup>1-3,8-9</sup> shows that CCG is entirely intergranular, both in air and inert environments, regardless of temperature. Floreen and Kane<sup>1</sup> found that in Inconel 718 the grain boundaries (gb) were covered by small cavities which were analogous to ductile rupture by void growth. Pelloux and Huang<sup>3</sup> found the same fracture appearance in Astroloy and found that the voids were centered on second-phase particles on the gb. In an earlier paper, Floreen<sup>8</sup> reported that CCG took place by nucleating gb microcracks ahead of the crack tip, followed by linking up with the main crack. The metallographic evidence shows that CCG is a process of separating the grain boundaries, the most likely mechanism being the nucleation and growth of gb cavities or voids. The exact role of oxygen in this process is unclear.

Models for the effect of oxygen upon CCG can be divided into qualitative models and quantitative models. Qualitative models relate the effects of oxygen in a descriptive fashion. The possible effects of oxygen are fairly well agreed upon in the literature. Disagreements arise over which specific mechanism is operating in a given material. Quantitative or mathematical models attempt to express these qualitative ideas in an exact, numerical fashion.

The qualitative models involve getting oxygen to the crack tip, the effect of an external scale, and internal oxidation. The processes of getting oxygen to the crack tip involves transporting the oxygen molecule down the crack to the crack tip, the adsorption (or stick) of the molecule to the crack-tip surface, and the dissociation of the molecule to atomic oxygen--  
 $O_2 \rightarrow 2O$ .

2.

Once atomic oxygen is present, an external oxide scale can form on the crack-tip surface. This scale can influence the CCGR in many ways, but the most likely way is by the cracking of the scale since oxide scales are usually brittle. The crack in the scale acts as a point of stress concentration causing crack advance until arrested by plastic blunting. The crack also exposes a fresh metal surface to the environment, which rapidly oxidizes it and thereby advances the crack.

In addition to forming an external scale, oxidation influences the base metal in three ways--through vacancy generation, loss of alloying elements, and growth stresses. Whenever a metal atom leaves the base metal to enter the scale, it leaves behind a vacancy at the metal-scale interface. These vacancies agglomerate to form voids at this interface and at gb's, thus contributing to creep damage.

When an alloy is oxidized, oxides which form are among the most stable. The alloying elements, especially Cr and Al, are usually stronger oxide formers than the base metal and, therefore, oxidize first. This selective oxidation weakens the metal matrix by removing strengthening elements, thus making deformation easier.

The crystallographic structure of the oxide and the base metal rarely match, and this mismatch causes stresses to build up. These growth stresses add to the applied stresses from external loads.

It is also theorized that the oxide scale strengthens the material. The oxide may bridge the crack surfaces and support some of the load; in addition, the oxide may blunt the crack tip, thus reducing the stress concentration.

It should be noted that some of these models are not compatible with one another, and some may seem too simplistic or unrealistic. These models are those suggested in the literature and for a given material most of them are not applicable.

Atomic oxygen atoms can also diffuse into the metal ahead of the crack tip. The most rapid path for diffusion is along a gb. As the oxygen diffuses into the metal, it reacts with the alloying elements to form the most stable oxides. When the oxide reaches its solubility limit within the metal matrix, it precipitates out as a second-phase particle.

Oxygen in the gb accelerates CCG by weakening the gb. This weakening occurs by: (1) lowering the surface energy, making it less energetic in separating the gb, (2) assisting the nucleation of voids by decreasing the radius at which an embryonic void becomes stable, (3) assisting the growth of voids by producing vacancies through internal oxidation, and (4) depleting the gb and adjacent metal matrix of the strengthening elements.

The formation of a second phase, or oxide, on the gb promotes cavity formation. The oxide may debond from the gb, thus initiating a cavity or void similar to ductile tearing, or the oxide may crack, thus producing a stress concentration at its sides and initiating a cavity. Finally, the size change associated with the formation of the oxide may act to wedge open the gb.

The available mathematical models may be placed into two groups--empirical and semi-empirical models. The models presented here are the best that could be found. No models for the effect of environment upon CCG were found. Consequently, models from the literature on the environmental effects on fatigue-crack growth (FCG), stress-corrosion cracking (SCC), and hydrogen embrittlement (HE) are presented and adapted to CCG. Generally, the models are crude or merely mathematical expressions of phenomena that may be important to CCG. It seems to the reviewer that more sophisticated models for SCC and HE should be available, although none were found; discussions with researchers in these fields indicated that more sophisticated models do not exist.

The empirical approach to modeling begins with subdividing the creep-crack-growth rate (CCGR),  $\dot{a}$ , in air into an inert and an environmental component

$$\dot{a} \text{ (air)} = \dot{a} \text{ (inert)} + \dot{a} \text{ (envir.)} \quad (1a)$$

$$\log \dot{a} \text{ (air)} = \log \dot{a} \text{ (inert)} + \log \dot{a} \text{ (envir.)} \quad (1b)$$

Equation (1b) is preferable because available data indicate that  $\dot{a} \text{ (envir.)} \gg \dot{a} \text{ (inert)}$ , thus rendering Eq. (1a) of little value. Once this separation is made, the dependence of the environmental component upon stress intensity, temperature, and oxygen pressure can be determined empirically from experimental data. Two possible forms of these dependences have been suggested in the literature.<sup>10</sup> One form is that the environmental component is equivalent to the general oxidation rate. The other form is that this component is simply a multiplicative constant, C, to the inert component

$$\dot{a} \text{ (envir.)} = C \times \dot{a} \text{ (inert)}$$

Semi-empirical models combine theoretical formulations with experimental curve fitting. These models can be divided into adsorption models, surface-reaction models, and diffusion models.

In adsorption models the rate-limiting step in CCG is the formation of an adsorbed layer of molecules on the surface of the crack-growth increment. How this adsorbed layer influences crack growth is not clear. It can be argued that the adsorbed layer has no effect because a fresh surface must first be created before adsorption can occur. The simplest approach to adsorption is to calculate the time required to form an adsorbed monolayer upon a surface.<sup>10</sup> From the kinetic theory of gases, this time is

$$t = \frac{D\sqrt{MTR}}{nAP} \quad (2)$$

where t is time, D is planar atomic density, M is molecular weight of the gas, T is absolute temperature, R is the gas constant, n is the number of atoms per gas molecule, A is Avogadro's number, and P is the partial pressure of the gas. In order to relate Eq. (2) to the CCGR, it is necessary to assume that this rate is equal to the time required to form an adsorbed monolayer. When this equating is done for FCG data, it is found that the

time for adsorption is much faster than the FCG rates. This discrepancy may be due to restriction of the flow near the crack tip and/or reaction of the environment to the crack walls. Modification to the simple model can be made along these lines.

A very sophisticated modification to the adsorption model has been made by Wei, et al.<sup>11</sup> They considered the gas flow near the crack tip to occur by molecular flow, or Knudsen flow, and attributed the decrease in gas pressure at the crack tip to adsorption. Assuming linear surface coverage and a sticking coefficient of one, they derived an equation for the fraction of surface cover,  $\theta$ ,

$$\theta \cong \frac{FPT}{SNRT} \quad (3)$$

where P is pressure, t is time, S is surface area of new crack per cycle, N is density of surface sites, R is the gas constant, and T is the absolute temperature. F is the Knudsen flow parameter and is given by

$$F = 8.72 \times 10^4 \beta \sigma_0 / E^2 B \ell \sqrt{T/M}$$

where  $\beta$  is an empirical constant,  $\sigma_0$  is the yield stress, E is the elastic modulus, B is the specimen thickness,  $\ell$  is the length of the Knudsen flow regime, and M is the molecular weight of the gas. In order to apply Eq. (3) to FCG, it is necessary to assume that

$$\frac{da}{dN} = C \cdot \theta \cdot \Delta a \quad (4)$$

where C is a constant and  $\Delta a$  is the increment of crack advance. Scaling Eqs. (3) and (4) to FCG for 2219-T851 aluminum in water vapor, the correct dependence of FCG upon the partial pressure of water vapor was obtained.

One possible effect of adsorption is a lowering of the surface energy, which renders fracture less energetic. However, since Duquette and Gell<sup>12</sup> showed plastic energy for fracture to be so much greater than the energy of adsorption, this consideration is negligible.

In surface-reaction models, the rate-limiting step in CCG is a chemical reaction which occurs on the surface of the crack tip. None of these models has been formulated into a crack-growth equation as yet, but the chemical-reaction kinetics have been enumerated.

Simmons, Pao, and Wei<sup>13</sup> have studied the Stage II SCC behavior of 4340 steel in water vapor. They determined that dissociation of the water molecule, the water reaction  $\text{H}_2\text{O} \rightarrow 2\text{H}^+ + \text{O}^{--}$ , was the rate-limiting step. This result was found by measuring the fraction of surface coverage by water as a function of time, temperature, and water-vapor pressure. These measurements were made by surface-chemistry experiments. The results of the chemistry data were fit to a linear surface-coverage equation

$$\theta = \beta P t \exp (-Q/RT) \quad (5)$$

where  $\theta$  is the fraction of surface coverage,  $\beta$  is a constant,  $P$  is pressure,  $t$  is time,  $Q$  is activation energy,  $R$  is the gas constant, and  $T$  is absolute temperature. Since the activation energy of this surface reaction is the same as that for SCC, the water reaction was identified as the rate-limiting step.

The kinetics of oxidation are generally described in terms of empirical equations

$$\xi^2 = kt + C \quad (6a)$$

$$\xi = k \ln t + C \quad (6b)$$

$$\xi^n = kt + C \quad (6c)$$

where  $\xi$  is the thickness of the oxide scale,  $t$  is time, and  $k$ ,  $C$ , and  $n$  are constants. Equation (6a) is the well-known parabolic rate law and applies to thick scales or to any situation where diffusion is the rate-limiting step. Equation (6b) is a logarithmic rate law and usually applies to thin films. Equation (6c) is a general rate law that can be fit to experimental data. Exactly how to incorporate these equations into a CCG model is unclear, but these are some of the mathematical expressions that may have to be included in such a model.

One semi-empirical model for SCC is based upon the diffusion of a gaseous species ahead of the crack tip. This model by Bania and Antolovich<sup>14</sup> holds that the activation energy for diffusion is reduced by the dilation of the metal matrix at the crack tip due to the large hydrostatic stresses at the crack tip. The reduction in activation is found to depend upon the stress intensity,  $K$ , and the elastic modulus,  $E$ , and is proportional to  $K^2/E$ . Since diffusion is the rate-limiting step, the activation energy for SCC is the same as that for diffusion. Therefore, the proposed crack-growth equation is

$$\dot{a} = AK^n \exp \frac{Q_0 - BK^2/E}{RT} \quad (7)$$

where  $\dot{a}$  is the crack-growth rate;  $A$ ,  $n$ ,  $Q_0$ , and  $B$  are constants; and  $K$ ,  $E$ ,  $R$  and  $T$  have been defined previously. Fitting Eq. (7) to SCC data for Ti-6-4 in 3.5% NaCl resulted in good predictions for the crack-growth rate.

Since cavitation on gb has been associated with CCG in some nickel-base superalloys, the literature was reviewed in search of models for CCG by this mechanism. Models by Raj and Baik<sup>15</sup> and Miller and Pilkington<sup>16</sup> for the growth of cavities in creep specimens have been used to predict the growth and coalescence of cavities ahead of crack tips. By combining the cavity-growth model, the stress field ahead of the crack tip, and the failure criterion of cavity linkup, the CCG behavior was calculated. The cavity-growth models can be divided into two approaches--diffusional growth and deformation growth. The diffusion-growth models are based upon the concept of Balluffi and Seigle<sup>17</sup> and the model of Hull and Rimmer.<sup>18</sup> Referring to Fig. 1, a gb cavity subjected to a tensile stress will grow by the diffusion of atoms from the cavity surface into the gb. By widening the gb, the tensile stress produces a gradient in chemical potential which is the driving force for this diffusion. The model of Hull and Rimmer is based upon the assumptions that the cavity is a sphere, that all deformation occurs in the gb (rigid crystals), and that diffusion through the crystal lattice is negligible compared to surface diffusion. The rate of void

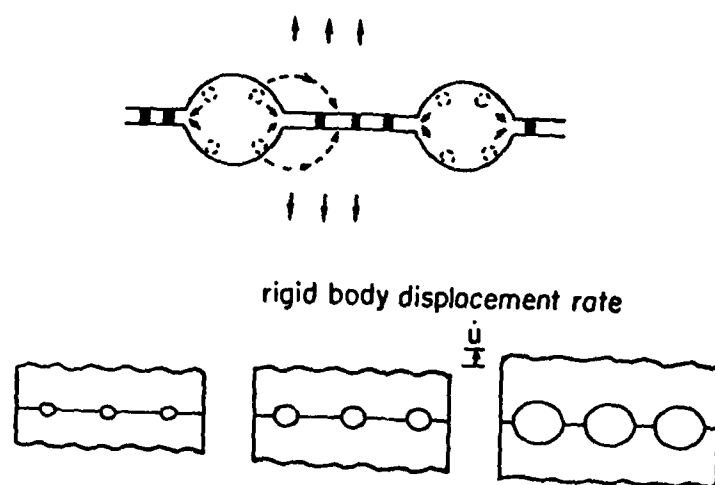


Figure 1. Diagram of Cavity Growth by Removal of Atoms from Cavity Surface and Deposition into Adjacent Boundaries; Growth is Accommodated by Rigid-Body Displacement of the Two Half Crystals [from Raj and Baik<sup>15</sup>]



growth is derived as

$$\frac{d\rho}{dt} = \frac{2\pi\Omega(D_g\delta_z)\sigma - P - 2\gamma/\rho}{kT\lambda\rho} \quad (8)$$

where  $\rho$  is the void radius,  $t$  is time,  $\Omega$  is the atomic volume,  $D_g\delta_z$  is the gb diffusion constant,  $\gamma$  is the tensile stress,  $P$  is the hydrostatic stress,  $\sigma$  is the surface tension,  $k$  is Boltzmann's constant,  $T$  is the absolute temperature, and  $\lambda$  is the cavity spacing. Modifications to the basic model of Hull and Rimmer have been made by Raj, *et al.*,<sup>19,20</sup> for cavities having non-equilibrium shapes. Their modifications have the same form as Eq. (8).

The deformation growth models are based upon enlarging the cavity by creep flow of the surrounding matrix. Different approaches to the continuum-mechanics problem of the change of shape of a creeping hole lead to the different models. The model of Hancock<sup>21</sup> will be discussed because it has been used to predict CCG. The model takes an approximate deformation plasticity solution of McClintock and Argon<sup>22</sup> for the plastic deformation of a circular hole and transforms it to creep behavior by use of a power-law deformation plasticity to power-law creep correspondence principle, similar to the correspondence principle of linear viscoelasticity. While not rigorously valid, this procedure is expected to yield reasonable results. Although the equations predict that the cavities grow into a ellipsoid, it is assumed that they retain a spherical shape. The model predicts the rate of cavity growth as:

$$\frac{d\rho}{dt} = \rho A D_V \frac{\mu b}{kT} \left( \frac{\sigma}{\mu} \right)^n \quad (9)$$

where  $\rho$ ,  $t$ ,  $k$ ,  $T$ , and  $\sigma$  are as before;  $A$  and  $n$  are the constants in the power-law creep equation,  $\dot{\epsilon} = A \sigma^n$ ;  $D_V$  is the volume diffusion coefficient;  $\mu$  is the shear modulus; and  $b$  is the Burger's vector. The most serious drawback to the model is that large spherical cavities deform into ellipsoids, as Hancock points out, but the model must assume that they retain a spherical shape in order to have failure by cavity linkup.

A combination of the diffusion and deformation models has been developed by Needleman and Rice.<sup>23</sup> In their model, diffusion dominates the growth when the edges of the cavities are far apart. As the edges move closer together, deformation becomes more important until it controls the growth when the edges are near each other. Unfortunately, their equations must be solved numerically using a finite-element scheme, and a closed-form solution is not available.

To model CCG using cavity-growth models, it is necessary to use the stress field ahead of the crack and calculate the time to cavity linkup. Raj and Baik have done this using a computer program to generate a numerical solution. They obtained an upper and lower bound for the CCGR which agreed well with data on Inconel 718. However, the bounds encompassed two to four decades of CCGR. Miller and Pilkington used both diffusion and deformation cavity-growth models to predict the CCGR. The CCGR,  $\dot{a}$ , was expressed as

$$\dot{a} = \frac{-d}{\lambda} \frac{dx}{dt} \quad (10)$$

where  $d/\lambda$  is the number of cavities per grain and  $x$  is distance. The elastic stress distribution is integrated over each grain to produce an average stress per grain as a function of  $x$ . This stress and Eq. (10) are put into the cavity-growth equation and integrated to give the CCGR as a function of  $K$ . This procedure results in a closed-form solution for the CCGR. They found that the deformation cavity-growth model of Hancock produced good agreement with CCG data for a Cr-Mo-V steel.

Unfortunately, none of these approaches includes environmental effects. The cavity-growth models upon which they are based do not consider the environment because cavity growth occurs in the interior of a metal, which is not exposed to the environment. Consequently, it is impossible for these CCG models to have an environmental component. That such a component is required is obvious from the fact that laboratory air can accelerate the CCGR by two orders of magnitude from that in a vacuum.<sup>24</sup>

## The conclusions

- (1) An air environment, as compared to an inert environment, accelerates the creep-crack-growth rate from zero to 100 times, depending upon the material and temperature.
- (2) Testing in an inert environment may not isolate the creep component in an air test.
- (3) Creep crack growth is intergranular at all temperatures and environments; therefore, CCG is a process of decohesion of the grain boundaries.
- (4) The same fracture-surface appearance is observed in both air and vacuum environments. The grain boundaries are covered by a network of voids. Therefore, the same fracture mechanism is operating in both air and vacuum.
- (5) The acceleration of cavity growth due to environment can be caused by
  - (i) oxygen atoms stabilizing cavities at smaller sizes,
  - (ii) oxygen nucleating cavities, thereby reducing the cavity spacing,
  - (iii) oxidation producing vacancies which enlarge the cavity,
  - (iv) oxygen lowering the surface energy of the gb, and
  - (v) oxygen depleting the gb and adjacent metal matrix of strengthening elements, thereby making creep flow easier.The exact cause or combination of causes can only be determined by further research.

- (6) The exact role of oxygen is unclear.
- (7) Possible effects of oxygen have been delineated in the literature.
- (8) No mathematical models for the effect of oxygen upon CCG were found. Models for related phenomena are in an initial phase of development.

b. An Adsorption Model for the Effect of Environment Upon High-Temperature Crack Growth

It is well known that a deleterious gas environment (such as those containing oxygen, hydrogen, chlorine) generally increases the crack-growth rate. Not so well understood is the mechanism of interaction of the environment with the crack tip. Considerable research has been done regarding the effect of hydrogen upon threshold crack-growth characteristics of steels. However, the effect of environmental interaction upon crack-growth behavior at elevated temperatures in nickel-base superalloys has been largely unexplored. Only scattered data are available in the literature.

A common approach used in the literature is to express the high-temperature environmental effect as the change in  $da/dN$  or  $da/dt$  at a given  $\Delta K$  or  $K$ , due to the presence of oxygen. It is implicitly assumed, and probably justifiably so, that oxygen is the deleterious species. Thus, one writes

$$\left. \frac{da}{dN} \right|_{\text{air}} = \alpha \left. \frac{da}{dN} \right|_{\text{vacuum}}$$

$$\left. \frac{da}{dt} \right|_{\text{air}} = \beta \left. \frac{da}{dt} \right|_{\text{vacuum}}$$

where  $\alpha, \beta > 1$ . A quantitative estimate of the environmental effect is the distance AB in Fig. 2. Such a scheme of quantification does little

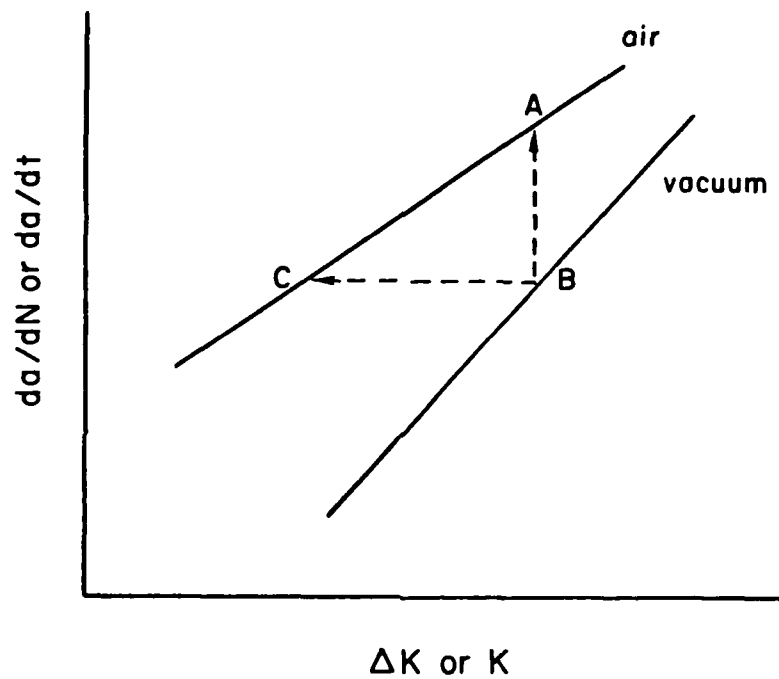


Figure 2. Diagram of Crack-Growth Rates in Air and Vacuum as a Function of Stress-Intensity Factor.

to elaborate on the mechanism of interaction. A more useful approach is to look at the effect of environment as a reduction in the crack-extension force necessary to drive the crack at a given velocity. Referring again to Fig. 2, the environmental effect at a given  $da/dt$  is the distance BC. Thus, an estimate of distances such as BC allows one to derive the crack-growth rates in air from those in vacuum, and vice versa. Note that although the two approaches are similar as far as Fig. 2 is concerned, as will be shown later, the latter approach allows one to incorporate the micromechanics of environmental crack-tip interactions. The task then is to determine the extent of horizontal translation as a function of  $da/dN$  or  $da/dt$ .

The oxygen environment may affect the crack-growth rate in several ways:

- a) Formation of brittle oxide scales.
- b) Reduction in crack-tip plasticity.
- c) Lattice expansion and chemical reaction associated with excess oxygen solubility through diffusion.
- d) Adsorption-induced reduction in true surface energy.

One or all of these factors may contribute to the environmental damage. However, a thorough understanding can be obtained only by treating each effect separately.

Oxide scaling is generally limited to temperatures of  $1000^{\circ}\text{C}$  and above. Therefore, in the temperature range of interest for turbine-disk materials ( $500 - 750^{\circ}\text{C}$ ), the scaling mechanism should have minor influence. One can safely ignore such effects. The oxidation stage prior to scaling, however, has an important effect upon crack-tip plasticity. In the case of grain-boundary fractures at low frequencies and high temperatures, the crack tips remain extremely sharp. Under these circumstances a significant fraction of the crack-driving force is provided through crack-tip shielding<sup>25,26</sup> by dislocations nucleated from the crack tip. In the case of

pure nickel, it has been found<sup>27</sup> by Rice and Thomson that the crack-tip-dislocation nucleation process lies on the border between the stress-assisted spontaneous nucleation and thermally activated nucleation. The formation of a high-modulus oxide layer at the crack tip affects the dislocation-nucleation process in two ways. First, it makes nucleation of dislocations even more difficult. Secondly, the presence of the oxide layer prevents the egress of oppositely signed dislocations through the crack tip, thus blocking sources of dislocations which are located at some distance from the crack tip. The former effect reduces the crack-tip shielding, and the latter reduces the plastic work dissipation. Since both essentially reduce the resistance to crack growth, the crack-driving force is reduced in the presence of an oxide layer. A quantitative estimate of the reduction in the crack-driving force has not yet been made (some calculations on the nucleation problem are currently underway).<sup>28</sup>

The diffusion of gaseous species into the region ahead of the crack tip causes dilatation of the lattice. The stresses thus generated can significantly affect the stress-intensity factor locally at the crack tip. In the present section the effect which such lattice expansion has upon crack-growth characteristics will be discussed. In addition to modifying the stress-intensity factor, the external species (primarily  $O_2$ ) could react and form brittle phases ahead of the crack tip. Also it could give rise to bond decohesion of the form discussed by Oriani and Josephic.<sup>29</sup> The former aspect will be disregarded in view of the fact that for thin-film oxidation, at first excess solubility occurs and only later nucleation and growth of oxides. Decohesion theory can be simulated by modification of the local stress-intensity factor.

We shall now focus our attention on the adsorption-induced reduction in true surface energy.

The present analysis is mainly applicable to sharp intergranular crack growth, although some estimate could be obtained in the case of transgranular crack growth. However, before considering the effect of adsorption, it is necessary to examine how the true surface energy of a solid affects the macroscopic crack-driving force.

Consider a distribution of dislocations piled up ahead of a semi-infinite crack. For simplicity only Model II and III cracks will be considered. Our experience with crack-tip plasticity suggests that Mode I cracks would cause only minor modifications in the results. Such a problem has been solved;<sup>30</sup> and the distribution function, COD, plastic zone size (dp), and dislocation free zone (dfz) have been obtained in terms of complete elliptic integrals of the first and second kinds. One of the results that emerges is that a maximum in the dislocation density occurs at a distance  $t_o$  ahead of the crack tip, rather than at the crack tip (as suggested by BCS theory). This has also been verified experimentally. The position of maximum density is found to be independent of the applied stress and is given by

$$t_o = \frac{\pi}{2} \frac{\mu \gamma_o}{\sigma_y^2}$$

where  $\mu = \frac{E}{2(1+\nu)}$  is the shear modulus,  $\gamma_o$  is the true surface energy of the solid, and  $\sigma_y$  is the yield stress. Perfect plasticity is assumed. There are four characteristic lengths involved, i.e., COD, dp, dfz, and  $t_o$ . From a dimensional consideration alone, at fracture a new result is

$$\frac{K_c^2}{2\mu} = \alpha_f \frac{\mu \gamma_o}{\sigma_o} \quad (11)$$

where  $K_c$  is the critical stress intensity at fracture and  $\alpha_f$  is a nondimensional number (typically 1 to 10).

Equation (11) can also be obtained by means of a different approach. In Ref. 30, the following mathematically exact solution was obtained:



$$\frac{K_c^2}{\gamma_o} = \frac{E^2(k)}{K^2(k)} \cdot \frac{1}{(1-k^2)}$$

where  $K(k)$  and  $E(k)$  are complete elliptic integrals of the first and second kinds, respectively, with modulus  $k = \sqrt{1 - (dfz/dp)}$ . The right-hand side of the expression is a function of the number of dislocations nucleated at the crack-tip and, at present, cannot be independently predicted. The simplest assumption is to treat the right-hand side as a constant, signifying the material's plasticity contribution to fracture.

Equation (11) has a significant implication. The left-hand side is normally represented in the Orowan-Irwin formulation as the effective surface energy,  $\gamma_{eff}$ . According to them

$$\gamma_{eff} = \gamma_o + \gamma_p \quad (12)$$

where  $\gamma_p$  is the contribution to the plastic-energy dissipation. Comparing Eqs. (11) and (12), we find

$$\gamma_p = \left( \frac{\alpha_f \mu}{\sigma_o} - 1 \right) \gamma_o \quad (13)$$

which shows that  $\gamma_p$  is proportional to  $\gamma_o$  with a constant of proportionality  $[(\alpha_f \mu / \sigma_o) - 1] \gg 1$ . Note that when  $\gamma_o = 0$ , then  $\gamma_p$  is also zero. This is expected physically, since zero surface energy implies zero bonding of atoms and a crack-driving force--no matter how small--would propagate the crack. Such a conclusion could not have been reached from Eq. (12), where it is often implicitly assumed that  $\gamma_p$  is independent of  $\gamma_o$ . Also, the large constant of proportionality is consistent with the high fracture toughness of engineering materials.

Returning to Eq. (11), we have

$$K_c = \sqrt{2\alpha_f} \cdot \mu \cdot \left( \frac{\gamma_o}{\sigma_o} \right)^{1/2} \quad (14)$$

Equation (14) has been verified<sup>31</sup> on variously tempered steels (different  $\sigma_0$ ) having varying sulfur content (different  $\gamma_0$ ), and the agreement was found to be extremely good. We shall use it in our analysis. It may be mentioned that a similar type of relation was obtained by Petch<sup>32</sup> in his analysis of ultimate strength of polycrystalline metals. For studying the environmental effect upon fracture, we can rewrite Eq. (14) as

$$K_c = \beta \sqrt{\gamma_0} \quad (15)$$

where  $\beta$  is a material property. The equation simply shows that the critical stress-intensity factor is proportional to the square root of the true surface energy. The problem then is to determine what influence adsorption has upon the true surface energy of a solid. For propagating cracks, such as in fatigue crack growth and creep crack growth, we shall simply replace  $K_c$  with  $K_v$ , where  $K_v$  is the stress-intensity factor necessary to drive the crack at a velocity  $v$ .

The effect of adsorption upon  $\gamma_0$  can be obtained through the Gibbs' adsorption equation,

$$\left. \frac{\partial \gamma_0}{\partial \mu} \right|_T = \Gamma \quad (16)$$

where  $\Gamma$  is the excess surface concentration of the adsorbing species (e.g., units of moles/cm<sup>2</sup>) and  $\mu$  its chemical potential. With an external gas at pressure  $p$ , the chemical potential is simply

$$\mu = RT \ln p \quad (17)$$

Substituting in Eq. (16),

$$\Delta \gamma_0 = RT \int \Gamma (d \ln p) \quad (18)$$

The problem with Eq. (18) is that  $\Gamma$  must be known as a function of the partial pressure of the external gas. This could, in principle, be determined from experimentally determined adsorption isotherms. Unfortunately, such isotherms are not available for the nickel-oxygen system. The best approximation involves the use of the Langmuir isotherm

$$\Gamma = \Gamma_s \frac{(Ap)^{1/2}}{1 + (Ap)^{1/2}} \quad (19)$$

where  $\Gamma_s$  is the number of molecules adsorbed at saturation, and A is a constant related to the heat of adsorption. The exponent 1/2 in the pressure term arises from the fact that the diatomic oxygen molecule has to dissociate upon adsorption. Substituting Eq. (19) into Eq. (18), one obtains

$$\Delta\gamma_o = 2\Gamma_s RT \ln[1 + (Ap)^{1/2}] \quad (20)$$

Note that A is still unknown. For the nickel-hydrogen system, A is  $5 \times 10^4/\text{mm}.$ <sup>33</sup> Equation (20) is valid at a given temperature up to partial pressures which yield one complete monolayer.\* In this extreme case a simpler result is obtained by using Eq. (18) directly, with  $\Gamma$  being set equal to a constant  $\Gamma_{O_2} \approx 10^{19}$  atoms/m<sup>2</sup>, giving

$$\Delta\gamma_o = -\frac{RT}{2} \Gamma_{O_2} \ln\left(\frac{p_1}{p_2}\right) \quad (21)$$

The factor of one-half accounts for the fact that the O<sub>2</sub> molecule dissociates on the adsorbed surface. Substituting into Eq. (15),

$$\frac{K_v|_{150 \text{ torr}}}{K_v|_{p_o}} = \left( \frac{\gamma_o - \frac{RT}{2} \Gamma_{O_2} \ln \frac{150}{p_o}}{\gamma_o} \right)^{1/2} \quad (22)$$

where  $p = 150$  Torr corresponds to crack propagation in air,  $p_o$  corresponds to the partial pressure in vacuum, and  $\gamma_o$  is the true surface energy in vacuum.

From Eq. (22)

$$\frac{K_v(\text{air})}{K_v(\text{vacuum})} = \left( 1 - \frac{RT}{2\gamma_o} \Gamma_{O_2} \ln \frac{150}{p_o} \right)^{1/2} \quad (23)$$

\* In the case of multiple layers, the BET theory (with more undetermined constants) is probably more appropriate.

Note that the use of Eq. (23) implicitly assumes that a monolayer buildup is a necessary requirement for environmental damage. Otherwise, one would be required to use Eq. (20) which contains two unknown constants. Such pre-monolayer effects have been ignored.

Data of other investigators<sup>34-36</sup> validate this assumption. Fatigue lives under different partial pressures of oxygen are found to exhibit two transitions. The lower transition corresponds to the partial pressure below which fatigue life is independent of partial pressure. The upper transition corresponds to the partial pressure above which fatigue life is independent of partial pressure. While some suggest<sup>35</sup> that the upper transition corresponds to a monolayer buildup, calculations based upon the kinetic theory of gases clearly show that the calculated transition pressure correlates much better with the observed lower transition pressure.<sup>36</sup> Therefore, in Eq. (23),  $p_o$  will be identified with the lower transition pressure.

The calculation of lower transition pressure is straightforward. From the kinetic theory of gases, the number of collisions of gas per unit area of wall (gm. mole/unit area) is given by

$$v = \frac{1}{4} \rho \bar{v}$$

where  $\rho$  is the density of the gas, and  $\bar{v}$  the average velocity of the gas molecules; that is,  $\rho = p/RT$  and  $\bar{v} = \sqrt{3RT/W}$ , where  $W$  is the molecular weight and  $p$  the partial pressure of the particular species. The following two units of  $R$  are useful in the calculations:

$$\begin{aligned} R &= 8.2 \times 10^{-2} \text{ lit. atm./gm. mole } ^\circ K \\ &= 83.14 \times 10^6 \left( \frac{\text{cm}}{\text{sec.}} \right)^2 \text{ gm./gm. mole } ^\circ K \end{aligned}$$

The Avogadro number also enters into the calculations. At 650°C one obtains

$$v = 3.3 \times 10^5 p \text{ collisions/site sec.} \quad (24)$$

where  $p$  is the partial pressure in Torr, and the cross-sectional area for oxygen adsorption is taken to be  $14 \text{ \AA}^2$ .<sup>37</sup> With a crack velocity  $da/dt$  (cm/sec.), the number of sites exposed per second is

$$s = 2.5 \times 10^7 \frac{da}{dt} \text{ sites/sec.} \quad (25)$$

With a sticking coefficient of unity, we have from Eqs. (24) and (25),

$$p_o = 76 \frac{da}{dt} \text{ torr} \quad (26)$$

with  $da/dt$  being in cm./sec. In the case of fatigue-crack propagation, one would use  $f(da/dN)$  rather than  $da/dt$ , where  $f$  is the frequency.

Using Eqs. (23) and (26) we are now in a position to compare the present theory with experimental results. Note that there is no adjustable parameter in the equations. The approach that will be used is to generate the  $(da/dt)$  vs.  $K$  curve in air, from the  $(da/dt)$  vs.  $K$  curve in vacuum or inert atmosphere. All available data are for 650°C.  $\gamma_o$  will be taken as  $1.5 \text{ J/m}^2$ --a reasonable value for nickel-base superalloys. The other relevant constants are  $R = 1.98 \text{ cal/gm. mole } ^\circ\text{K}$  and  $\Gamma_{O_2} = 10^{19}/\text{m}^2$ .

Figure 3 shows the creep-crack-growth data for Inconel 718 (Floreen and Kane<sup>1</sup>) at 650°C. Fracture was intergranular in both air and vacuum environments. The predicted curve in air is also shown. The correspondence is quite good. Figure 4 shows the 15-min. hold-time data for Astroloy (Pelloux and Huang<sup>38</sup>) in  $3 \times 10^{-5}$  Torr vacuum and air. The  $da/dN$  curve was converted to  $da/dt$ . Here also the fracture was intergranular in both environments, and the predicted curves exhibit good correlation. Figure 5 shows the 1-Hz FCG data for Astroloy (Pelloux and Huang<sup>38</sup>) in  $3 \times 10^{-5}$  Torr

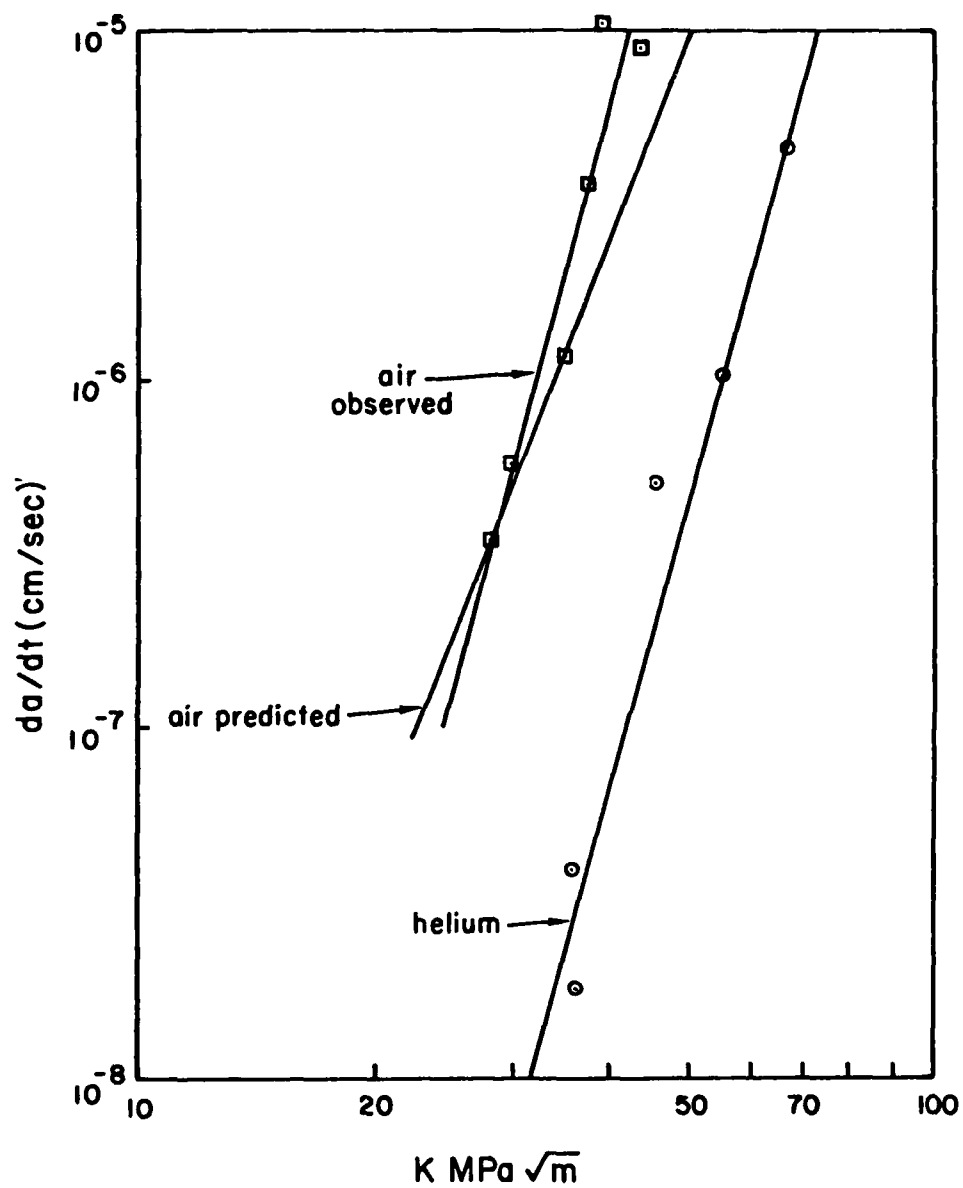


Figure 3. Creep Crack Growth in Inconel 718 at 650°C [from Floreen and Kane<sup>1</sup>].

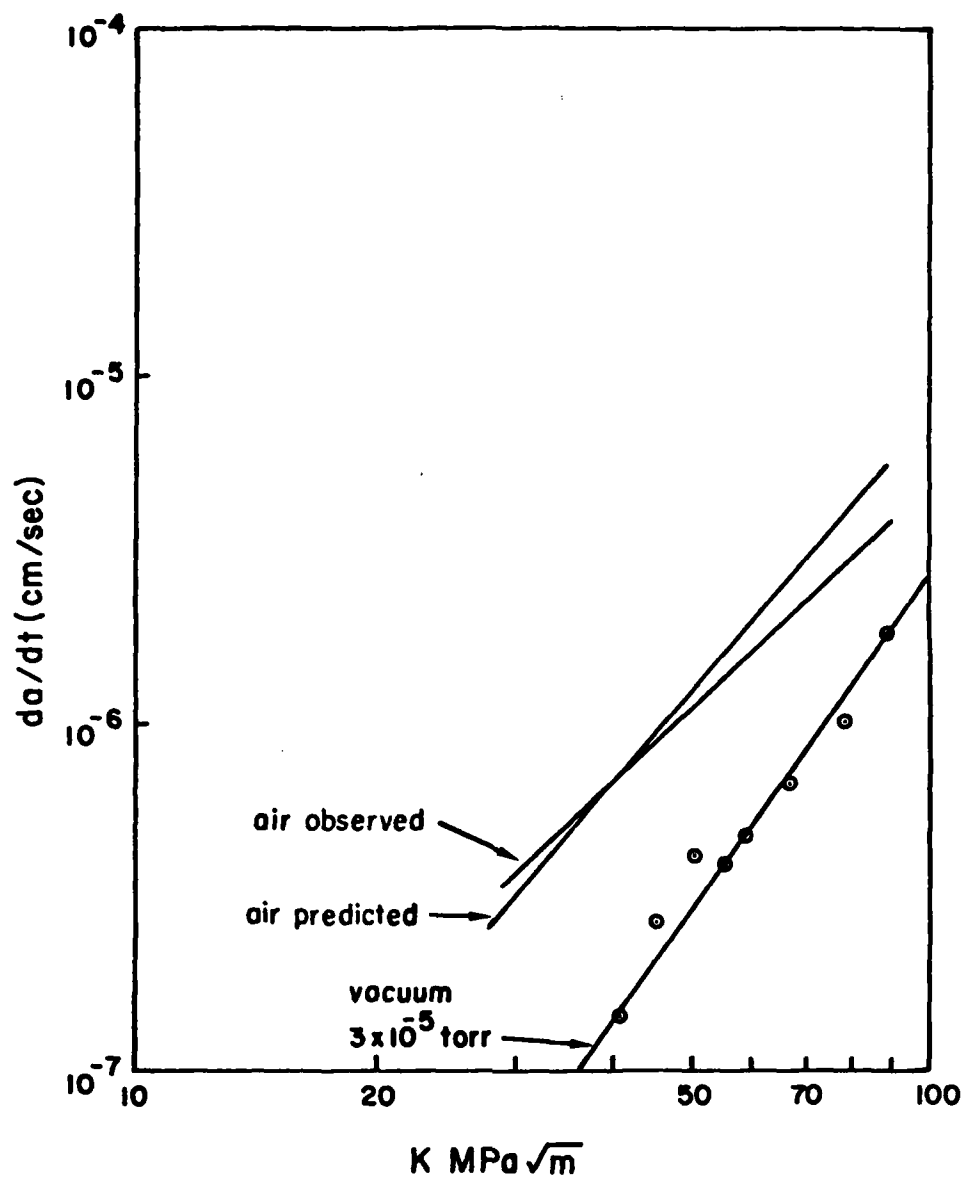


Figure 4. Crack Propagation in Astroloy for 15-min. Hold Time at 650°C [from Pelloux and Huang<sup>38</sup>].

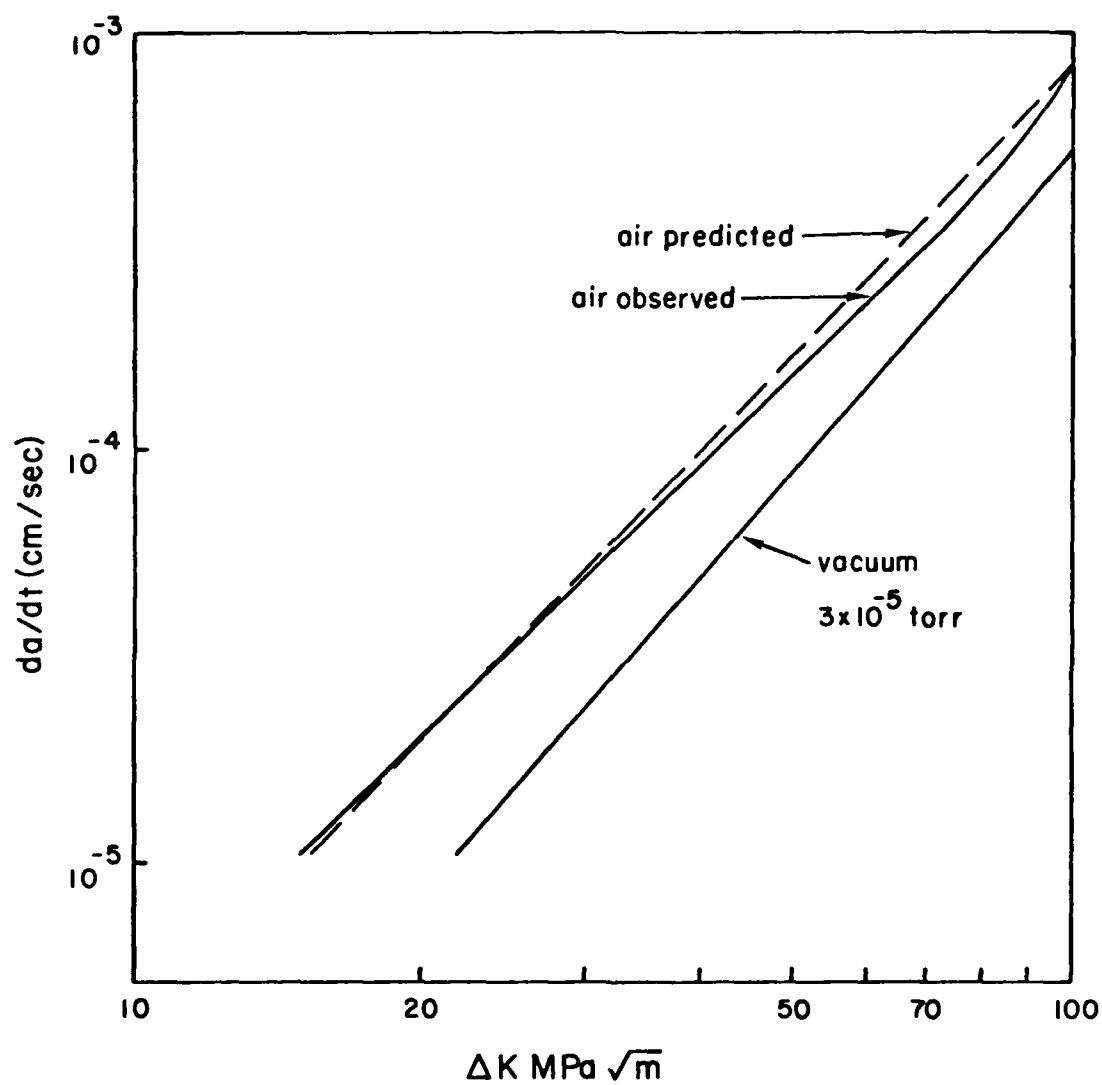


Figure 5. Fatigue-Crack Growth in Astroloy at 1 Hz [Pelloux and Huang<sup>38</sup>].



vacuum and air,  $da/dN$  was converted to  $da/dt$  by multiplying by the frequency. Although fracture was transgranular in both environments, the correlation is excellent. Figures 6 and 7 show FCG data<sup>1</sup> at 1 and 0.1 Hz, respectively, in Inconel 718. While the predicted curve is satisfactory at 1 Hz, the curve at 0.1 Hz exhibits poor correlation (predicted rate is still within a factor of two of observed rate). In the case of Inconel 718, it should be mentioned that while fracture was transgranular at both frequencies in the helium environment, it was intergranular at both frequencies in air. The poorer correlation is probably due to such a change in fracture mode. The poor correlation at 0.1 Hz also suggests that under conditions present in creep-fatigue interactions, the environmental damage is probably maximum. This point should be kept in mind in the design of engine components.

A noticeable feature of these figures is that the predicted curves have slopes which differ from those of the experimental curves. This could be attributed to several factors. First, we have neglected environmental damage prior to the formation of a monolayer. Secondly, we have considered a perfectly plastic solid. A work-hardening material would probably change the exponent in Eq. (22). Finally, in addition to adsorption, environmental damage is the result of the other factors given earlier in the discussion. One important effect is the expansion of the lattice caused by diffusion of oxygen atoms ahead of the crack tip, aided by a high hydrostatic-stress gradient. This aspect will be discussed in the next subsection. However, considering the satisfactory prediction, adsorption probably constitutes the most damaging effect.

#### c. Experimental Results for Baseline Creep Crack Growth (CCG) in Inconel 718

CCG tests were run on 10-mm-thick CT specimens of Inconel 718. Three tests were run at 650°C. The crack length was determined by a compliance technique and/or optical surface-crack-length measurements. The details of the tests are given in Table 1.

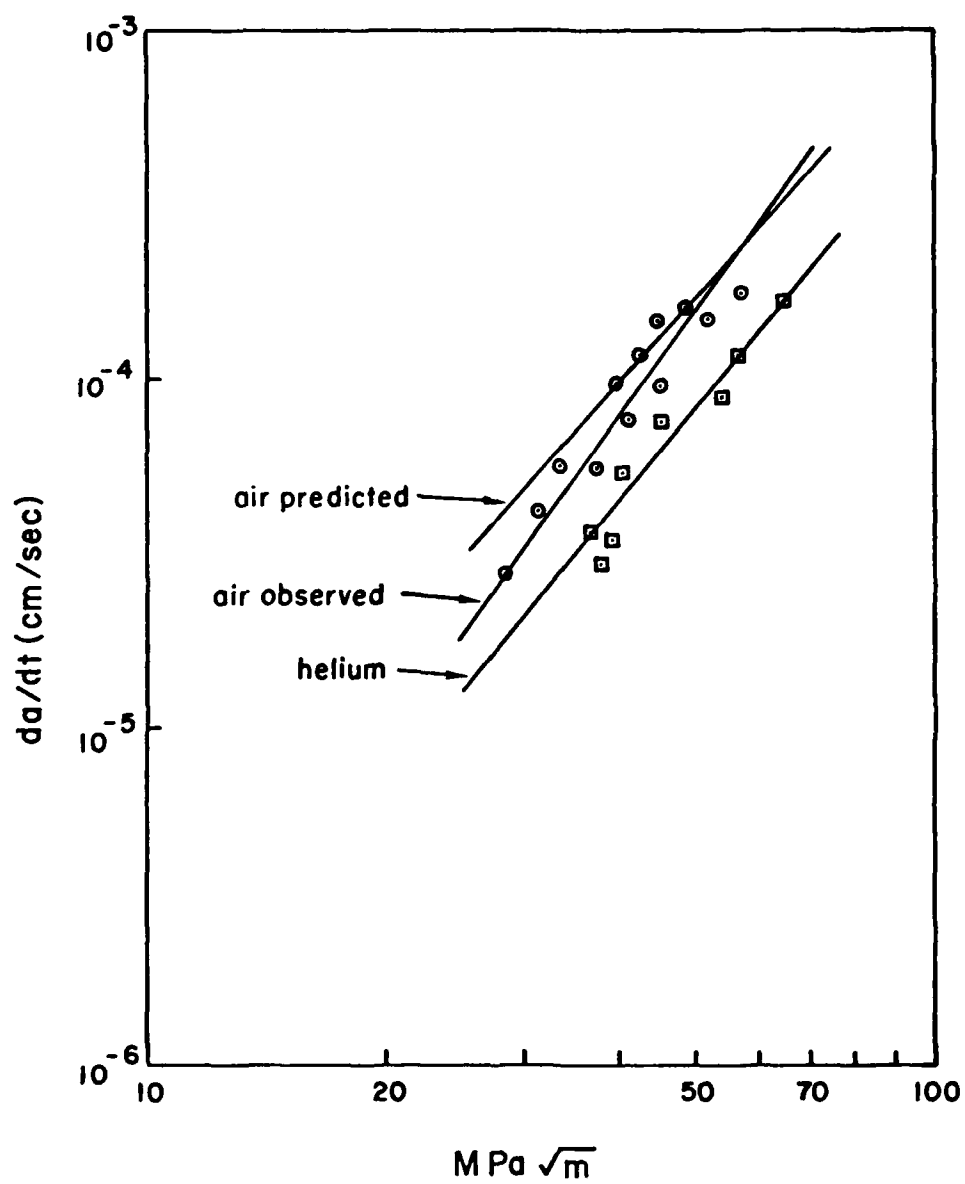


Figure 6. Fatigue-Crack Propagation in Inconel 718 at 650°C, 1 Hz [from Floreen and Kane<sup>1</sup>].

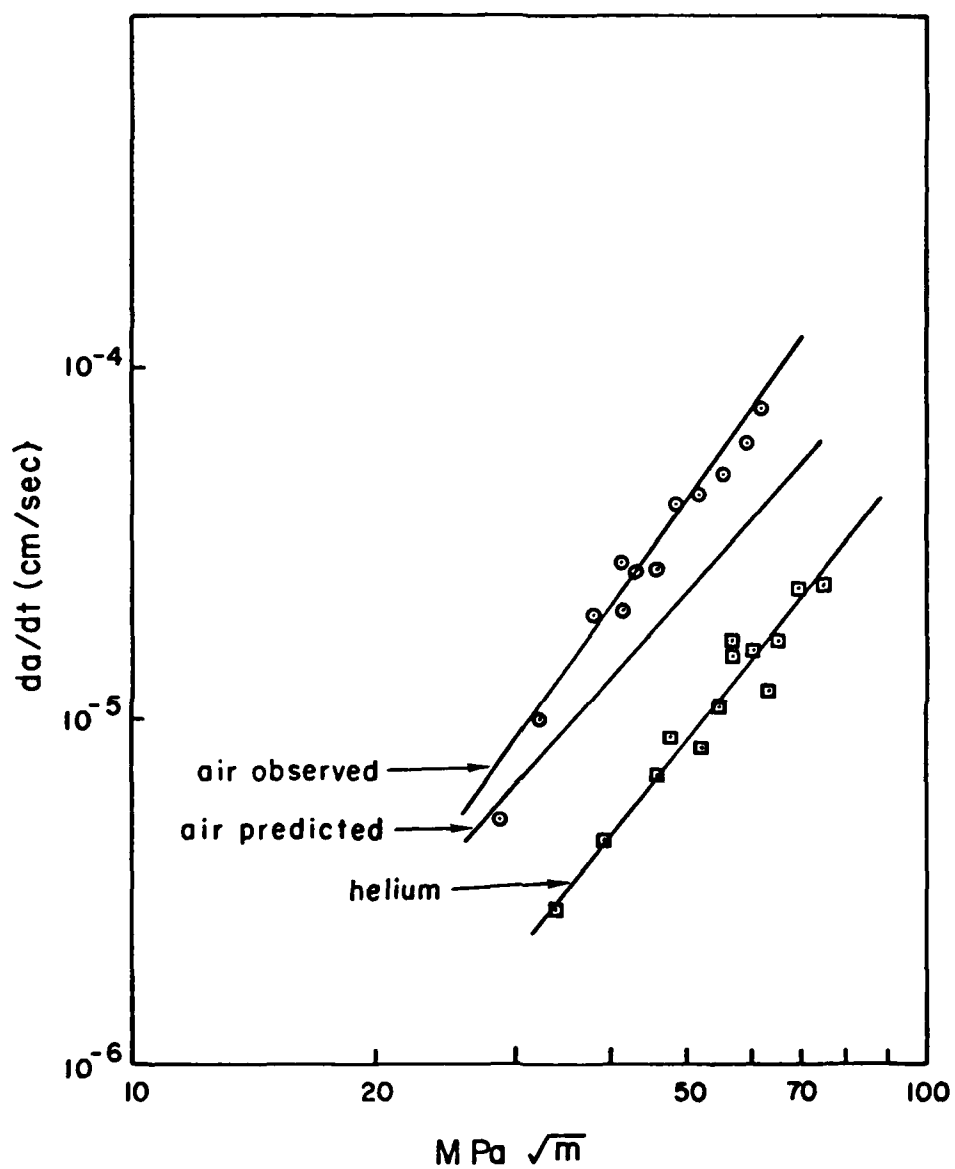


Figure 7. Fatigue-Crack Propagation in Inconel 718 at 650°C, 0.1 Hz [from Floreen and Kane<sup>1</sup>].

TABLE 1  
CCG TESTS ON INCONEL 718 AT 650°C -  
PRECRACKING AT ROOM TEMPERATURE, R = 0.1,  $\nu$  = 10 Hz

TEST	SPECIMEN	FINAL PRECRACKING $\text{ksi}\sqrt{\text{in}}$	RANGE OF K IN TEST $\text{ksi}\sqrt{\text{in}}$	PURPOSE
1	001	20	25-50	To determine $da/dt$ as a function of K
2	001	20	20-40	To determine whether long and short cracks exhibit similar behavior
3	002	25	30-40	To determine whether the unloading from compliance affects the growth rate

It was found that the CCG rate could be described as

$$da/dt \text{ (in./min)} = 7.41 \times 10^{-7} K^2$$

where K is in ksi  $\sqrt{\text{in.}}$ . Both the compliance data and that from optical surface crack length measurements yielded the same CCG behavior as shown in Figs. 8 and 9. Paradoxically, the compliance measurements predicted shorter crack lengths than those observed on the surface. This could be due to the pin sticking in the specimen during the test, although the pin rotated freely in the clevis after the test.

The CCG behavior of the long crack was the same as that of the short crack, when correlated by K. The long-crack behavior is shown in Fig. 10.

To determine the compliance for Fig. 9, a partial unloading--25% of the test load--and reloading was conducted every 15 to 30 min. In order to evaluate whether this unloading affected the CCG behavior, a third test was run in which no unloading occurred. Only the surface crack length was read. As shown in Fig. 11, the CCGR of this test was the same as in the other tests. This result shows that periodic unloading to measure compliance does not affect the CCG behavior under the test conditions.

It is of interest that in Test No. 1 the compliance decreased after 1 min. had passed than upon initial loading. However, this phenomenon did not occur in Test No. 2. The compliance remained the same for the first few minutes into the test. The difference between these tests was the final precracking K,  $K_f$ . In Test No. 1,  $K_f$  was 80% of the starting K; whereas in Test No. 2,  $K_f$  was 100% of the starting K. This result indicates that the solution to the puzzle of the decreasing compliance depends, in part, upon the plastic zone surrounding the crack tip. If the material in the plastic zone has become cyclically stable due to fatigue precracking, then there is no change in compliance. If, however, the initial test K is larger than  $K_f$ , then the material in the plastic zone is not cyclically stable, and changes occur after the initial loading.

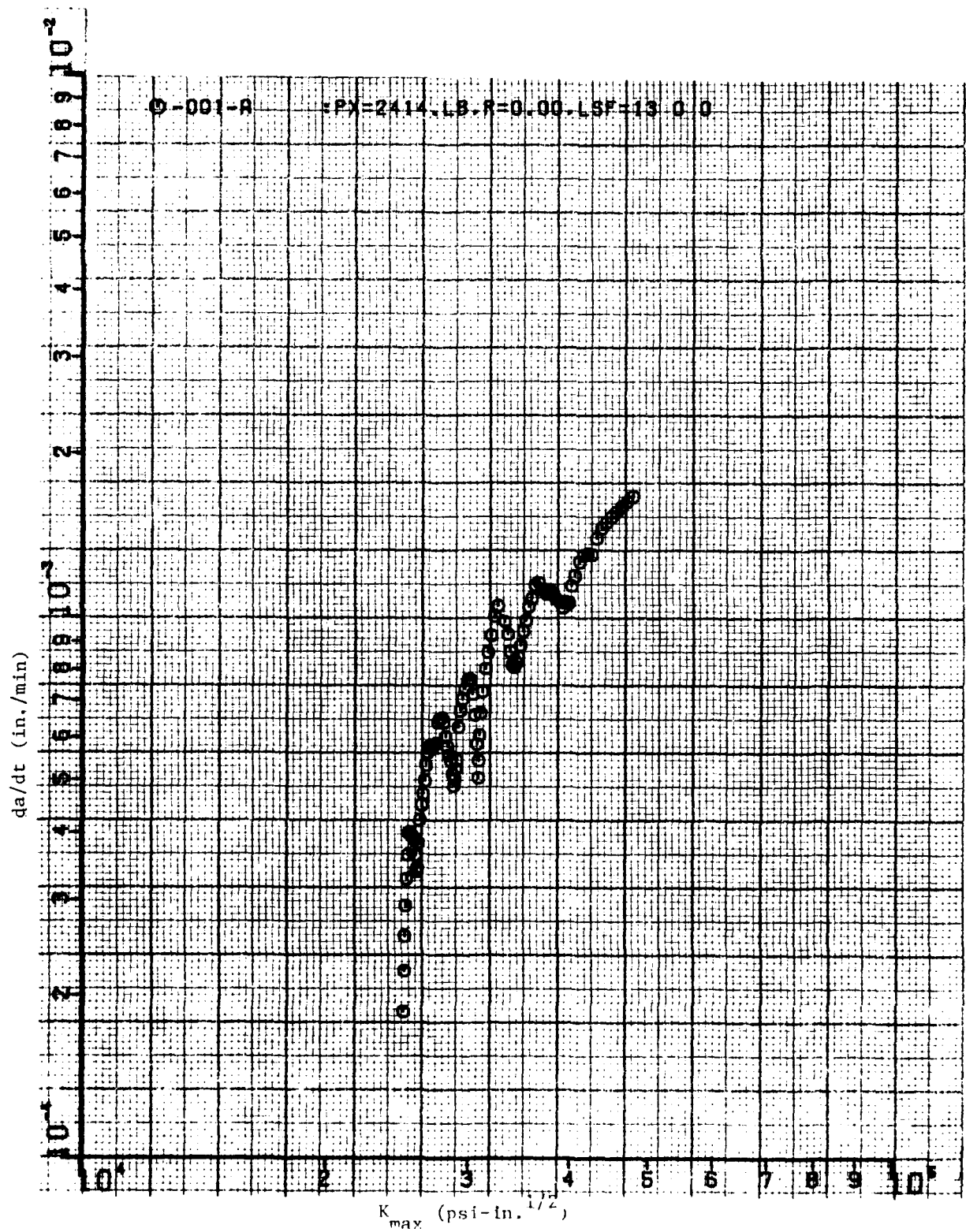


Figure 8. Creep-Crack-Growth Rate in Inconel 718 at 650°C Using Optical Surface-Crack-Length Measurements.

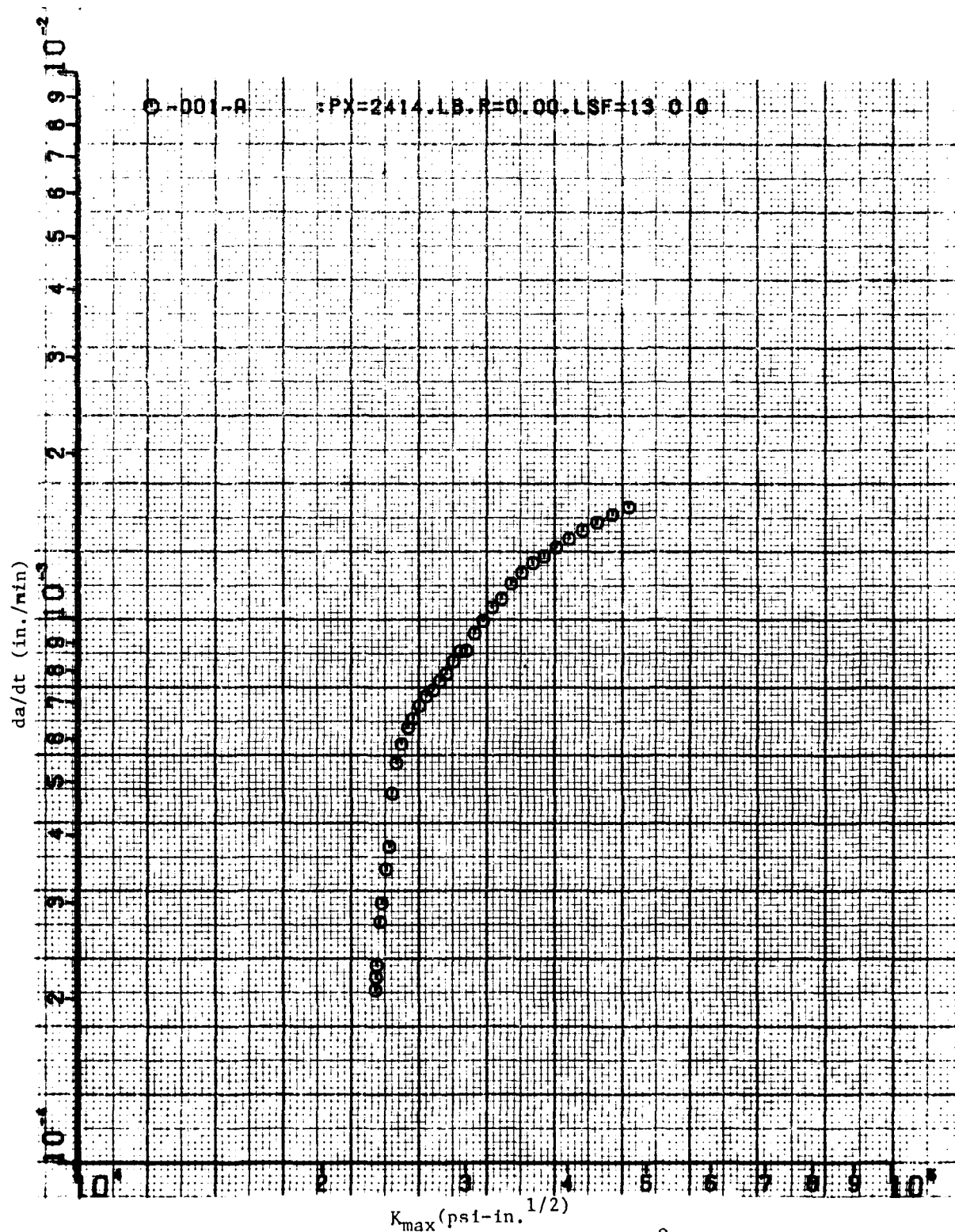


Figure 9. Creep-Crack-Growth Rate in Inconel 718 at 650°C Using Compliance Technique for Crack-Length Determination.

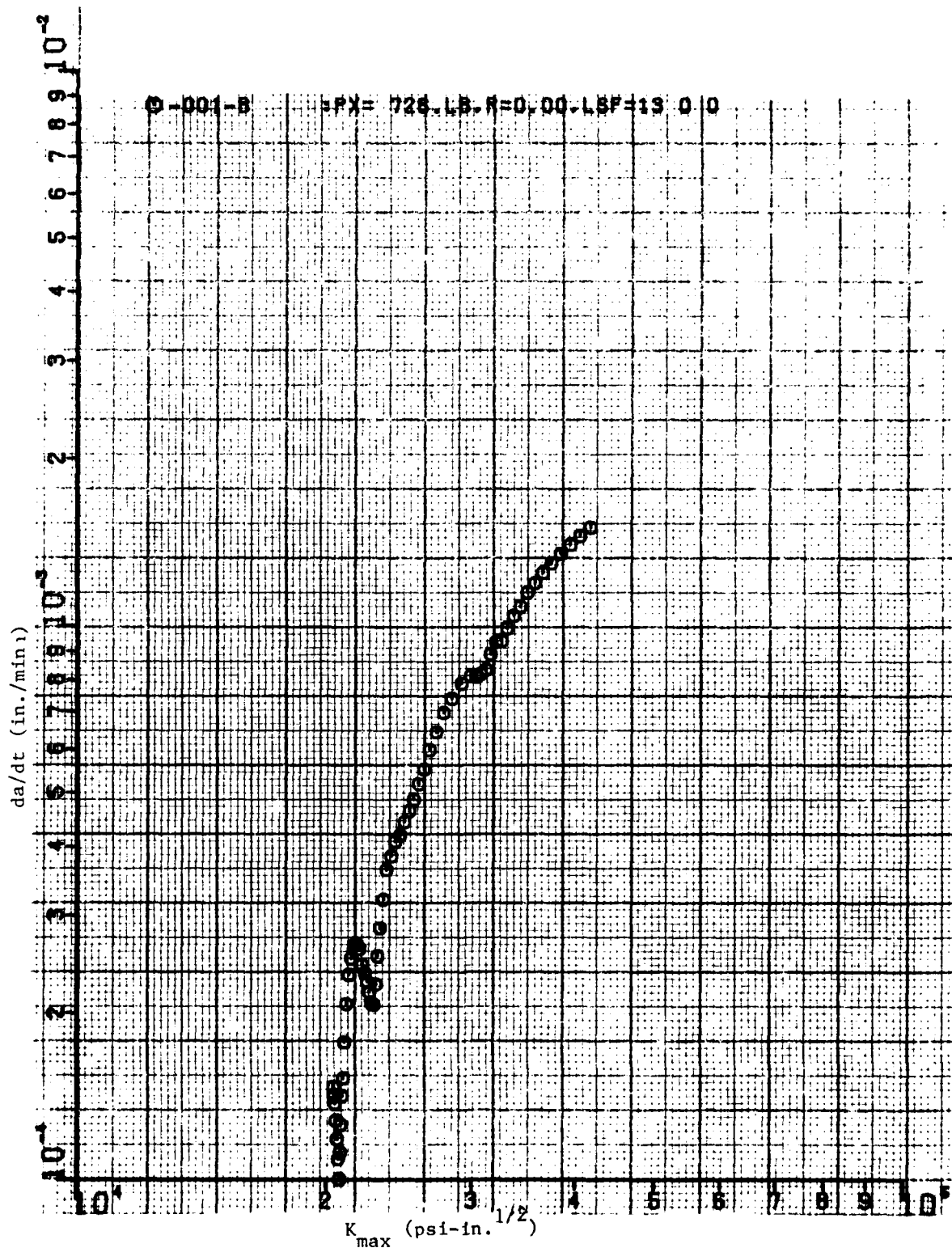


Figure 10. Creep-Crack-Growth Rate in Inconel 718 at 650°C Using Surface Measurements Where Crack Length is Longer Than for Results in Fig. 8.



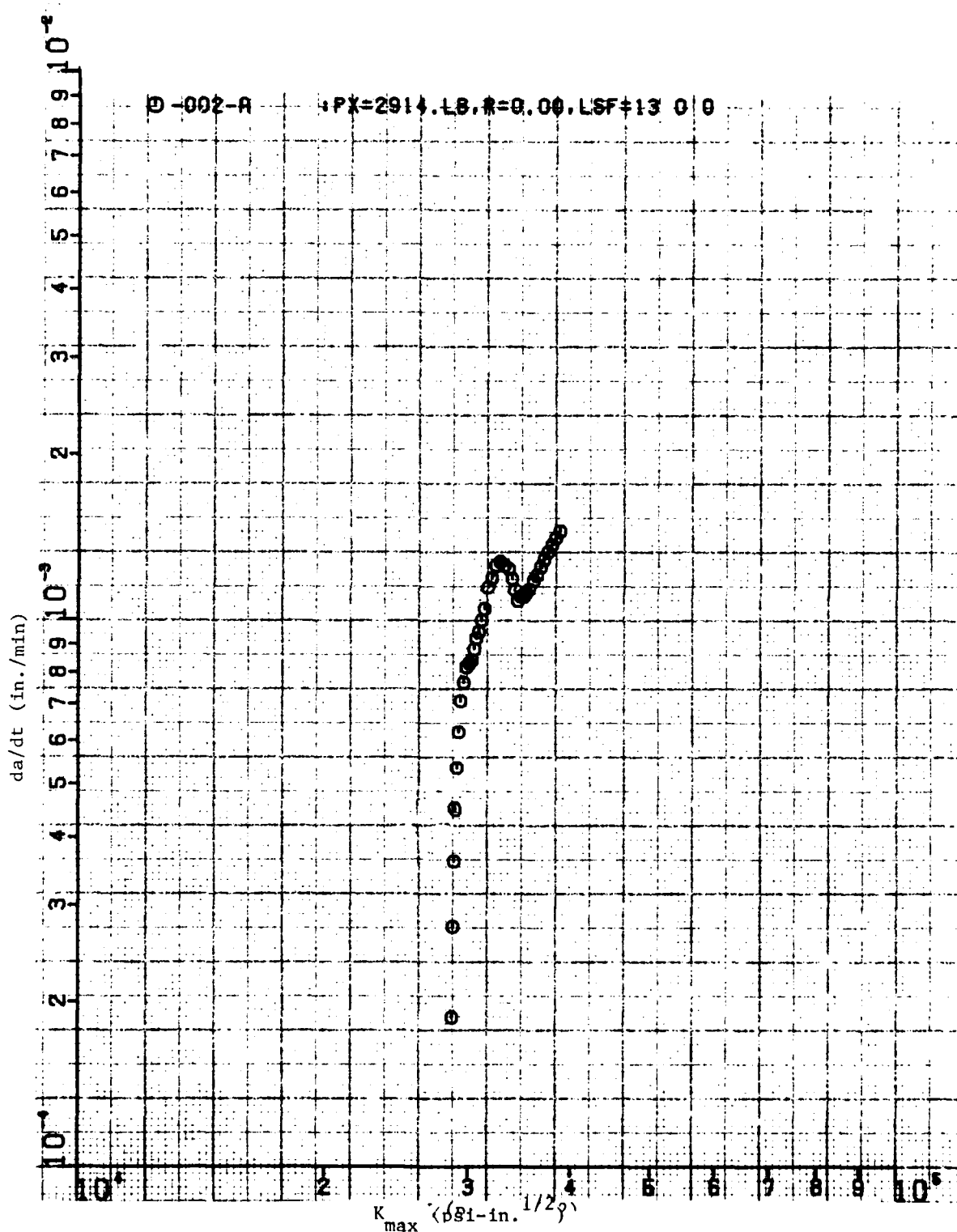


Figure 11. Creep-Crack-Growth Rate in a Second Specimen of Inconel 718 at 650°C Using Surface Measurements.

### 3. EVALUATION OF ENVIRONMENTAL AND WAVESHAPE EFFECTS

#### a. Experimental Fatigue-Crack-Growth Rates FCGR)

Preliminary FCGR results for IN100 at 732°C in laboratory air and dry argon at 5 and 1/6 Hz are given in Table 2. These results were obtained from tests of four WOL specimens, 0.3-in. thick. In addition, so-called baseline FCGR values for IN100 at 732°C in laboratory air at 2.5 Hz which were obtained from another investigation in the Facility are presented for reference.

The tests at 5 and 1/6 Hz were conducted at constant load, and crack-length measurements were made every 5 to 10 mils. After the crack had grown 100 mils, the alternate frequency was used for the next 100 mils of crack growth. One specimen was tested entirely in dry argon (assumed to be an inert environment), and the other three were tested first in dry argon for 500 to 600 mils of total crack growth and then in laboratory air to specimen failure. When the environment was being changed, the load was shed in order to obtain values of the crack-growth rate in lab air for low values of the range of the stress-intensity factor,  $\Delta K$ .

When proceeding to the next 100 mils of crack growth, the load was either held constant or increased in magnitude. By following this test procedure, it was hoped that the transient crack-growth behavior at the beginning of each 100-mil block of data would be minimized. Also for crack lengths with  $a/W < 0.5$ , the  $\Delta K$  did not vary by more than  $\pm 5\%$  and was assumed to be a constant (over a 100-mil growth increment) when determining the growth rates in Table 2.

The results in Table 2 were obtained by two different data-reduction schemes. The CGR were determined from a least-squares-error linear fit to the data. This procedure reduced the scatter in the results which was caused, in part, by the long focal length of the traveling microscope used to read the crack length and the difficulty in locating the crack tip. The scatter in a reading was estimated to be  $\approx \pm 5$  mils.

TABLE 2

PRELIMINARY VALUES OF FCGR FOR IN100 IN LABORATORY AIR AND DRY ARGON

$$\frac{da}{dN} \text{ Units} - 10^{-5} \text{ in./cyc.}$$

Temperature = 732°C

R = 0.1

L. A. - Laboratory Air at 760 Torr

D. A. - Dry Argon at 780 Torr

Frequency (Hz)

Average $\Delta K$ (ksi $\sqrt{\text{in.}}$ )	2.5	5		1/6	
	L.A. *	L.A.	D.A.	L.A.	D.A.
13.1	.25	.30 .46	.32 .3		3 4.5
14.3	.42	.81		3.	4.5
15.5	.7		.66 .58		
16.9	1.0	1.2		4.	8.9 12.
18.4	1.3		.82 1.1 1.4		
20.8	2.3	2.0		12.	6.1 9.3 13.
23	3.1		2.2 2.6	10.	
26.2	4.0			16.	12. 23.
30.	5.1	5.3 5.4	4.0 3.5	23.	
42.5	11.	15.	10.	36.	45.

\* Baseline - FCGR data for another heat of material.

When  $a/W > 0.5$ , a second data-reduction scheme--a five- or a seven-point polynomial fit per ASTM Standard Practice E647--was used to determine the CGR. The CGR were obtained for a range of  $\Delta K$  values over a 100-mil growth increment. For the test procedure, which was described previously, this data-reduction scheme would only be applied to the data for laboratory air and  $\Delta K \geq 30 \text{ ksi } \sqrt{\text{in.}}$

A comparison of the results in Table 2 at 5 Hz indicates that the CGR is slightly higher in lab air than in dry argon. At 1/6 Hz and the lower  $\Delta K$  levels, the CGR appears to be slightly lower in lab air than in dry argon. In lab air the growth rate was about a factor of five higher at 1/6 Hz than at 5 Hz, while in dry argon the rate was about a factor of 10 higher at 1/6 Hz than at 5 Hz. The CGR in lab air at 2.5 and 5 Hz showed very good agreement, even though the specimens were from two heats of material.

The preliminary results show that the inert environment is detrimental to the CGR at the low frequency and beneficial at the high frequency. At 1/6 Hz in dry argon, the higher CGR could be attributed to the activation of a time-dependent creep mechanism. In lab air the creep mechanism--normally grain-boundary sliding--is impaired by the embrittling nature of the oxidation, and the CGR is reduced. At 5 Hz in dry argon, the creep mechanism which was a dominant factor at 1/6 Hz is now suppressed, and a time-independent mechanism becomes a dominant factor in the CGR. In the presence of lab air, the embrittling oxidation process tends to enhance the crack-growth mechanism.

In attempts to confirm these interpretations of the data from observations of the fracture surface of the specimen tested in dry argon, it was found that the surface of the grains was obscured by a foreign substance (see the next sub-section, Fractography). Also, on the sides of the specimen which were polished prior to testing, a dark film formed during the test. Small samples of material were prepared and subjected to the same temperature and environment (lab air and dry argon) as the crack-growth specimens.

Auger analysis of the surface composition of these samples was conducted. The results indicate that compounds of oxygen were formed on the sample surfaces in the dry-argon environment. The conclusion is that oxygen was present in the environment for the CGR results. Even though the Auger analysis cannot quantify the amount of oxygen in the dry-argon environment in the test chamber, probably sufficient oxygen is present to affect the CGR. As a result of the contaminated fracture surface and the confirmed oxide film on the sides of the specimens, the use of the environmental chamber and, thus, the investigation was discontinued.

b. Fractography

Detailed fractography was carried out on two IN100 specimens, both tested at 732°C. Specimen 7ENWS-2 was cycled alternately at 5 Hz and at 1/6 Hz in a dry-argon environment. However, the environment reacted with the metal as evidenced by discoloration of both the specimen sides and the fracture surfaces. Presumably the dark external film was an oxide, although microprobe analysis was not performed; charging up of the electron beam in the SEM indicated the presence of a non-conducting layer--probably an oxide.\* Specimen 19SG-2 was a creep-fracture sample, with  $K$  increasing from 36 to 66 ksi  $\sqrt{\text{in}}$ . This test was conducted in laboratory air.

Figure 12 is a macrofractograph of specimen 7ENWS-2. Although the demarcation between regions of 1/6 Hz and 5 Hz is blurred at low  $\Delta K$ , well-defined boundaries can be seen between regions of different frequencies at high  $\Delta K$ . The main feature delineating the two regions is the roughness of the fracture surfaces. On a microscopic scale, the fracture is intergranular at 5 and 1/6 Hz, as seen from Figs. 13 and 14, respectively.

It is thought that the roughness of the fracture surface in Fig. 12 is caused primarily by the oxidation process at this high temperature. The mechanics of oxidation-enhanced fracture will be discussed later in this

---

\* Auger analysis, discussed in the previous subsection, indicated that oxide compounds were present.

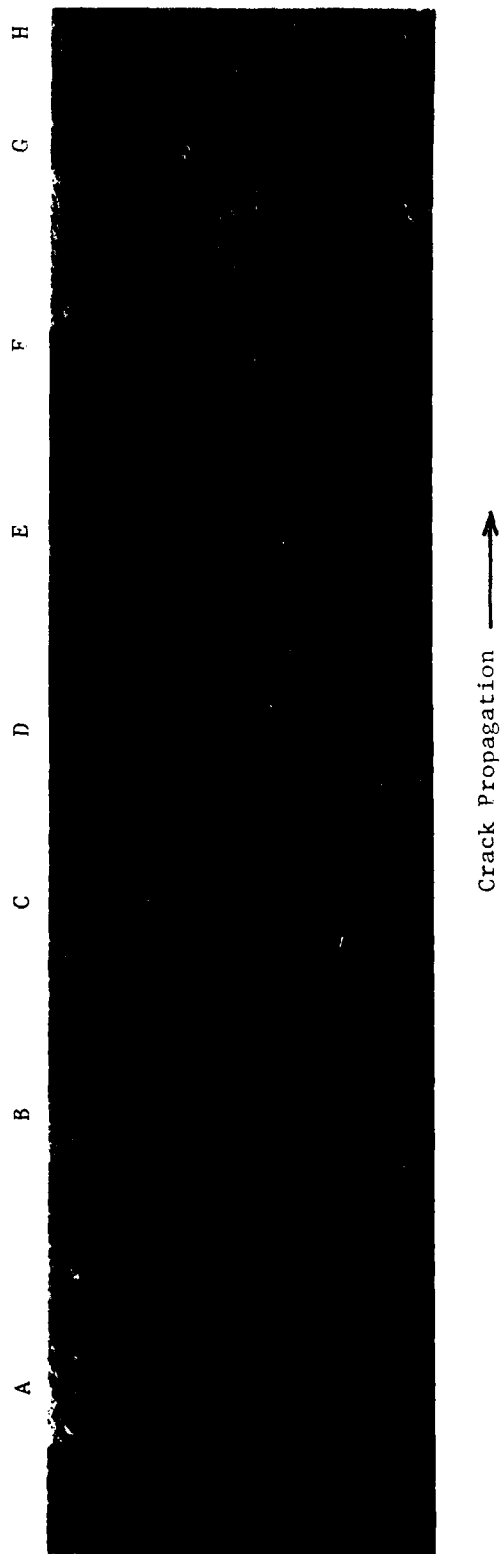


Figure 12. Specimen 7ENWS-2 Cycled Alternately at 1/6 Hz and 5 Hz at 1350°F. Regions A, C, E, and G correspond to 1/6 Hz, while Regions B, D, F, and H correspond to 5 Hz. Magnification 14x.

Crack Propagation →

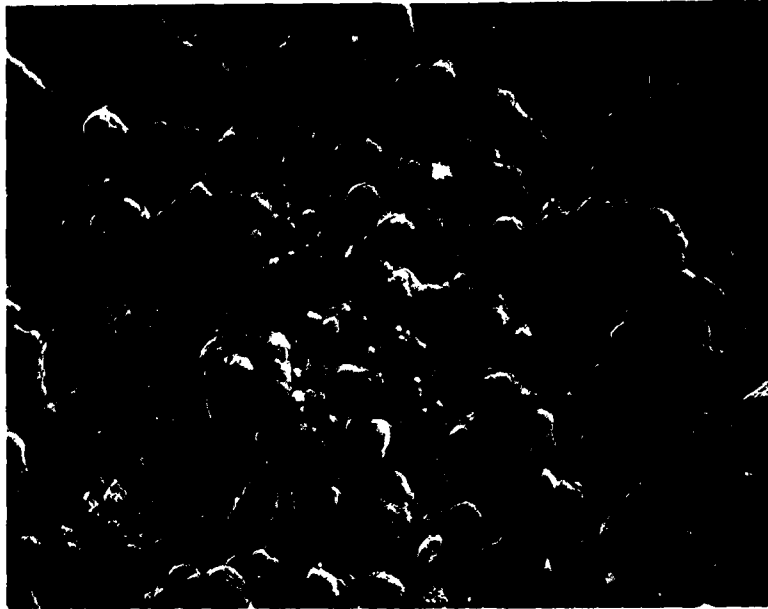


Figure 13. Higher-Magnification Micrograph from Region D (5 Hz) in Figure 12. Magnification 1000×

Crack Propagation →

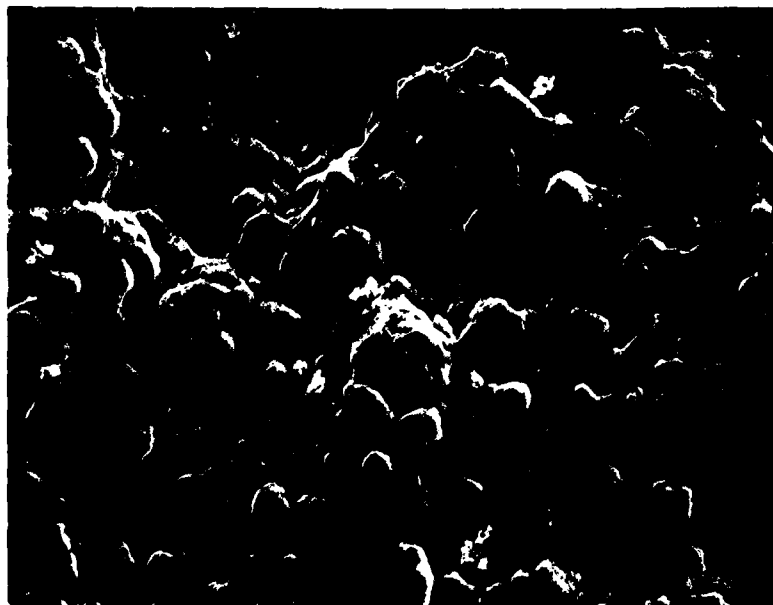


Figure 14. Higher-Magnification Micrograph from Region E (1/6 Hz) in Figure 12. Magnification 1000×

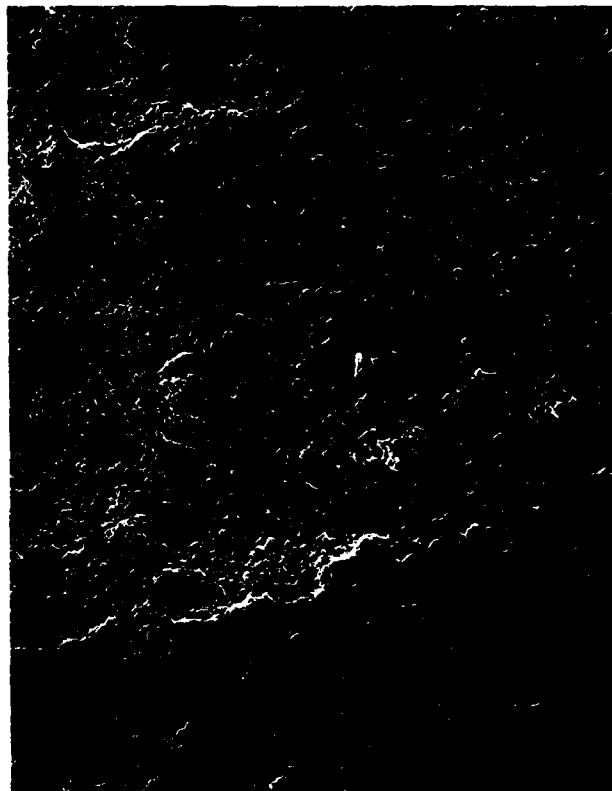
section. Suffice it to say that the fracture surface in Region B (Fig. 12) is rougher than that in Region F (Fig. 12), although the frequency was 5 Hz in both regions. Since the tests were run at a constant load amplitude,  $\Delta K$  in Region B is smaller than in Region F. Remembering that the CGR decreases with decreasing  $\Delta K$ , more time is available for oxidation-enhanced growth in Region B than in Region F. Therefore, the fact that Region B is rougher than Region F is consistent with the assumption that ridging or roughening of the fracture surface is associated with oxidation effects.

One very interesting feature is observed in the boundary between Regions E and F. Fingerlike ridges can be seen protruding from Region E to F. Since the fracture surface in Region F is much smoother than in Region E, it is thought that fracture at 1/6 Hz progresses by the formation of fingerlike instabilities along the crack front. A higher-magnification micrograph, Fig. 15, shows the boundary between Regions E and F, together with fingerlike protrusions. Similar protrusions were also observed in a creep-fracture sample from an investigation<sup>39</sup> by Donat, *et al.*, in which the specimen was broken open at room temperature following tunneled crack growth at elevated temperature. Fingerlike ridges were observed protruding from the curved crack front of creep fracture into the region of fast room-temperature fracture. Thus, fingerlike protrusions seem to be a characteristic feature of both low-frequency and sustained-load tests. They seem to play a dominant role in crack propagation.

#### 4. PRELIMINARY STUDIES ON THE PROPAGATION OF SHORT CRACKS AT NOTCHES

Experiments were initiated for determining the propagation characteristics of short cracks at notches. The emphasis was on evaluating the suitability of the specimen geometry and the testing technique. The material chosen for the investigation was 7075-T651 aluminum alloy. The reasons for choosing this alloy were:





Crack Propagation —————→

Figure 15. Boundary Between Regions E and F in Fig. 12. Region E is to the Left and Region F is to the Right of the Micrograph. Note the Fingerlike Instabilities Protruding from Region E to F. Magnification 140×

- (1) easy availability and machinability and
- (2) the alloy produces well-defined striations and, therefore, macroscopically determined growth rates could be correlated with striation spacings.

A modified keyhole specimen, 1/4-in. thick (shown in Fig. 16), was chosen for the investigation. The elongated specimen geometry was chosen in order to amplify the COD.\* The sample was cycled at a maximum load of 200 lb and an R-ratio of 0.1 which corresponded to stresses<sup>†</sup> of ~ 30 ksi and 70 ksi at A and B, respectively. The COD was measured using a 1/4-in.-gage-length extensometer. However, since the COD was too large, this measurement was discontinued after a few thousand cycles. An attempt was made to employ the replica technique for measuring the crack lengths. Replicas were taken of the side surfaces around the hole using cellulose acetate tape. The replicas were held in position using scotch tape and acetone sprayed on the surface. After drying, the replicas were carefully peeled from the surface, stored on glass slides, coated with aluminum for improving reflectivity, and observed under an optical microscope. Cellulose acetate tape was found, however, to be inadequate for taking replicas from the inside surface of the hole. The curvature of the surface created a major problem. For this surface a Ladd-type replica was used. The process consisted of applying a solution on the surface and then firmly pressing on the replicating tape in order to remove bubbles. It should be mentioned that a few bubbles always remained. However, this did not create a major problem because minute features on the specimen surface were imprinted on the bubbles, and these features could be detected by careful focusing of the microscope. Nevertheless, it is suggested that other types of replicating tapes and procedures be tested by which all bubbles may be removed.

\* In fact, it became apparent later that the COD was excessively large and beyond the range of the extensometer.

† The test had been completed by the time the results of the stress analysis were available.

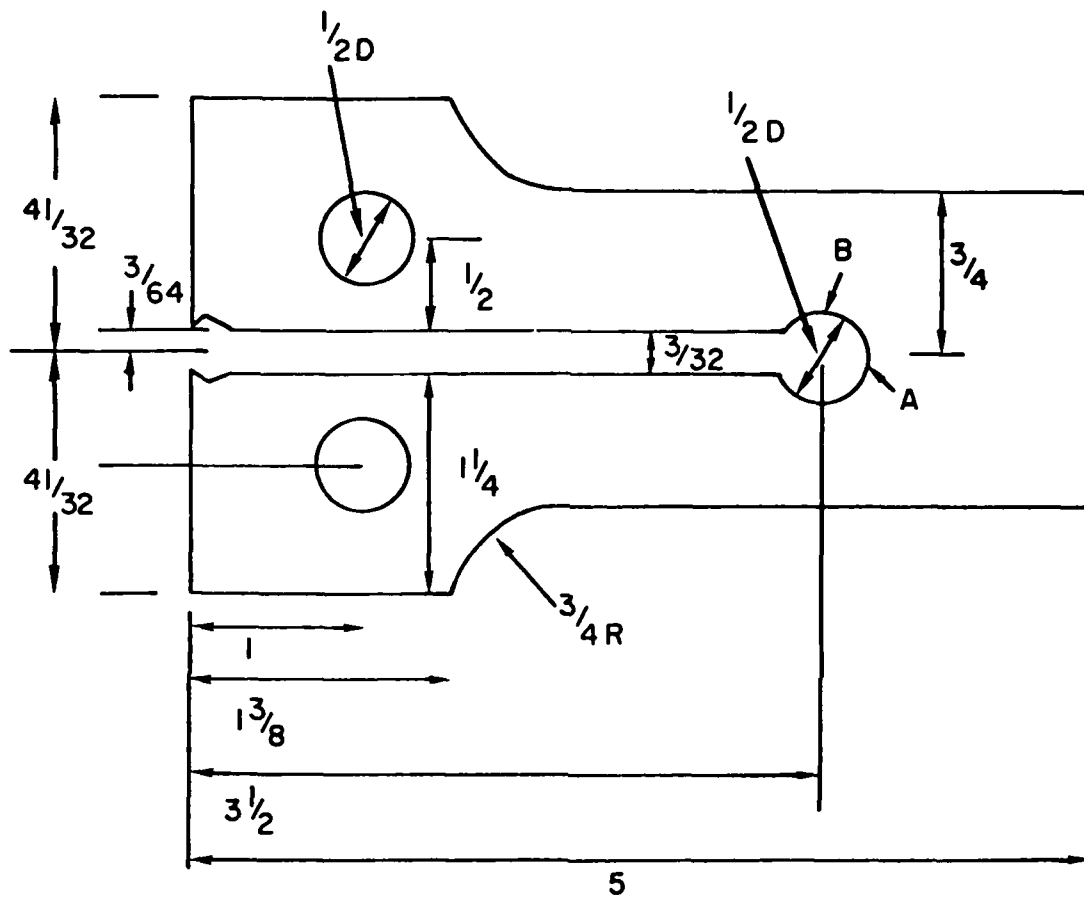


Figure 16. Keyhole Specimen for Short-Crack Investigation (Dimensions in Inches).

Replicas were made at 5,000-cycle intervals, the initial replica being made at 80,000 cycles. The specimen fractured near a corner at B after 108,000 cycles. Scanning electron micrographs were taken of the fracture surface.

In addition to the short crack-propagation test, a compact-tension specimen of 1/4-in. thickness was tested in order to obtain long-crack data for the same thickness and batch of material. Also, examination of the fracture surface of this specimen allowed the calibrating factor relating the striation spacing and crack-growth rate to be obtained.

Figure 17 contains the long-crack propagation data. The specimen failed at a  $K_{max}$  of  $\sim 17 \text{ ksi}\sqrt{\text{in.}}$ , which is quite low. This is expected since the loading axis was perpendicular to the rolling direction. Figures 18 and 19 are SEM micrographs of the fracture surface at distances of 12 and 14.5 mm, respectively, from the edge of the machined notch. The striation spacings are  $4 \times 10^{-5}$  and  $5.8 \times 10^{-5}$  in. for Figs. 18 and 19, respectively. Through calculation of the  $\Delta K$  for the given positions of the crack front and the use of Fig. 17, the values of  $da/dN$  are found to be  $1.1 \times 10^{-5}$  and  $1.5 \times 10^{-5}$  in/cycle for Figs. 18 and 19, respectively. Thus, the striation spacings are  $\sim 3.5$  times the macroscopic crack-growth rate. Similar values were obtained at other locations, although in some cases the striations were not so well defined.

In the case of the short-crack specimen, no cracks were observed on the replicas prior to fracture, which was unfortunate. Scratches on the surface (in spite of a 3- $\mu$  polish) did complicate detection of surface cracks. While it can be said with certainty that no cracks existed on the side surfaces 3,000 cycles prior to fracture, such a definitive statement cannot be made regarding the inside of the hole. The scratches there were deeper than on the side surfaces. There were indications of delamination from scratches; however, these were determined not to be cracks. Cracks of lengths greater than 250  $\mu$  should have been easily detected since the replicas were taken with the specimen loaded to 20% of maximum load. Thus, it appears that most of the crack propagation on the surface occurred within the last 3,000 cycles prior to fracture.

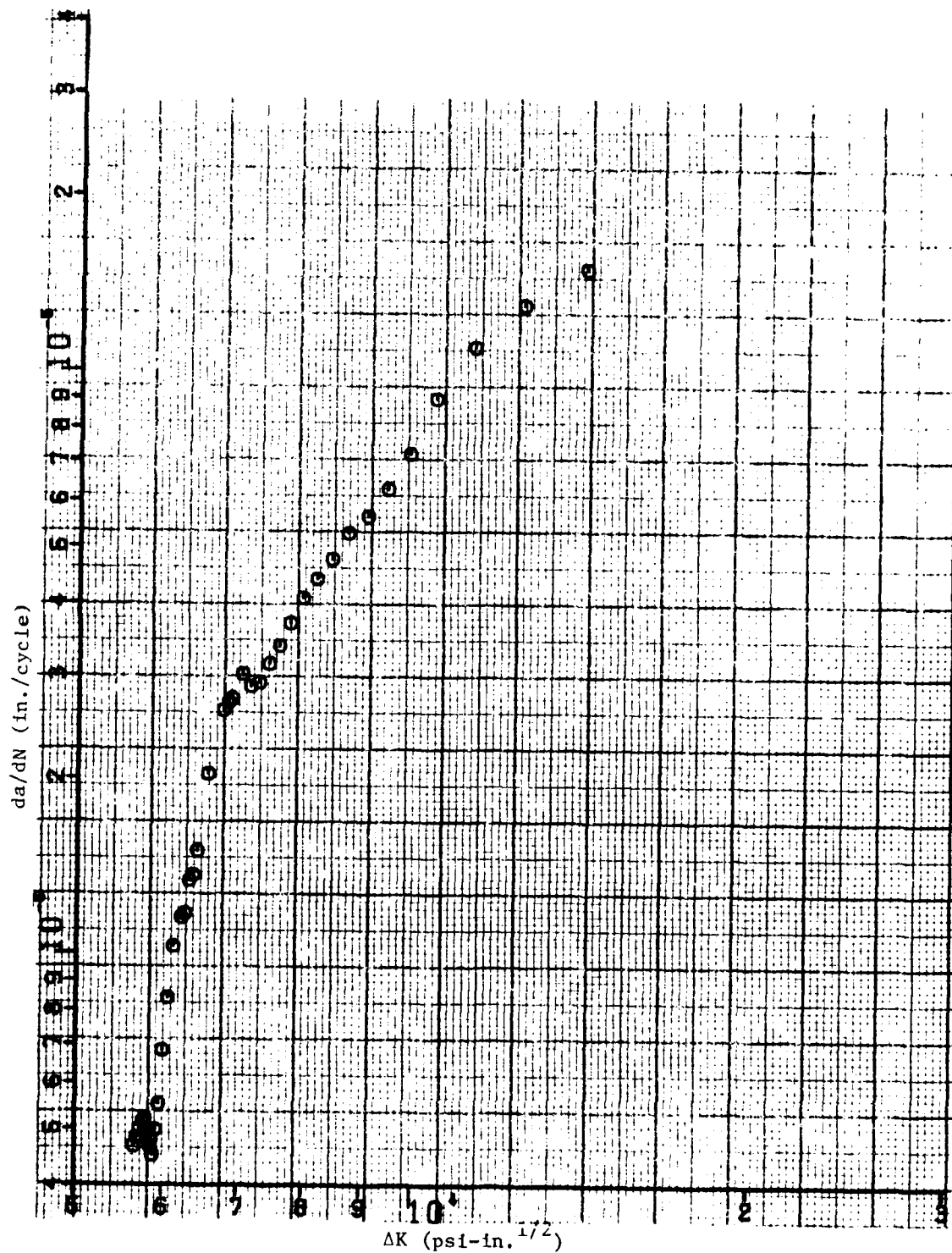


Figure 17. Fatigue-Crack-Growth Rate for a Long Crack in 7075-T651 Aluminum.

Crack Propagation —→



Figure 19. SEM Micrograph of the Fracture Surface of a Long-Crack Specimen at a Distance of 14.5 mm From the Machined Notch. Magnification 2000 $\times$ .

Crack Propagation —→

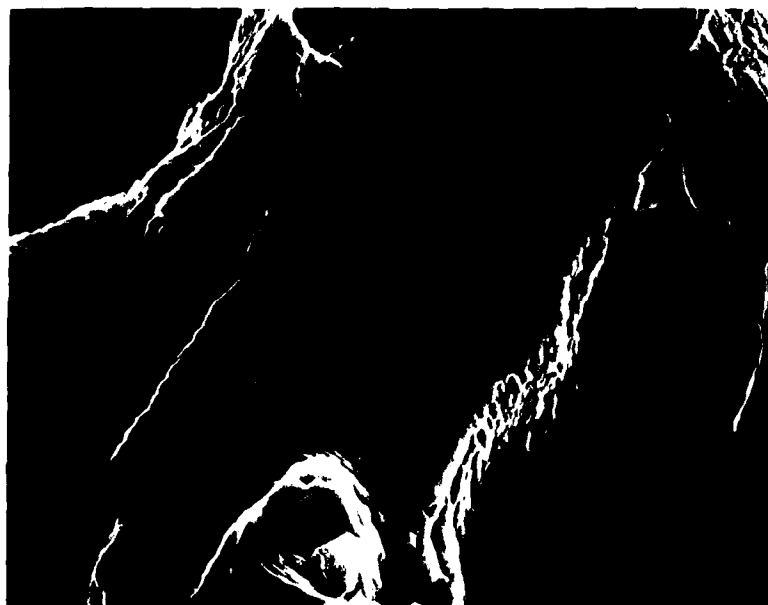


Figure 18. SEM Micrograph of the Fracture Surface of Long-Crack Specimen at a Distance of 12 mm From the Machined Notch. Magnification 2000 $\times$ .

This is possible since the fracture toughness of the material is quite low. Although the present test essentially failed, it does point out that for low-fracture-toughness materials, crack lengths must be measured at very short intervals if there is general yielding around a stress concentration. Had a notch stress near the endurance limit been chosen initially, then uncertainty of the crack initiation would have required taking replicas many times, although in this case crack-length observation points could have been spaced a greater number of cycles apart. Thus, regardless of the stress level around a notch, a large number of replicas is always necessary.

Figure 20 is a schematic diagram of the fracture surface, showing regions of fatigue and overload fracture. Within a 0.1-mm depth from the side surface AD, no striations are visible. Striations below this depth are oriented at an angle to this surface, suggesting that the crack propagated internally and then broke open at the side surface. This behavior, although strange, is consistent with the fact that no cracks were visible on the side surface prior to fracture. Such phenomena must be borne in mind when performing future experiments.

Striations were visible along the notch surface (near AB of Fig. 20). Figure 21 is a sketch showing the locations of the micrographs in Figs. 22, 23, and 24. The striation spacings in these figures are  $1.9 \times 10^{-5}$ ,  $3.8 \times 10^{-5}$ , and  $3.25 \times 10^{-5}$  in., respectively. Using the calibrating factor of 3.5 obtained from the long-crack experiment, the SEM micrographs suggest a  $da/dN$  of  $5.4 \times 10^{-6}$ ,  $1.1 \times 10^{-5}$ , and  $9 \times 10^{-6}$  in/cycle in Figs. 22, 23, and 24, respectively. A rough comparison can be made with long-crack data by evaluating  $\Delta K$  at various regions, using the formula  $\Delta K = 0.9\sigma \sqrt{\pi l}$ , where  $\sigma = 60$  ksi and  $l$  is 0.1, 0.7, and 1.2 mm at Points (7), (8), and (9), respectively, in Fig. 21. The factor 0.9 accounts for the load ratio. The  $da/dN$  values for long cracks corresponding to these  $\Delta K$  values may be obtained from Fig. 17. Table 3 summarizes the results.

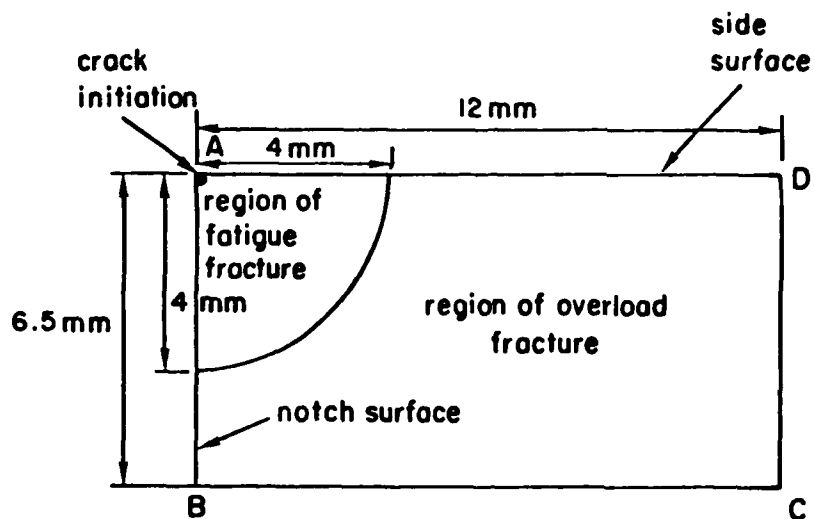


Figure 20. Schematic Diagram of Fracture Surface for Short-Crack Specimen.

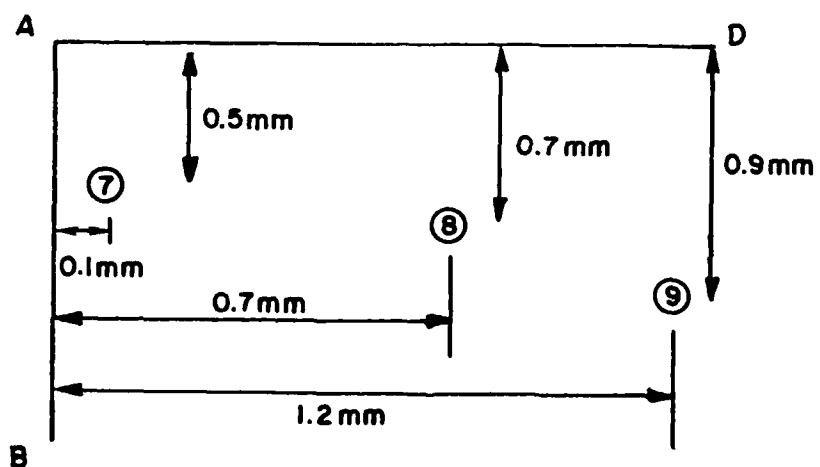


Figure 21. Enlarged Sketch of Fatigue-Fracture Region from Which SEM Micrographs Were Taken.



Crack Propagation



Figure 23. SEM Micrograph of Fracture Surface of Short-Crack Specimen at Region ⑧ in Fig. 21. Magnification 2000x.

Crack Propagation



Figure 22. SEM Micrograph of Fracture Surface of Short-Crack Specimen, at Region ⑦ in Fig. 21. Magnification 5000x.

Crack Propagation →



Figure 24. SEM Micrograph of Fracture Surface  
of Short-Crack Specimen at Region  
⑨ in Fig. 21. Magnification 2500 $\times$ .

TABLE 3  
COMPARISON OF RESULTS FOR SHORT- AND LONG-CRACK  
FATIGUE-CRACK-GROWTH RATES IN 7075-T651 ALUMINUM

LOCATION (see Fig. 23)	$\Delta K$ ksi $\sqrt{\text{in.}}$	SHORT CRACK* da/dN in/cycle	LONG CRACK+ da/dN in/cycle
7	6	$5.4 \times 10^{-6}$	$6 \times 10^{-7}$
8	15.9	$1.1 \times 10^{-5}$	$1.5 \times 10^{-5}$
9	19	$9 \times 10^{-6}$	$3 \times 10^{-5}$ (extrapolated)

\* Obtained from SEM micrographs and calbrating factor of 3.5.

+ Obtained from Fig. 17.

Note that at very short crack lengths, the crack-propagation rate for the short crack is one order of magnitude higher than that for the long crack. However, as the crack length increases, the short-crack propagation rate falls below the long-crack propagation rate. Of course, several approximations were used in making the comparisons, and also the striation spacings are not uniform. Therefore, the present data should be viewed with caution. At Location (7) the approximations are quite valid and, hence, the one-order-of-magnitude difference is believed to be a real effect. An interesting point to note is that at Location (9),  $K_{max}$  is beyond the fracture-toughness value. It is not clear why fatigue-crack propagation occurred well beyond this point. Of course, the large voids in Fig. 26 do suggest a considerable extent of overload fracture.

Based upon experience gained from this, the following future work is suggested:

- 1) Modification of the specimen design and use of the design shown in Fig. 25 which has three advantages. First, the COD is much smaller than in the case of Fig. 16. Second, it would be easier to take replicas from inside the notch. Third, the shorter width of the specimen would allow using an induction coil for heating purposes. The finite-element calculations on this geometry have already been completed. (Subsection 8 of this section.)
- 2) Electropolishing of the sample after mechanical polishing. A polishing agent consisting of 75% methanol and 25% nitric acid was found to be satisfactory. Cooling of the solution and use of approximately  $1.5 \text{ A/cm}^2$  for only 15 sec. would minimize grain-boundary etching. The electropolishing would remove all traces of scratches and also provide much better replicas.

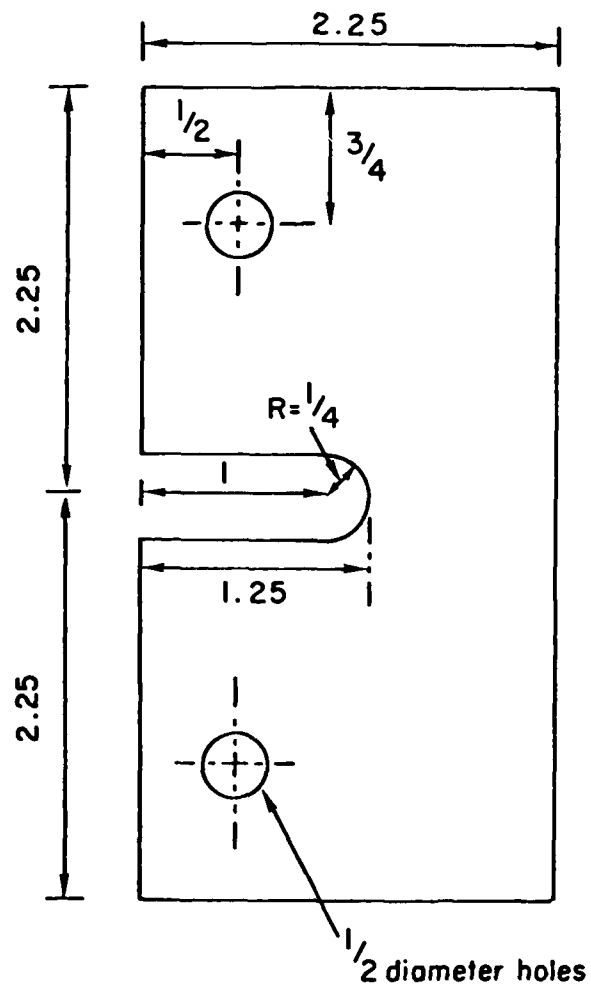


Figure 25. Wide-Notch Specimen (Dimensions in Inches).

- 3) Use of other replicating tapes in order to remove all bubbles.
- 4) Use of a dummy sample for obtaining an estimate of the crack-propagation life before the short-crack propagation test is carried out.

## 5. EVALUATION OF THRESHOLD TEST PROCEDURE

Testing of four specimens for an ASTM round-robin evaluation of the ASTM tentative test procedure<sup>40</sup> for determining  $FCGR < 10^{-8}$  m/cycle has been completed. The specimens tested were CT with  $W = 2.0$  in. and  $B = 0.30$  in. and were made from 2219-T851 aluminum. The objectives of the test program were to identify and resolve problem areas in the proposed test procedures and to assess the variability in low FCGR data within and among laboratories.

The ASTM tentative test procedure recommends a K-decreasing test phase followed by a K-increasing test phase. The FCGR from both of these phases are compared in order to evaluate the validity of the data. In the K-decreasing test phase, the stress-intensity factor decreases exponentially as a function of CG increment. The exponentially decreasing K provides a rate of change of plastic zone size with crack length which is proportional to the current zone size. The relationship for K or equivalently for the stress-intensity range,  $\Delta K$ , is given by

$$\Delta K = \Delta K_0 \exp [C(a-a_0)] \quad (27)$$

where  $\Delta K_0$  and  $a_0$  are the initial values of the stress-intensity range and crack length, respectively;  $a$  is the current crack length; and  $C$  is the constant of proportionality. For the recommended test procedure,  $C = -2.00 \text{ in.}^{-1}$ . Two of the four specimens were tested under this recommended test condition. The other two were tested to evaluate an optional decreasing-K condition, where  $C = -3.00 \text{ in.}^{-1}$ .

In the tests, K was decreased by manual load shedding in small steps such that the change in K was less than 10%. When the desired CGR was obtained

$\approx 10^{-10}$  m/cycle, the load was maintained at its current value. Then, for the CT test geometry, the stress-intensity factor increased as the crack continued to grow.

In the test procedure it is important to obtain a correlation between FCGR for decreasing- and increasing-K conditions. Since the data apply to the almost vertical portion of a FCGR curve, the rates become very sensitive to changes in test conditions. If a state of quasi-equilibrium does not exist during the test phases, unusual variations occur in the data due to transient conditions. Transients in FCGR may occur if, for example, a nonsteady equilibrium state exists in the chemical activity between the environment and the exposed fracture surface when the load change is too large in the K-decreasing test phase or if interruptions of too long a duration occur in the test phase. One condition for the FCGR data to be valid is that the FCGR's be similar for decreasing- and increasing-K conditions.

When valid data are obtained for  $FCGR < 10^{-8}$  m/cycle, an operational procedure is recommended for the determination of a threshold K level. A linear-regression analysis is applied to approximately equally spaced  $da/dN$  data between  $10^{-9}$  and  $10^{-10}$  m/cycle on a  $\log da/dN$  vs  $\log \Delta K$  plot. The intersection of the regression line with  $10^{-10}$  m/cycle FCGR will determine the  $\Delta K$  threshold level. This value of FCGR is chosen, in part, because it represents a lower limit to a continuous CG process. At  $10^{-10}$  m/cycle the atomic bonds between single atoms or molecules are broken in each cycle; therefore, the process is one in which CG increments occur as isolated events along the crack front.

Typical examples of the FCGR obtained from the test procedure are shown in Figs. 26 and 27. The threshold FCGR under the decreasing-K condition, Fig. 26, were obtained from data on crack length versus cycle count using the secant data-reduction method.<sup>40</sup> Since the load was shed in increments  $\approx 10\%$  of maximum load, the FCGR data which were produced in the first CG increment may be altered by the load change. The data obtained when the load was changed are denoted in Fig. 26 by the rhombus symbols. In several instances the transient FCGR data appear to lie outside the general

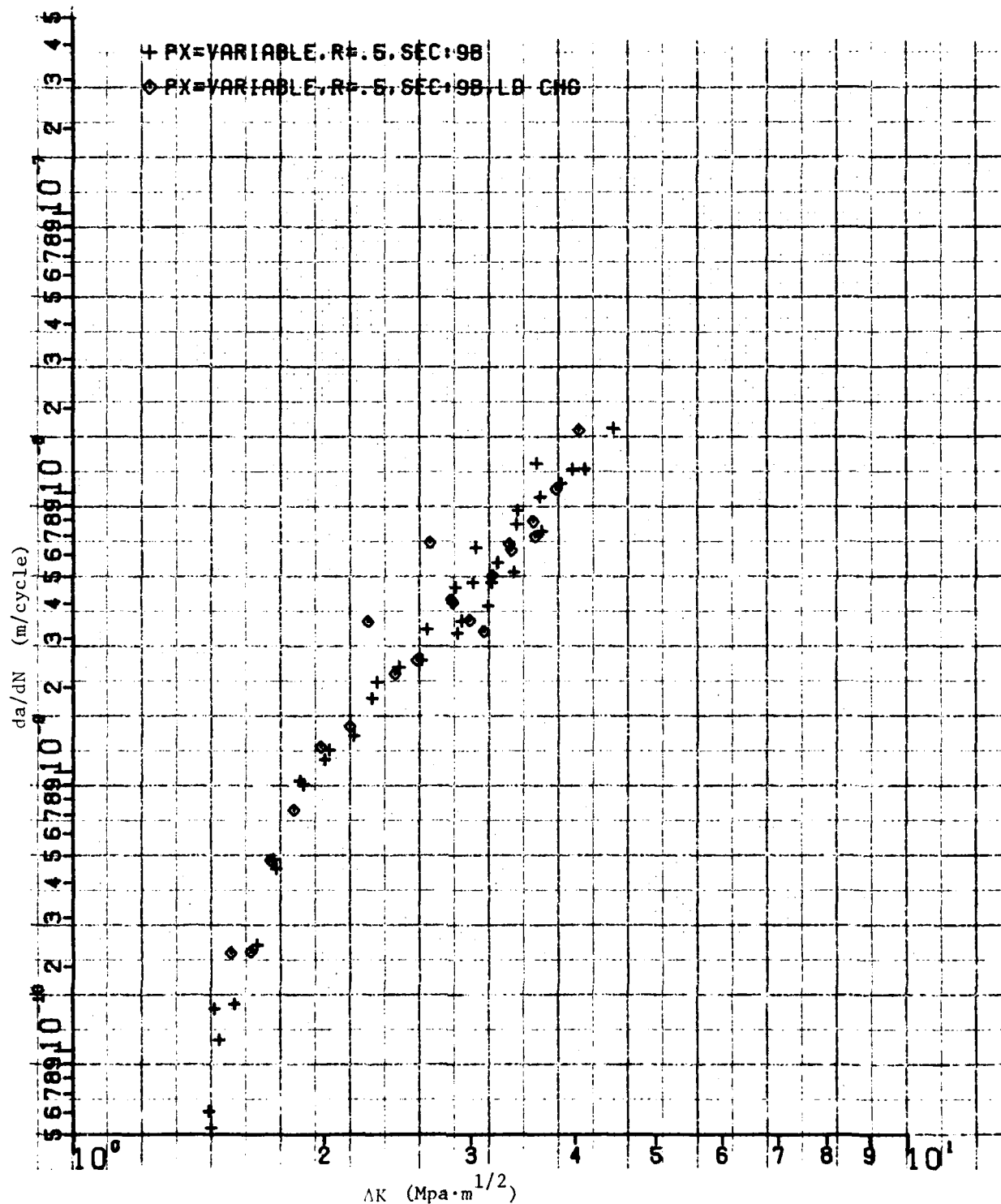


Figure 26. Threshold Fatigue-Crack-Growth Rates under Decreasing-K Conditions for 2219-T851 Aluminum in Laboratory Air at 40 Hz.



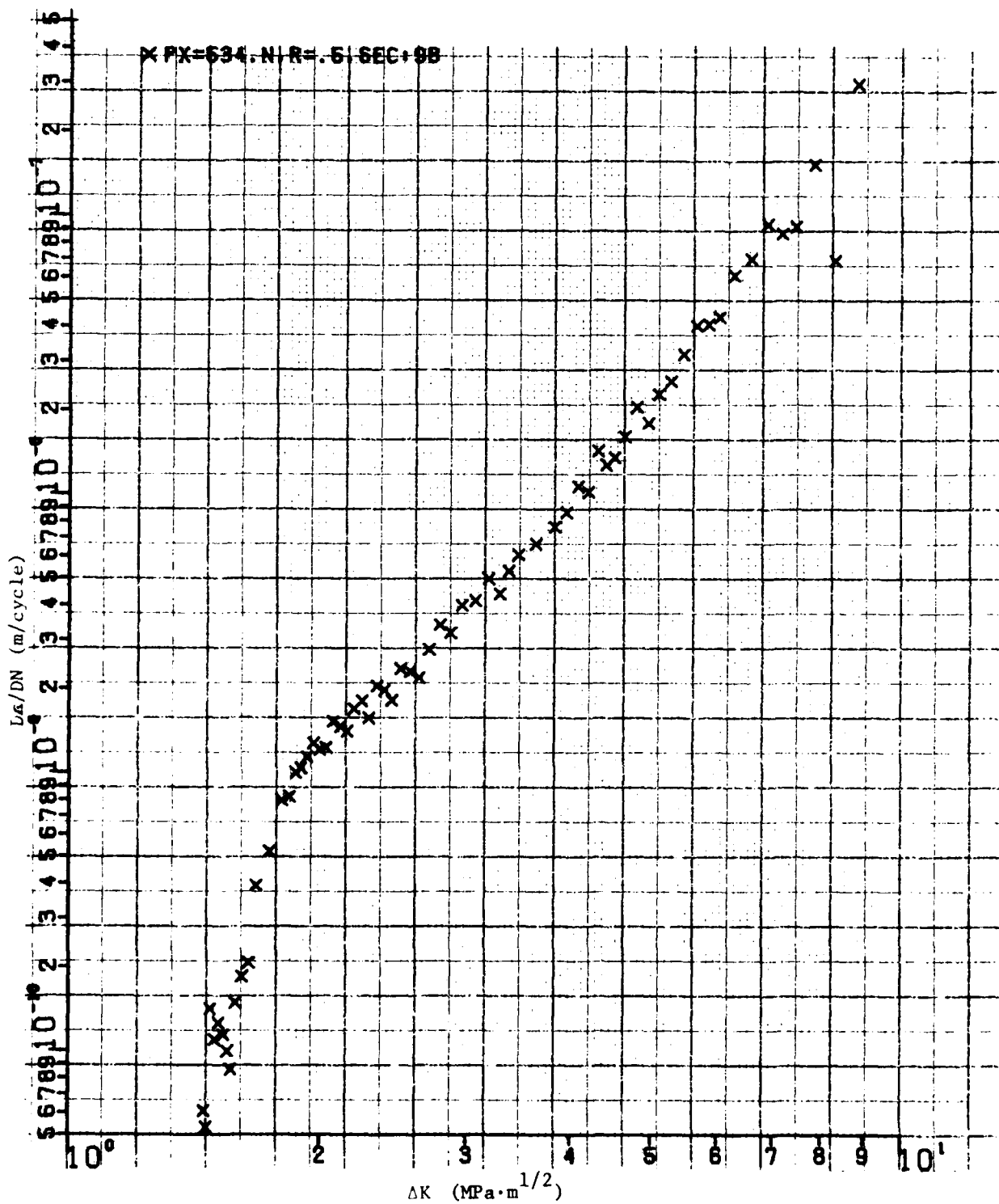


Figure 27. Threshold and Higher Fatigue-Crack-Growth Rates under Increasing- $K$  Conditions for 2219-T851 Aluminum in Laboratory Air at 40 Hz.

scatter band of the data obtained when the load was not changed. The threshold FCGR under the increasing-K condition, Fig. 27, were also obtained using the secant data-reduction method. The data under decreasing- and increasing-K conditions are almost coincident. Thus, they would be considered valid data. Valid threshold data were obtained from all four specimens.

The threshold K values at  $FCGR = 10^{-10}$  m/cycle are given in Table 4. Some significant differences appear to exist between the results for the two values of C for the decreasing-K condition.

#### 6. STUDY OF CRACK-GROWTH RESISTANCE USING POLYCARBONATE AS A MODEL MATERIAL

An experimental program was conducted to investigate the characterization of stable crack growth by the J-integral method using polycarbonate (PC) as a model material. Deeply cracked three-point-bend specimens were tested having ratios of crack length to width of 0.6 to 0.8 and thicknesses ranging from 25.4 to 3.2 mm (1 to 1/8 in.). The J-integral was found to provide a good measure of crack initiation and growth in polycarbonate. No effect of thickness or crack length upon fracture behavior was found over the range tested. Critical values of J were 9 psi-in. at the beginning of crack growth, 25 psi-in. at 2% crack extension, and 41 psi-in. at pop-in. The crack growth exhibited an exponential relationship with J. Data in the literature on other materials were found which also obeyed this exponential relationship. Using this relation, a new method of determining  $J_{IC}$  and a logarithmic tearing modulus were developed.

Details of this investigation are reported in an AFWAL Technical Report entitled, "A Study of the J-Integral Method Using Polycarbonate," which has been submitted for publication.<sup>41</sup>

TABLE 4

THRESHOLD K OBTAINED FOR 2219-T851 ALUMINUM IN  
THE ASTM ROUND-ROBIN TEST-PROCEDURE EVALUATION

SPEC ID	C (in. <sup>-1</sup> )	$K_{th}$ (MPa·m <sup>1/2</sup> )	
		Decreasing-K Test	Increasing-K Test
9A	-2	1.326	1.225
17D	-2	1.286	1.290
9B	-3	1.468	1.487
17C	-3	1.537	1.485

## 7. CHARACTERIZATION OF STABLE CRACK GROWTH USING POLYCARBONATE AS A MODEL MATERIAL

The deflection-rate-controlled tests and the constant-load tests on PC three-point-bend specimens at temperature were conducted in order to evaluate both the relationship between compliance and crack-front shape and the characterization of the growth of the crack. The test matrix is described in Table 5. Crack-length measurements were made from the photographs taken through an end of the specimen during the test. Crack lengths were determined from the average of the three crack-length measurements made at one-quarter, one-half, and three-quarters of the thickness of the specimen. Even though tunneling occurred in all specimens without side grooves, the crack front remained fairly straight in the specimen interior across 80 to 90% of the thickness. The crack lengths from the three measurements did not vary by more than  $\pm 4\%$  from the average crack length.

Crack-growth rates (in./min.) and stress-intensity factors were computed by means of the incremental polynomial method which is described in the ASTM 647-80T Test Method. Plots of crack-growth rate as a function of stress-intensity factor have the shape of an inverted "V". These results indicated that the stress-intensity factor could not be used for correlating the crack-growth rates observed in these tests. Hence, the stress-intensity parameter was not an adequate parameter to use in the characterization of the stable crack growth in PC when creep deformations occurred in the remaining ligament of the specimen.

The results also indicated that compliance measurements on the specimens without side grooves--obtained at periodic intervals by partially unloading and reloading the specimen during the tests--did not provide an accurate means for determination of an effective crack length. All unloading and reloading was conducted at a deflection rate which was ten times greater than the deflection rate used in the test. For Specimen PC-SCG-178 the deflection rate for unloading and reloading was 100 times greater than the test deflection rate. There are two reasons for the lack

TABLE 5  
PC TEST MATRIX FOR CRACK-GROWTH CHARACTERIZATION  
Test Temperature: 71°C (160°F)

<u>Load Conditions</u>		<u>Specimen I.D. and Remarks</u>		
<u>Approximate Load Point Deflection Rate (in./min.)</u>	<u>Constant Load (lb)</u>	<u>With Compliance Measurements</u>	<u>Without Compliance Measurements</u>	<u>Side Grooves With Compliance Measurements</u>
0.02		PC-SCG-15	PC-SCG-175 PC-SCG-174	
0.006		PC-SCG-16		
0.004				PC-SG-171
0.002		PC-SCG-14	PC-SCG-177	
0.0006		PC-SCG-173		PC-SG-172
0.0003		PC-SCG-178		
	365		PC-SCG-171	
	455		PC-SCG-172	

of consistency in crack lengths obtained from compliance measurements and observed crack lengths:

- 1) creep deformations were occurring, even under the increased unloading and loading rate, and
- 2) the highly deformed material near the sides of the specimen created three-dimensional loading on the specimen, whereas the compliance-crack length relationship was based upon two-dimensional analysis.

Data from the PC specimens with smooth sides were reduced to obtain the  $C^*$  parameter which has been used in the literature to characterize time-dependent stable crack growth. Preliminary results indicated that  $C^*$  is not an appropriate parameter for the characterization of CGR. The time rate of energy input per unit thickness,  $\dot{U}/B$ , into a specimen having crack length  $a$  is shown in Fig. 28 for the seven displacement-rate tests on specimens with smooth sides in Table 5. From the data shown in Fig. 28, a linear relationship was chosen for the least-squares error fit to each set of displacement-rate data. As a result, the values of  $C^* \equiv -(\delta\dot{U}/\delta a)_\delta/B$  are constant for each test.

Thus, the plot of CGR,  $da/dt$ , versus  $C^*$ , Fig. 29, was a set of vertical data points. No correlation existed between  $da/dt$  and  $C^*$  for a given test, and no correlation existed among the data from the various tests. The test data which were used to evaluate  $C^*$  were taken from the decreasing side of the loading curve. Using data from the increasing side of the loading curve produced negative values of  $C^*$ , implying that energy is increasing in the specimen rather than being released at the crack tip. This inconsistency between crack growth and energy change in the specimen can, for the most part, be attributed to the assumed constitutive relation between stress and strain rate used in the development of the  $C^*$  parameter.

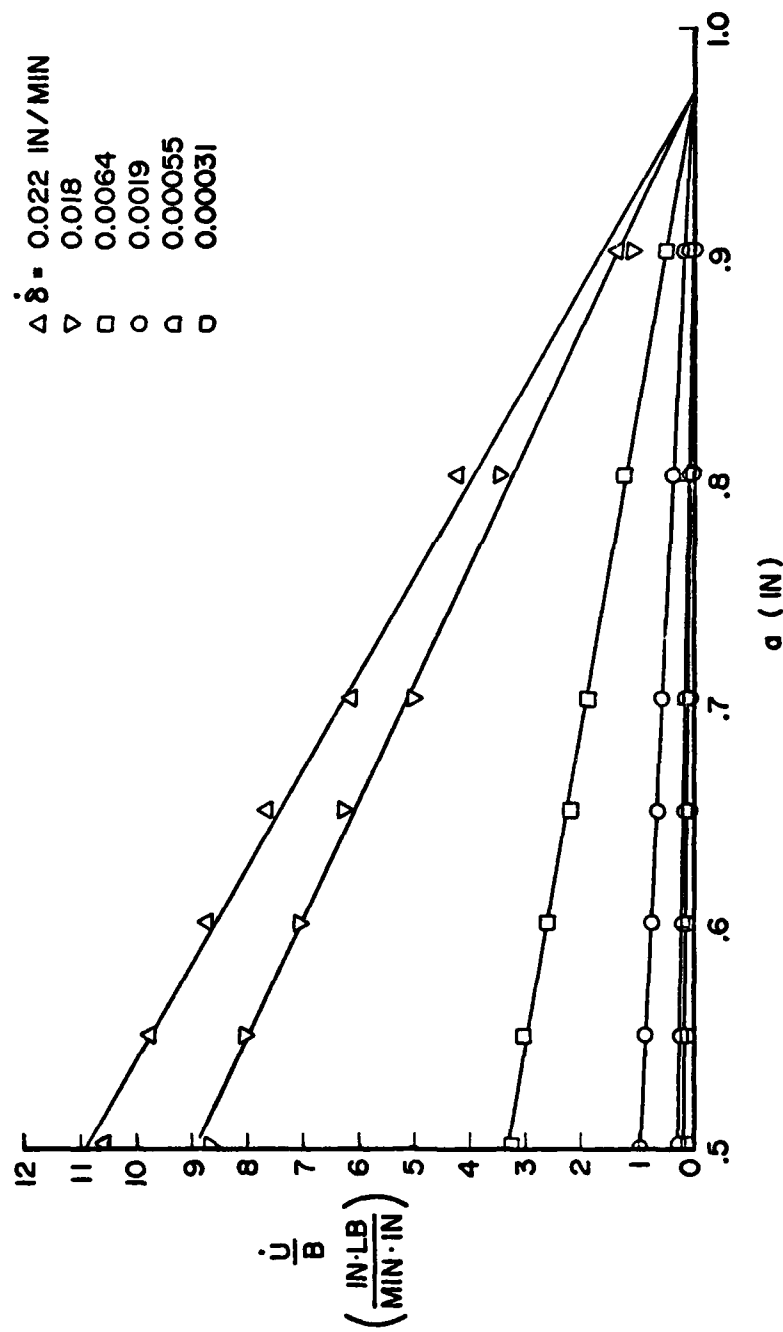


Figure 28. Plot of Time Rate of Change of Strain Energy Per Unit Thickness as a Function of Crack Length for Various Constant Load-Displacement Rates.

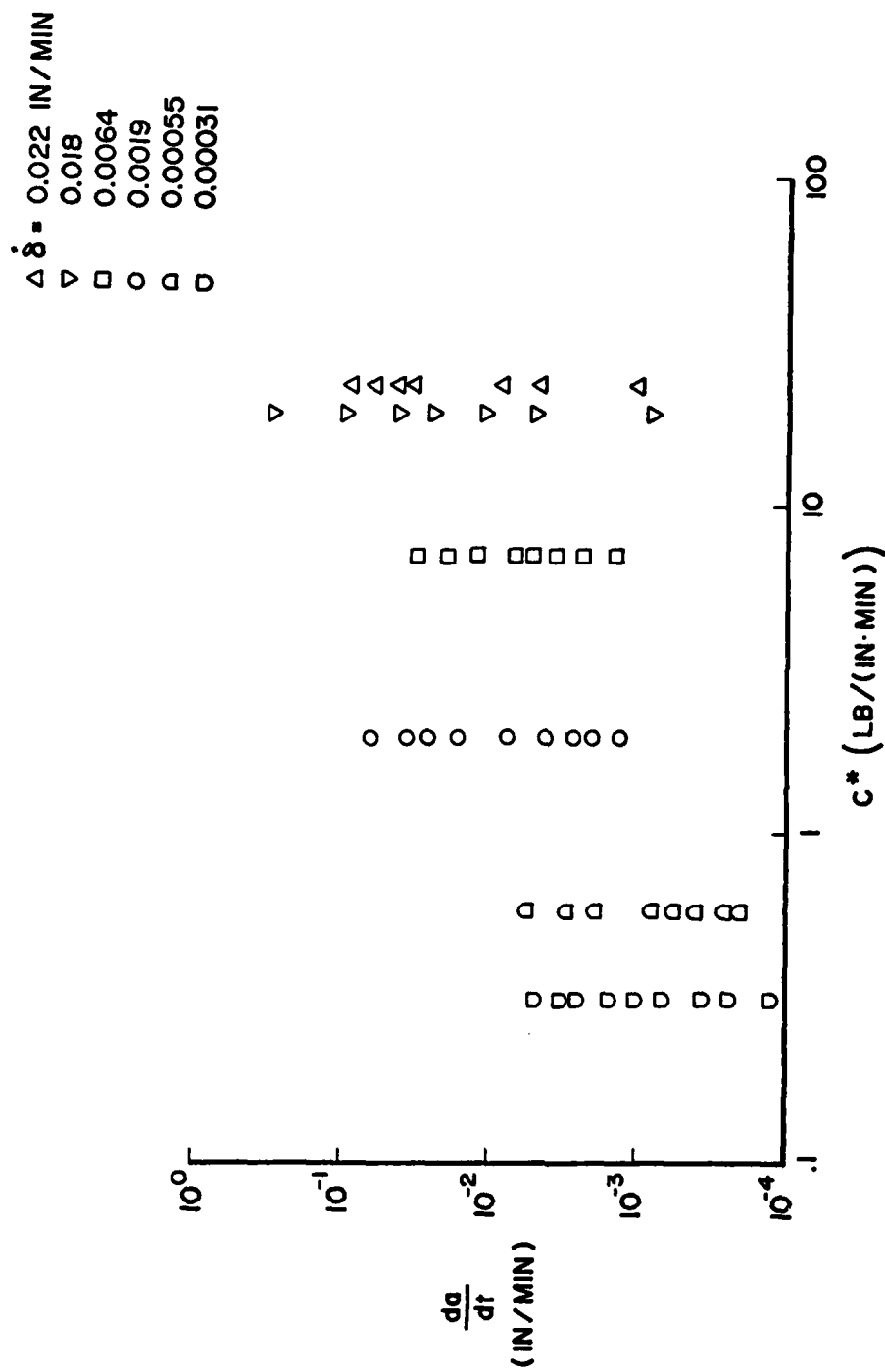


Figure 29. Log-Log Plot of Crack-Growth Rate as a Function of  $C^*$  for Polycarbonate Three-Point-Bend Tests.



The type of relationship in Fig. 29 between  $da/dt$  and  $C^*$  is similar to the relationship found earlier between  $da/dt$  and the stress-intensity factor  $K$  for crack growth under decreasing load. The right side of the inverted "V" curve for  $da/dt$  versus  $K$  was almost vertical, that is, the CGR occurs at constant  $K$  and is associated with crack growth under decreasing load.

The CGR under decreasing loading which occurred at constant  $K$  was also obtained from tests of side-grooved specimens. In addition the growth rate that occurred under increasing load coincided better with the rate under decreasing load for the side-grooved specimens than for the smooth specimens. Since the side-grooved specimens exhibited very little tunneling in their crack-growth behavior, the inverted "V" crack-growth behavior was attributed to formation of crack tunneling in the smooth specimens. Thus, a model of crack-growth behavior should incorporate the two distinct phenomena--a propagating crack front in the interior of the material and the regions near the side surfaces which stretch rather than crack and form the sides of the crack tunnel.

## 8. FINITE-ELEMENT ANALYSIS OF TEST SPECIMENS

### a. Ring and Partial Ring Geometries

A ring-shaped (annulus) geometry containing a single radial crack was analyzed by the technique described in Ref. 42 for two loading conditions. Diametrically opposite tensile loads were applied at the inner radius, and the crack at the inner radius was perpendicular to the load line, Fig. 30(a). Also, diametrically opposite compressive loads were applied at the outer radius, and the crack at the inner radius was coincident with the load line, Fig. 30(b).

It was shown that for inner-radius-to-outer-radius ratios of one-half and less, Mode I stress-intensity factors for the ring geometry were essentially proportional only to the load over a range of non-dimensional

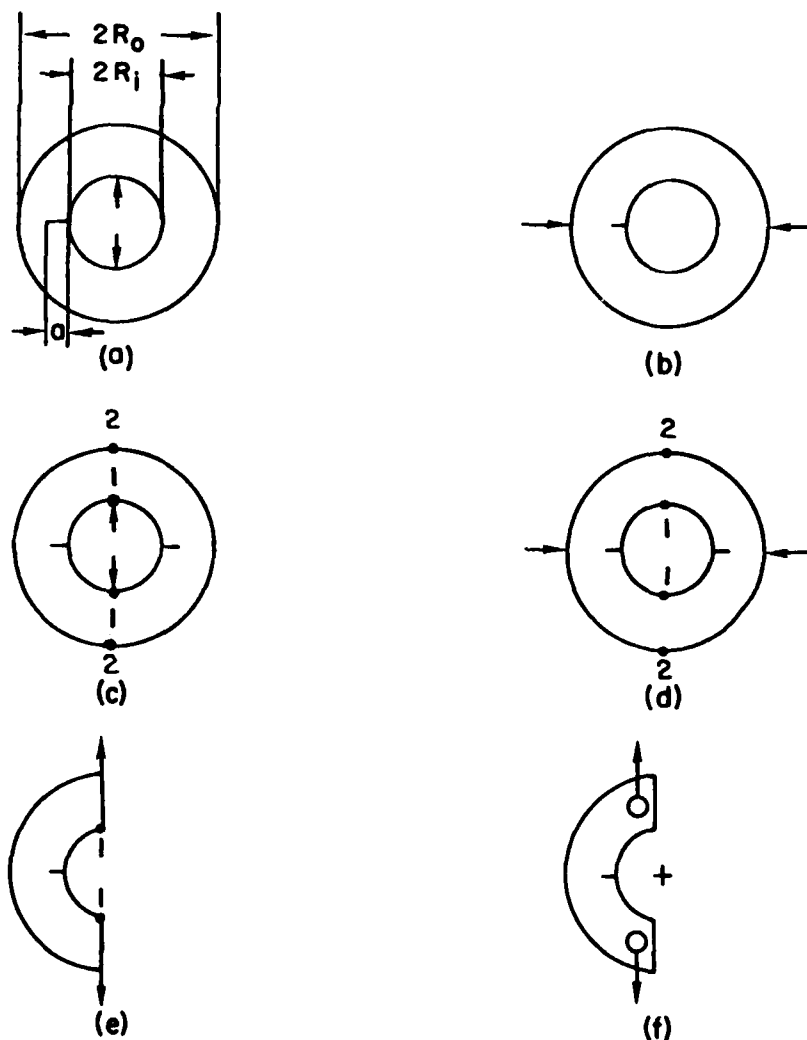


Figure 30. Schematic Diagram of Rings and Partial Rings with Cracks.

- a) Single-Notch Tension (SNT) Specimen.
- b) Single-Notch Compression (SNC) Specimen.
- c) Double-Notch Tension (DNT) Specimen.
- d) Double-Notch Compression (DNC) Specimen.
- e) Notched Tension Half-Ring (NTH) Specimen.
- f) Notched Tension Modified-C (MC) Specimen.

crack lengths. The ring specimens under tensile loads were used in experiments involving parametric crack-growth studies where the variation of the stress-intensity factor for a constant applied load was to be eliminated.

More detailed results of the analysis are reported in a paper entitled, "Constant  $K_I$  Crack-Propagation Test Specimens," which will be published in the International Journal of Fracture.

A ring-shaped geometry containing two collinear radial cracks emanating from the inner radius of the annulus has been analyzed under tensile and compressive loading conditions, Figs. 30(c) and (d), respectively. As in the above description of the loads, the two cracks coincided with the load line for the compressive loads on the outer radius and were perpendicular to the load line for the tensile loads on the inner radius. Also a half-ring having a crack emanating from the inner radius has been analyzed with collinear tensile loads being applied to the ends, Fig. 30(e).

For more efficient utilization of the material in the ring specimens, an analysis was conducted on a portion of a ring which would be obtained by removing a section of material containing the cracked surfaces for the single- or double-cracked ring specimen, thereby preserving the fracture surfaces. For the single-cracked ring, an equivalent section of material would be removed on the diametrically opposite side of the ring. Two pieces of the ring referred to as modified C-shaped specimens would be left which would subtend an arc of slightly less than  $180^\circ$ , Fig. 30(f). The modified C-shaped specimens were loaded in tension.

An AFVAL Technical Report<sup>43</sup> will be published which tabulates results for the stress-intensity factors and certain displacements for the double-cracked ring and the modified C-shaped specimens. These results were obtained for various ratios of inner to outer radius and crack lengths by the technique described in Ref. 42. Mathematical expressions were determined by a least-square error fit to some of the pertinent finite-element results.

b. Keyhole and Wide-Notch Specimens

Analysis of keyhole and wide-notch specimens by the technique described in Ref. 42 was conducted in support of the preliminary investigation of the propagation of short cracks at notches (Subsection 4 of this section). The reasons for the particular design of the keyhole specimen, Fig. 16, have been discussed in the previous subsection. Testing of the specimen commenced before the finite-element analysis was completed because specimen fabrication was completed ahead of schedule and the test equipment was available. The hoop stresses at the critical points A and B, Fig. 16, around the hole in the unflawed specimen were 37.4 and 87.6 psi per pound of applied load per inch thickness, respectively. The experimental results were consistent with the stress calculation because the fatigue crack initiated at the highest stress location, Point B.

As a result the geometry was modified, and an analysis was conducted on the wide-notch design shown in Fig. 25. For this unflawed specimen the maximum stress occurred at the root of the notch at the plane of symmetry. The stress-intensity factors for various crack lengths emanating from the notch along the plane of symmetry are summarized in Table 6, where the units are  $\text{psi}\sqrt{\text{in.}}$  per pound of applied load per inch thickness.

c. Three-Dimensional Results for Some Test-Specimen Configurations

A three-dimensional elastic finite-element-analysis program was developed. The program was based upon 20-node isoparametric brick elements and contained special provision for introducing the elastic stress singularity at the crack tip. The program was used to analyze a three-point-bend specimen with a span to width ratio  $S/W = 4$  and crack length to width ratio  $a/W = 0.375$  and a ring tension specimen with the ratio of inner radius to outer radius  $R_i/R_o = 0.5$  and a ratio of crack length to width of the ring  $a/(R - R_i) = 0.5$  for each of the two collinear cracks, Fig. 30(c). Through-the-thickness (z-direction) results of these analyses are shown in Tables 7 and 8. A uniformly distributed line load was used as the boundary condition for both geometries. In both cases it was found that the mid-plane results were comparable to the corresponding two-dimensional-analysis results.

TABLE 6  
STRESS-INTENSITY FACTORS FOR A WIDE-NOTCH SPECIMEN

(Specimen geometry shown in Fig. 25)

Crack Length (in.)	Stress-Intensity Factor (psi $\sqrt{\text{in.}}$ /lb./in.)
0.0833	5.91
0.165	7.32
0.250	8.81

TABLE 7  
RESULTS FOR THREE-POINT-BEND SPECIMEN (THREE DIMENSIONAL)  
 $a/W = 0.375$ ,  $S/W = 4$

$z/B$	$Y$	$C$	$\delta$
0.0	7.3345	18.4378	40.04319
0.201	7.2799	18.4265	40.1597
0.402	6.6124	18.3780	40.6013
0.406	6.1522	18.3226	40.8306
0.500	5.6431	18.2424	41.1274

Mid-plane →

Specimen surface →

$$Y = \text{stress-intensity factor (nondim.)} = \frac{K_I B \sqrt{W}}{P}$$

$$C = \text{crack-mouth compliance (nondim.)} = \frac{EB(COD)}{P}$$

$$\delta = \text{load-point compliance (nondim.)} = \frac{EBV}{P}$$

TABLE 8  
RESULTS FOR RING TENSION SPECIMEN WITH TWO CRACKS (THREE DIMENSIONAL)  
 $a/(R_o - R_i) = 0.5, R_i/R_o = 0.5$

$z/B$	$Y$	$C/2$	$\delta_1/2$	$\delta_2/2$
0.000	4.3214	4.3407	10.1740	8.3265
0.201	4.2899	4.3311	10.1992	8.3472
0.402	3.8897	4.3266	10.3109	8.4385
0.406	3.6246	4.3141	10.3693	8.4861
0.500	3.3193	4.2952	10.4428	8.5547

$Y = \text{stress-intensity factor (nondim.)} = \frac{K_I B \sqrt{R_o}}{P}$

$C = \text{crack-mouth compliance (nondim.)} = \frac{ER(COD)}{P}$

$\delta_1 = \text{load-point compliance (nondim.)} = \frac{EB2V_1}{P}$

$\delta_2 = \text{compliance between two points on outer radius at the load line (nondim.)} = \frac{EB2V_2}{P}$

The crack-mouth opening and the load-point displacement for the three-point-bend specimen were higher for the three-dimensional analyses than for a two-dimensional plane-stress finite-element analysis and for other results in the literature. Since a plane-strain constraint should develop in the interior of the specimen around the crack front for the three-dimensional problem, the displacements should be slightly lower than the two-dimensional plane-stress results. It is possible that the three-dimensional results were higher because the values of the nodal forces imposed as a boundary condition on the sides of elements were not computed properly for a 20-nodal element and a uniformly distributed line load. However, the total load is correct. Also, a constant displacement condition may have been a more satisfactory condition to impose than the condition of uniformly distributed loads along the sides of the specimen.

d. Analytical Modeling of the Mechanical Aspects of Fatigue Crack Growth

A program to estimate the Dugdale plastic zone size using finite-element methods was completed. The accuracy of the program was assessed by solving the problem of the center-crack panel for two different crack lengths. The results were found to be in good agreement with other results available in the literature. The program was then used to analyze compact-tension and WOL specimen geometries for  $0.4 \leq A/W \leq 0.8$ . The development of this program was a preliminary step in the development of a predictive crack-growth model based, in part, upon the crack-closure phenomenon and the plastic zone ahead of the crack tip. In addition to the crack-growth model, these results should provide "improved" initial conditions for an elastic-plastic-analysis algorithm.



### SECTION III

#### EXPERIMENTAL INVESTIGATIONS TO DETERMINE MECHANICAL PROPERTIES AND RELIABILITY OF STRUCTURAL MATERIALS

A large number of highly diverse and basic experiments were conducted to generate data on the mechanical properties and reliability of structural materials used in airframes and gas-turbine engines in aircraft under a variety of loading and environmental conditions as required in AFWAL R&D programs. The data were generated on the mechanical behavior with specific emphasis being placed upon the fracture, fatigue, and crack-growth behavior of structural materials for airframes and metal alloys and ceramics for advanced gas-turbine engines. The materials investigated included nickel-base superalloys, ( $\alpha$ - $\beta$ ) titanium alloys, high-strength low-alloy steels, structural ceramics, and other structural materials.

##### 1. TYPES OF TESTS

The types of mechanical tests included the following:

- 1) Room-temperature uniaxial tension and compression tests using Instron testing machines.
- 2) Creep and uniaxial tension and compression tests at temperatures up to 760°C (1400°F) utilizing Instron and servo-controlled MTS machines and creep frames with both resistance and inductance heating systems.
- 3) Low-cycle-fatigue crack-initiation experiments at room and elevated temperatures utilizing servo-controlled MTS machines.
- 4) Sustained-load crack-growth experiments at room and elevated temperatures utilizing Instron, MTS machines, and creep frames or special sustained-load fixtures.

- 5) Fatigue experiments under cyclic loading utilizing resonant Schenck fatigue machines or servo-controlled MTS machines
  - a) to produce a fatigue precrack,
  - b) to generate FCGR data (e.g.,  $da/dN$  vs.  $K$ ),
  - c) to determine fatigue life (i.e., S-N curves), and
  - d) to evaluate the effects upon crack growth of single and multiple overloads and underloads.
- 6) FCGR experiments under programmable spectrum loading utilizing servo-controlled MTS machines, Wavetek function generators, and the U.S. Data Control System.

## 2. INVESTIGATIONS SUPPORTED BY DATA OBTAINED IN FACILITY

The reduced and analyzed data generated in this program were used in the following reports and papers:

"Influence of Surface Conditioning on the Fatigue Properties of Ti-6Al-2Sn-4Zr-2Mo-0.2Si," Y. Mahajan, S. Fujishiro, L. R. Bidwell, and F. H. Froes, Proceedings of Fourth International Titanium Conference held in Kyoto, Japan, May 1980.

"Microstructure Property Correlation in Cold-Pressed and Sintered Elemental Ti-6Al-4V Powder Compacts," Y. Mahajan, D. Eylon, and F. H. Froes, Proceedings of the AIME Conference on Titanium Powder Metallurgy held in Las Vegas, NV, February 1980.

"Fatigue Crack Initiation of Titanium Alloy Powder Compacts," D. Eylon, Y. Mahajan, N. Ontoko, and F. H. Froes, Proceedings of the AIME Conference on Titanium Powder Metallurgy held in Las Vegas, NV, February 1980.

"The Effect of Microstructure and Microstructural Integrity on the Mechanical Properties of Ti-6Al-4V PM Products," F. H. Froes,

D. Eylon, and Y. Mahajan, Proceedings of the 1980 International Powder Metallurgy Conference, Washington, D. C., June 22-27, 1980, Modern Developments in Powder Metallurgy, Vols. 12-14.

"Fracture Behavior of Blended Elemental P/M Titanium Alloys," P. J. Anderson, V. M. Svoyatytsky, F. H. Froes, Y. Majahan, and D. Eylon, Proceedings of the 1980 International Powder Metallurgy Conference, Washington, D. C., 22-27 June 1980, Modern Developments in Powder Metallurgy, Vols. 12-14.

"Improvement of Ti Alloy Fatigue Properties by Pt Ion Plating," S. Fujishiro and D. Eylon, Metallurgical Transactions, Volume 11A, August 1980.

"Formability of a Mechanically-Alloyed High Strength P/M Aluminum Alloy IN-9051," Y. W. Kim and L. R. Bidwell, TMS-AIME Fall Meeting, Pittsburgh, PA, October 5-9, 1980; a complete version to be published in Metallurgical Transactions.

"Grain Size and Fatigue Crack Growth Relationships in P/M Al-Mg Alloy, IN-9051," Y. W. Kim and L. R. Bidwell, 110th TMS-AIME Annual Meeting, Chicago, IL, February 24-28, 1981; also to be published in Metallurgical Transactions.

"The Effects of Thermo-Mechanical Processing on the Tensile Properties of an Al-Fe-Ni P/M Alloy," Y. W. Kim and L. R. Bidwell, 110th TMS-AIME Annual Meeting, Chicago, IL, February 24-28, 1981; also to be published in Metallurgical Transactions and accepted for publication by Scripta Metallurgica, May 1981.

"A Comparison of Microstructure and Properties of Equivalent Strength Ingot Metallurgy and Powder Metallurgy 7XXX Aluminum Alloys," S. Doerr, Thesis, The Ohio State University Graduate School, Department of Metallurgical Engineering, Quarter/Year Winter/81.

"Crack Growth Behavior of Alloy IN100 Under Sustained Load at 732°C (1350°F)," R. C. Donath, AFWAL TR-80-4131 (Air Force Wright Aeronautical Laboratories, Wright-Patterson Air Force Base, OH, 1980).

"Load Sequence Crack Growth Transients in a Superalloy at Elevated Temperature," J. M. Larson and T. Nicholas, 14th National Symposium of Fracture Mechanics, UCLA, Los Angeles, CA, June 30-July 2, 1981.

"An Experimental Investigation of Creep Crack Growth in IN100," R. C. Donath, T. Nicholas, and L. S. Fu, 13th National Symposium of Fracture Mechanics, ASTM, Philadelphia, PA, June 14, 1980.

"High Integrity Titanium Alloy Shapes by Powder Metallurgy," D. Eylon and F. H. Froes, Symposium on Titanium and its Alloys for Surgical Implants, Phoenix, AZ, May 11-12, 1981.

"Fatigue Control in Prealloyed Titanium Powder Compacts," F. H. Froes and D. Eylon, MPIF Conference, Philadelphia, PA, May 4-6, 1981.

D. W. Becker, W. A. Baeslack, III, F. Mullins, and F. H. Froes, "Circumventing Fusion Welding Problems in High-Strength Titanium Alloys," Technical Memorandum LL-78-1 (Air Force Materials Laboratory, Wright Patterson Air Force Base, OH, March 1979).

W. A. Baeslack, III and Y. Mahajan, "Intergranular Fracture of Heat-Treated Weldments in a High-Strength, Alpha-Beta Titanium Alloy," Scripta Metallurgica, p. 959, October 1979.

W. A. Baeslack, III, and D. W. Becker, "Fusion Zone Fracture Behavior in Titanium Alloy Weldments," Metallurgical Transactions A, p. 1803, November 1979.

Y. Mahajan and W. A. Baeslack, III, "Transgranular Fracture of Weldments in a High-Strength, Alpha-Beta Titanium Alloy," Scripta Metallurgica, p. 1125, December 1979.

D. W. Becker and W. A. Baeslack, III, "Property-Microstructure Relationships in Metastable-Beta Titanium Alloy Weldments," *Welding Journal*, Research Supplement, p. 85s, March 1980.

W. A. Baeslack, III, and D. W. Becker, "Substructure Characteristics of Titanium Alloy Weldments," *Metallurgical Transactions A*, p. 605, April 1980.

W. A. Baeslack, III, and Y. Mahajan, "Alpha-Beta Interface Sliding in Titanium Alloy Weld Metals," *Metallurgical Transactions A*, p. 1234, July 1980.

D. W. Becker, W. A. Baeslack, III, and F. H. Froes, "Welding of PM CORONA-5 Product," Powder Metallurgy of Titanium Alloys (F. H. Froes and J. E. Smugersky, Eds.) (The Metallurgical Society of AIME, 1980), p. 217.

W. A. Baeslack, III, D. W. Becker, and F. H. Froes, "Welding of an Advanced, High-Toughness Titanium Alloy," Titanium '80 - Science and Technology, Proceedings of the 4th International Conference on Titanium (H. Kimura and O. Izuma, Eds.) (The Metallurgical Society of AIME, 1981), p. 269.

D. W. Becker, R. Messler, and W. A. Baeslack, III, "Joining of Titanium Alloys - A Critical Review," Titanium '80 - Science and Technology, Proceedings of the 4th International Conference on Titanium (H. Kimura and O. Izuma, Eds.) (The Metallurgical Society of AIME, 1981), p. 235.

Y. Mahajan, D. W. Becker, and W. A. Baeslack, III, "Grain Boundary Deformation in a Metastable-Beta Titanium Alloy," *Journal of Materials Science*, April 1981.

S. L. Bostin and W. A. Baeslack, III, "Microstructure-Property Relationships in GTA Welded Ti-10V-2Fe-3Al," Technical Memorandum AFWAL-MLL-81-1 (Air Force Wright Aeronautical Laboratories, Wright-Patterson Air Force Base, OH, 1981).

W. A. Baeslack, III and C. M. Banas, "A Comparative Evaluation of Laser and Gas Tungsten-Arc Weldments in High-Temperature Titanium Alloys," 1981 AWS National Meeting; to be published in the Welding Journal.

W. A. Baeslack, III, "Technical Note - Evaluation of Triplex Heat-Treatments for Alpha-Beta Titanium Alloys," to be published in the Welding Journal.

W. A. Baeslack, III, "Effect of Solute Banding on Solid-State Transformations in Titanium Alloy Weldments," to be published in Metallurgical Transactions A.

W. A. Baeslack, III, and F. Mullins, "Heat Treatment Response of Continuously Cooled Ti-4.5Al-5Mo-1.5Cr," to be published in Scripta Metallurgica.

W. A. Baeslack, III, "Microstructure-Property-Fracture Relationships in a High-Toughness PM Titanium Alloy - A Metallography Study," to be published in Metallography - An International Journal.

W. A. Baeslack, III, D. W. Becker, and F. H. Froes, "Welding of Advanced Titanium Alloys - A Survey," to be published in Journal of Metals.

W. A. Baeslack, III, and F. Mullins, "Influence of Cooling Rate on the Structure and Properties of Weldments in a Near-Alpha Titanium Alloy," to be published in Metallurgical Transactions A.

W. A. Baeslack, III, and D. W. Becker, "Welding of Advanced Titanium Alloys - An Interpretive Report," to be published as a Welding Research Council Bulletin.

F. Mullins, D. W. Becker, and W. A. Baeslack, III, "Elevated Temperature Properties of Weldments in Advanced High-Temperature Titanium Alloys," AFWAL Technical Report, to be published in August 1981.

W. A. Baeslack, III, "Fracture and Fatigue Behavior of Weldments in ELI Ti-CORONA 5," 1981 ASM National Meeting, New Orleans, LA; published in the Proceedings.

### 3. MODULUS AND MECHANICAL PROPERTIES OF IN100 AT ELEVATED TEMPERATURES

Results of modulus determinations of IN100 at room temperature (70°F) and at 800, 1000, 1200, and 1350°F are shown in Table 9. The tests were conducted on round tensile specimens with threaded ends and a test section with 1/4-in. diam. and 1-in. gage length. All modulus values were determined at a strain rate of 0.004 in./in./min. These specimens were subsequently tested at various strain rates to failure at 1350°F. The mechanical properties obtained from these tests are listed in Table 10. A plot of true stress versus engineering strain is shown in Fig. 31.

TABLE 9

YOUNG'S MODULUS FOR IN100 AT  
0.004 IN./IN./MIN. NOMINAL STRAIN RATE

Specimen ID	Average Modulus (Mpsi)				
	Number of Measurements				
	% Difference between minimum value and average value of modulus.				
	% Difference between maximum value and average value of modulus.				
Specimen ID	Temperature (°F)				
	70	800	1000	1200	1350
ENTEN-1	30.4	27.3	26.4	24.6	23.9
	4.	6.	6.	5.	6.
	-0.9	-1.9	-2.3	-1.3	-2.9
	+0.7	+1.4	+1.8	+1.9	+2.5
ENTEN-4	31.3	28.6	27.9	26.8	24.7
	4.	2.	1.	2.	2.
	-1.6	-0.5	-	-0.8	-1.2
	+2.2	+0.5	-	+0.8	+1.2
GT-1	31.8	28.9	27.0	25.3	24.0
	3.	3.	3.	3.	3.
	-0.0	-2.2	-0.9	-2.0	-1.1
	+0.0	+2.3	+0.6	+1.6	+1.0
GT-2	31.6	28.2	27.4	25.6	24.7
	6.	4.	3.	4.	3.
	-2.3	-0.4	-1.0	-0.7	-1.5
	+2.2	+0.4	+0.9	+0.9	+1.4
GT-3	32.3	27.9	26.9	24.9	24.1
	3.	4.	4.	4.	3.
	-0.0	-0.7	-1.5	-2.2	-1.0
	+0.0	+0.7	+1.1	+1.4	+0.7



TABLE 10  
MECHANICAL PROPERTIES OF IN100 AT 1350°F  
Nominal Diameter at 70°F - 0.250 in.

Specimen ID	Strain Rate Beyond Yielding in./in. min.	Gage Length 70°F (in.)	Thermal Expansion (in.)	Yield Strength at 0.2% O.S. (ksi)	Ultimate Strength (ksi)	True Fracture Stress (ksi)	Elongation of Gage Length (%)	Reduction of Area (%)
ENTEN-1	0.0033	1.000	0.012	141.5	143.6	130.	7.0	8.6
ENTEN-4	0.0004	1.000	0.0093	119.1	121.8	108.	3.5	7.1
GT-1	0.085	1.000	ND	153	163	149	18.9	21.
GT-2	0.0038	0.998	0.009	136	143	134	5.1	8.1
GT-3	0.0001	1.000	0.009	115	118	78	8.8	7.9

AD-A113 841

SYSTEMS RESEARCH LABS INC DAYTON OH RESEARCH APPLICA--ETC F/G 11/4  
MECHANICAL PROPERTY CHARACTERIZATION AND MODELING OF STRUCTURAL--ETC(U)  
FEB 82 N E ASHBAUGH, H L BERNSTEIN F33615-79-C-5025  
SRL-9799 AFWAL-TR-81-4187 NL

UNCLASSIFIED

2 of 2

AD-A113 841

2 of 2

2 of 2

END

DATE

FILED

5-82

DTIC

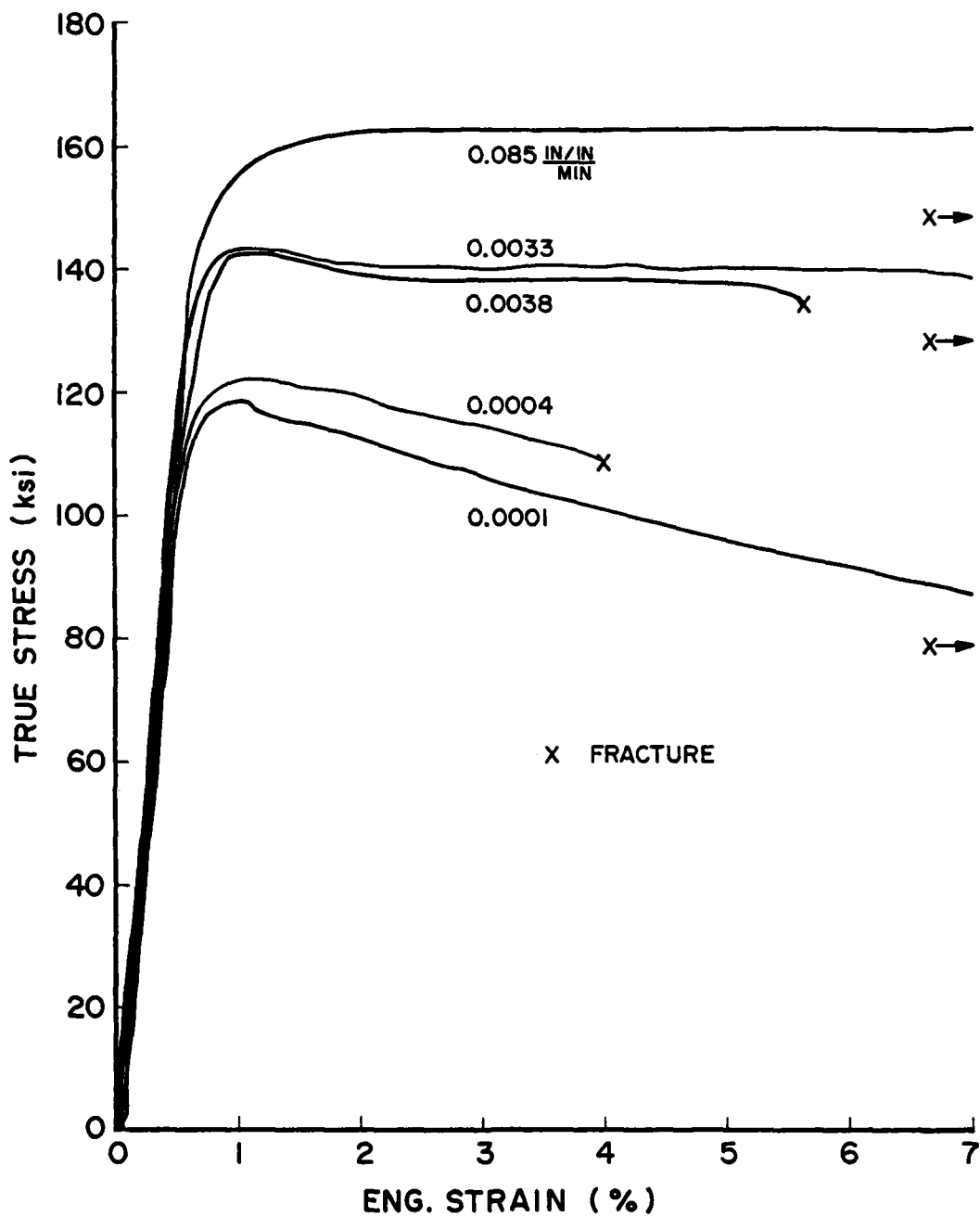


Figure 31. Tensile Tests of IN100 at 1350°F and at Various Strain Rates.

#### SECTION IV

##### DEVELOPMENT OF TESTING TECHNIQUES, EQUIPMENT, AND INSTRUMENTATION

The AFWAL/Materials Laboratory Mechanical Test Facility was maintained, operated, and upgraded in order to provide efficient state-of-the-art performance. Advanced testing techniques were developed to investigate crack-growth behavior, fatigue, and fracture. Specific improvements which were made include crack-length determination by COD measurements, development of electric-potential methods and compliance techniques, creep-facility updating, incorporation of the computer control system, and expansion of the computer signal-generator system including interactive capabilities, design of an environmental chamber, and design and fabrication of versatile resistive furnaces. Routine maintenance, calibration, and repairs as well as necessary modifications of existing equipment were carried out.

#### 1. AUTOMATION OF CREEP FRAME FOR SUSTAINED-CRACK-GROWTH TESTS

For automating compliance measurements in the creep frames, a variable-speed motor was mounted on Swedish Frame 4 to balance or unbalance the loading beam. This motor kept the beam in balance during the test, compensating for deflections in the specimen. It also was used to unbalance the beam and then rebalance the beam periodically during the test to provide a partial unloading and reloading of the specimen as required for compliance determination. A tensile load cell was designed and made of 7075-T6 aluminum alloy to cover the load range of 500 to 3,000 lb (0.238 in. D). This was one load cell of a series of four, covering the load range of 100 to 12,000 lb with high sensitivity. The load cell was located in the load train below the specimen.

A partial evaluation of the compliance automating system in the Swedish creep frame was made. Table 11 summarizes the results. In addition the data-sampling and compliance computer programs being used on the MTS #6 crack-growth effort were used to calculate compliance. Direct

TABLE 11

COMPLIANCE DATA FOR COMPACT-TENSION SPECIMEN 7-5, IN100

a = 0.500 in., B = 0.202 in., LOADED TO 2000 lb.

Compliance, micro-inches/lb.

Punched Paper Tape Plot 200-lb. load Increments		From X-Y Recorder Plot 200-lb. load Increments		X-Y Recorder Trace Continuous Motor Driven Loading	
<u>Load</u>	<u>Unload</u>	<u>Load</u>	<u>Unload</u>	<u>Load</u>	<u>Unload</u>
FIRST SETUP					
2.02*	2.09*	1.99*	2.01*	2.04*	1.97*
				1.98*	1.96*
				1.93	1.94
SECOND SETUP					
2.03*	2.06	2.02*	2.06	2.03	2.02
2.00	1.95	1.96	1.99	2.03	2.01
1.94	2.06	1.94	2.04	2.00	2.00
1.94	2.04*	1.94	2.06*	2.03*	2.00*
		2.06*		1.98	1.99
					2.00*
AVERAGE					
1.99	2.04	1.97	2.04	2.00	1.99

\* Compliance determined from load-deflection data taken from 0 to 2000 lb. Other compliance values obtained from data taken from 1000 to 2000 lb.

input of deflection and load signals was made to the computer program, and program variables were examined. A good series of calculations was found using the calculating range of 1100 to 1900 lb and about 130 data points. Successive compliance values found were: 2.085, 2.087, 2.086, 2.083, 2.090, and  $2.085 \times 10^{-6}$  in./lb. An analytical result of  $2.22 \times 10^{-6}$  in./lb was obtained using a boundary integral technique.<sup>44</sup>

The compliance automating system in the Swedish creep frame was modified by the addition of an electrical circuit consisting of three microswitches and a micrometer adjustment. With this system a final crack length was selected and converted into a deflection change from compliance relations and the test stopped through unloading of the specimen. One microswitch was activated by movement of the loading arm of the frame. The amount of movement of the loading arm required to flip the switch can be adjusted by means of a micrometer. When this switch was activated, the load-unload motor started operating in the unload direction. This continued until the full load was carried by the floor and not by the specimen. The second microswitch was mounted in line with the specimen and stopped the motor after the specimen was unloaded. The third switch was in series with the second switch and was set as a limit to motor operation in the loading direction. One test was completed with this group of controls. Specimen 8-4B was tested at 1200°F and an initial K of  $18 \text{ ksi}\sqrt{\text{in.}}$ . At 4 p.m. the surface crack lengths were 110 and 121 mils. The system was adjusted for final surface crack lengths of 150 mils. The following morning the specimen had been unloaded and the surface crack lengths were 155 and 157 mils.

## 2. SOFTWARE DEVELOPMENT FOR COMPUTER DATA ACQUISITION, AUTOMATED CONTROL OF CRACK-GROWTH TESTS, AND DATA REDUCTION.

The programs which are described in this subsection have been delivered to AFWAL/MLLN.

a. Data Acquisition to Determine Compliance and Crack Length

A program was written for the US Data Signal Generator System to acquire load and displacement data and then to conduct a linear-regression analysis on a selected portion of the data. Compliance was determined from the inverse of the slope of a linear-regression analysis of load-versus-displacement data. Then crack length was computed from a functional expression<sup>40</sup> of crack length versus compliance for the geometry being tested.

Due to the small displacements for short crack lengths in the particular test being conducted, the ratio of the maximum displacement signal-to-noise level was about 20. To produce a higher signal-to-noise ratio, a low band-pass filter was used since the displacement was obtained from the most sensitive range of the extensometer and the noise level was within specs for the system. However, a phase shift was produced in the displacement signal relative to the load signal; therefore, a second channel of the filter was applied to the load signal which brought the two signals back in phase.

In the program data used for the compliance determination could be selected from the loading or unloading portion or both portions of the acquired load-displacement data. Also, the range and mean values of the data could be chosen in such a way that portions of the acquired data at maximum and minimum load where nonlinearities in the displacement data occurred could be avoided in the compliance computation.

For evaluation the system was set to sample data every 0.01 sec and to acquire 187 load and displacement data points. Since the operating frequency of the test is 2.5 Hz, data were acquired from 4.7 loading cycles. An extensometer used to measure COD in elevated-temperature tests was attached to a CT specimen with 0.5-in. thickness and 2.50-in. total width. The tests were conducted at room temperature.

Table 12 contains the mean crack length and standard deviation based upon 10 acquired data samples. Data for the crack-length calculations were taken from the unloading and loading portions of the acquired data. The window for the data which were used in the computation was the mean load  $\pm$  25% of the load range. The load excitation was a ramp waveform. When the window was applied to the 4.7 loading cycles,  $\approx$  40 data points were used in the crack-length calculation; when the window was applied to 1 cycle, only  $\approx$  10 data points were used in the calculation.

In Table 12 the crack lengths were determined from the basic (unfiltered) signals, the filtered signals, and the filtered signals with a 10 $\times$  amplification of the displacement signal. The shift in the mean crack length between the unfiltered and filtered signals was attributed to dynamic effects of the loading frame and specimen caused by a ramp waveform. One very encouraging result for the reproducibility of the system was that two data sets had less than 0.001-in. standard deviation. This compliance program and the program for spectrum-load testing<sup>45</sup> which was developed under a previous contract constitute the principal parts of the following program for automated control of a test frame.

b. Automated Computer Control of a Test System

A program was developed to enable the M400 Computer Control System on MTS #6 to monitor the specimen response and, in turn, enable the test parameters to be controlled automatically. The computer system consists of a Tektronix 4051 and a U.S. Data Engineering Signal Control Unit (SCU) which, in addition to generating a command signal, has the capability of acquiring data. The software was written in such a way that crack growth would be produced under a constant  $\Delta K$  condition.

In the software, the crack length of a specimen is determined from compliance which was obtained from acquired data on the load and the COD. The compliance was calculated by linear regression to a portion of the load-displacement data. The portion of the load-displacement data used in



TABLE 12  
MEAN AND STANDARD DEVIATION OF CRACK LENGTH  
DETERMINED FROM LOAD-COD DATA

	$\bar{a}$ (in.)			
	$\sigma$ (in.)			
	Data for Compliance			
	Unloading		Loading	
Signal Condition	40 data points	$\approx$ 10 data points	$\approx$ 40 data points	$\approx$ 11 data points
Basic Signal	0.99354	--	--	--
	0.01417	--	--	--
Filtered	0.96879	0.97327	--	0.97519
	0.00274	0.00958		0.00450
Filtered with	0.96146	0.96356	0.96873	
10 $\times$ Amplification	0.00096	0.00439	0.00066	--

the compliance determination was preselected by the operator when the program was set up. From the crack length, load parameters, and  $\Delta K$ , a new load is calculated and compared with the current load. If the percentage change in load exceeds an amount which was preselected by the operator, the new maximum load is produced in the command signal.

The block diagram in Fig. 32 indicates the major steps in the software when the program is set up. The program handled either a CT ( $H/W = 0.6$ ) or a WOL ( $H/W = 0.486$ ) specimen geometry. The load parameters consisted of the maximum load, frequency, and R ratio. For proper data acquisition, data were acquired over at least one complete loading cycle. The calibration factors coupled the computer system with the test-frame hardware. The window determined the data points in the acquired data which were used in the compliance computation. Normally, the upper portion of the loading curve was chosen in order to avoid closure effects. Data around the peak load were also avoided because of potential perturbations created by the change in load direction.

The block diagram in Fig. 33 indicates the major steps in the feedback loop. When the program was initialized and the specimen located in the test frame, the operator began the program. The program acquired data and computed a compliance and a crack length from the relationship in Ref. 40 and then a new load. However, the maximum load on the specimen was not changed until the operator was satisfied that all segments of the test were operating properly. Then the operator would set a flag in the program so that the feedback loop for the load was completed, and the test would be under computer control.

Since no real-time clock was available with the computer system, the crack-length determination was initiated after a buffer refill for the command signal (end-points) had been requested. Thus, the new maximum load would be applied to the specimen after the next buffer-refill request. The minimum time between buffer refill requests was limited by computer-system hardware for handling the acquired data. The range of time between buffer refills was ~ 4-60 min.

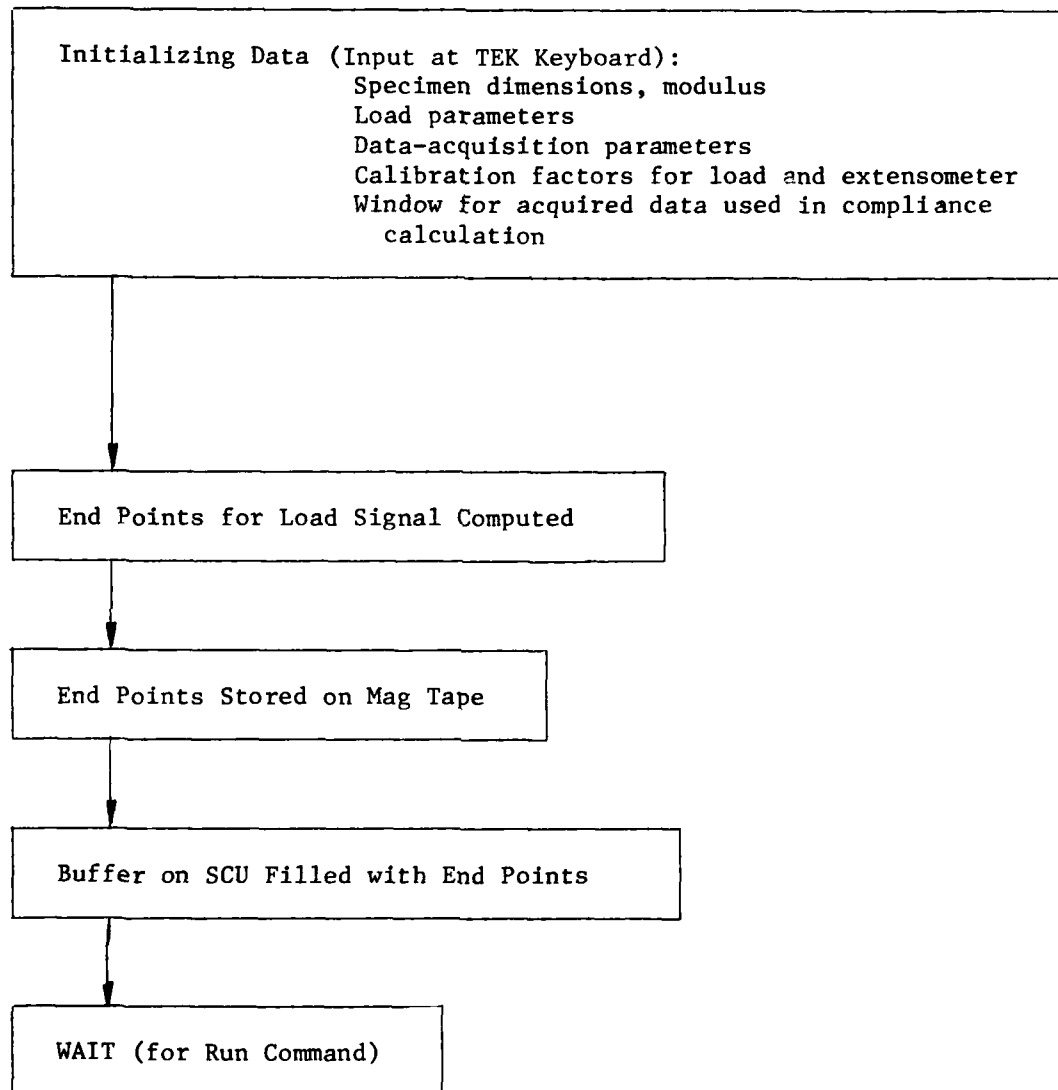


Figure 32. Block Diagram of Major Steps in Initializing Control Program.

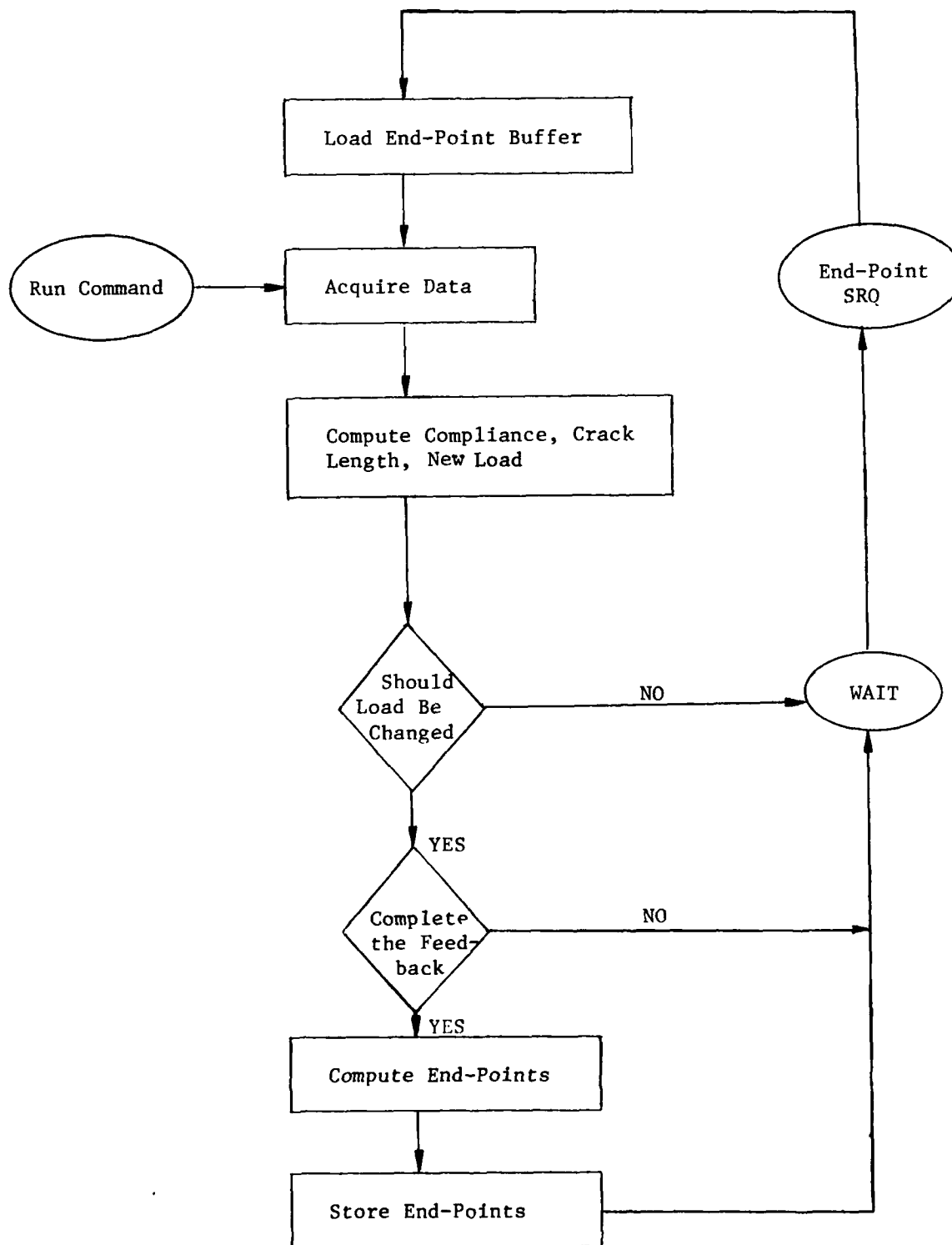


Figure 33. Block Diagram of Major Steps in Feedback Loop of Control Program.

The software could be set up to provide several modes of operation. The operator could control the  $\Delta K$  on the specimen through the computer in an open-loop mode. In this mode the  $\Delta K$  level would be changed without stopping the test. Rather than one set of data being acquired for a crack-length determination, several sets could be acquired if the time between buffer refills were sufficiently long. Several sets of data would provide a better estimate of the crack length.

In order to evaluate the operation of the control program and the response of the overall system, a trial specimen made from steel was tested. Steel was chosen because its modulus has a value similar to IN100 which will be the primary material tested in the system in the near future. A plate of deck steel was available of sufficient thickness (0.30-in.) that the steel specimen would be the same size as the IN100 specimens. Thus, the elastic displacements which were measured by the COD extensometer would be similar to those for the IN100 specimens.

However, the steel was more ductile than the IN100, and the test--even though successful--was terminated prematurely by the control program due to excessive plastic deformation which exceeded the limits of the extensometer. In order to obtain reasonable crack growth in the time available, the test was conducted at a stress-intensity value of  $45 \text{ ksi}\sqrt{\text{in.}}$  with  $R = 0.1$ . These loading conditions produced hysteresis in the load-vs.-COD curves. As the crack grew, the COD ratchetted further open until the range of the extensometer was exceeded and the test was automatically terminated.

During the test, optical measurements were made of the crack length on the surface of the specimen. A comparison of the results of the optical measurements and compliance data is made in Table 13. The compliance crack lengths were larger than the surface crack lengths, primarily due to crack-front curvature and the previously discussed inelastic deformation. The curvature of the center of the crack front was  $\approx 50$  mil ahead of the tips on the surface of the specimen when the test was terminated.

TABLE 13

OPTICAL AND COMPLIANCE CRACK LENGTHS FOR  
TRIAL SPECIMEN TESTED UNDER COMPUTER CONTROL

Cycles (kcycle)	Crack Lengths <sup>(a)</sup> (in.)	
	Optical Measurement	Compliance <sup>(b)</sup> Analysis
0	0.553	0.553
0.5	0.559	0.581
1.25	0.569	0.601
1.69	0.580	0.613
2.99	0.611	0.644
4.10	0.647	0.665
5.38	0.671	0.724
6.7	-	0.755 <sup>(c)</sup>
6.8	0.713	-

(a) Notch length = 0.245 in.; width, W = 1.6 in.

(b) To obtain crack length, modulus used was 29 Mpsi for 0-2.99 keyc data, 28 Mpsi for remainder of test.

(c) Last valid compliance result.

The inelastic deformation also had a significant effect upon the compliance because the window was set to accept the load-displacement data for compliance upon increasing<sup>\*</sup> load. Unfortunately, this region on the load-displacement curve is the most sensitive to inelastic deformation. The use of the compliance on the unloading side of the load-displacement curve would have provided much better agreement with the surface crack length and crack-front curvature.

For this test, 1% was chosen as the absolute percentage change in load level which would be required before the new maximum load would be applied to the specimen. It was thought that there would be excessive scatter in the data and/or the response of the system which would cause the load to increase at times during the test. However, this was not the case. The load either decreased or remained the same after each data sample. Since control was possible at a 1% load variation, the system was able to detect less than a 1.5% change in compliance. For this particular range of crack lengths, the change in compliance corresponded to the detection of crack-length changes of about 0.5% or 3 mils.

#### c. Modifications to the Automatic Computer-Control Program

The automated computer-control test program was modified to permit another type of crack-growth test to be automatically conducted in the Facility on MTS #6. The previous program provided automatic control of an FCG test under constant  $\Delta K$  conditions. Due in part to the limitations of the system, tests could only be conducted at low frequencies of  $\leq 0.5$  Hz.

Several modifications were made to this program which expanded the automated test capabilities. One of the new programs basically controls the load as a function of crack length. In the program the load would be incremented or decremented each time the crack grows a preselected increment. After the crack has grown to a prescribed length, the load would remain constant.

---

\* The only reason for the software being written to select the data from the positive loading rate was that the response of the test frame was smoother upon loading than unloading. Incorporation of data for compliance calculation upon unloading would require a very minor change in the software.

This program was used to collect FCG data and has the potential to control threshold tests. The program allows test frequencies of up to  $\approx 2.5$  Hz.

The basic constant-AK program was also modified in such a way that the accumulated data on cycle count, crack length, load level, etc., were written on magnetic tape. This modification allowed for a longer continuous test time. The basic program stored data in the computer memory which provided easier access to the data than possible with tape but severely limited the amount of data which could be stored before the computer memory would overflow.

d. Monitoring and Control System

A program was written for the U. S. Data Monitoring and Control System to permit various types of data to be collected automatically and stored for future use. The system consisted of a U.S. Data Interface Unit (IU), a Tektronix 4051, a Tektronix 4907 File Manager, five cycle counters, and a multiplexed hard-copy unit. The IU accepts the input of 16 differential analog voltage signals, 20 channels of 3 1/2-digit BCD data (plus a sign bit, a data-valid bit, and a range bit), and 80 channels of logic-level digital data. The IU also has 16 logic-level output channels. The system was connected to five MTS frames, each frame being allocated three analog, four BCD, and sixteen logic-level input channels and three logic-level output channels. The data from the input channels were collected in the IU, transferred to the TEK 4050, and then stored in the file manager.

In addition to the software development, extensive wiring between the IU and the test frames was installed. The signals in the test frames were modified for compatibility with the inputs of the IU.



Although it appeared that the program was functioning properly, problems existed in the system hardware. Cross-talk between analog channels from different machines occurred. The cross-talk did not influence machine control but did adversely affect the readout devices in use. Another major problem involved reading of the time from the IU memory and caused the TEK to stop in the I/O mode. Subsequently, this problem was traced to a faulty GPID card in the IU.

e. Crack-Growth Data Reduction

Four computer programs to facilitate the reduction of crack-growth data were completed. The programs are run on the ASD CDC computer system. The programs accept various types of raw crack-length data or those from COD or compliance measurements. Also, two of the programs accept data which were obtained under variable-load conditions. The crack-growth rate is determined for either cyclic- or time-based data with appropriate headings on the computer print-out. A plot of crack length versus cycle count or time is made. The crack-growth rate can be obtained by either the incremental polynomial method or the secant method. Both methods are recommended in the ASTM E 647-78T Test Method. For the incremental polynomial method, a least-squares error fit to, at most, 21 data points can be selected. The programs will determine the stress-intensity range for six types of test specimens: CT, single edge notch, three point bend, WOL, center crack, and tension ring.

A summary of the different aspects of the four programs is given in Table 14. The generally accepted test for obtaining crack-growth-rate data is conducted under constant load. However, some important tests such as a threshold test must be carried out with variable loads. Thus, two basic input data sets exist: 1) crack length and cycle count or time and 2) crack length, load, and cycle count or time. Since data in the literature must now be presented in SI units, an additional set of programs was written to convert the laboratory raw data which is being obtained in English units into reduced data in SI units.

TABLE 14  
COMPUTER DATA-REDUCTION PROGRAMS

PROGRAM ID	COMPUTER SYSTEM	INPUT VARIABLES <sup>(a)</sup>	INPUT UNITS <sup>(a)</sup>	OUTPUT UNITS
NAK	ASD/CDC	a,N	English	English <sup>(b)</sup>
NEA	ASD/CDC	a,P,N	English	English <sup>(b)</sup>
MAK	ASD/CDC	a,N	English	SI <sup>(c)</sup>
MPA	ASD/CDC	a,P,N	English	SI <sup>(c)</sup>
TEK	TEK 4051	a,N	English	English <sup>(d)</sup>

- a) Input variables are a-crack length (units in in.), P-load (lb) and N-cycle count or time (variable input units). For the TEK program N is cycle count.
- b) English units for crack-growth rate and stress-intensity range are in./cycle or min. and ksi-in.<sup>1/2</sup>, respectively.
- c) SI units for crack-growth rate and stress-intensity range are m/cycle or s and MPa·m<sup>1/2</sup>, respectively.
- d) For the TEK program the crack-growth rate is in in./cycle.

Since several TEK 4051 desk-top computers are available in the laboratory, a shortened version of the previously described data-reduction programs has been written in BASIC language for this computer. In Table 14, this program is referred to as TEK. Input crack-length and cycle-count data were read from magnetic tape which had been produced from the data-acquisition or control programs discussed previously. The crack-length and cycle-count data can be curve fit to obtain  $da/dN$  values by either the secant method or the incremental polynomial method using 3 - 21 data points. The stress-intensity range can be computed for only two specimens--WOL and CT. An example of a plot and listing of the input data given by the program are shown in Fig. 34 and Table 15, respectively. The reduced data obtained by a nine-point incremental polynomial method for a WOL specimen are shown in Fig. 35 and listed in Table 16. An example of the data reduced by the secant method is given in Fig. 36 and Table 17.

### 3. IMPROVED LABORATORY EQUIPMENT AND TEST PROCEDURES

#### a. Centorr Vacuum System

The Centorr vacuum system was disassembled and cleaned; new O-rings were purchased and the system reassembled. Because of the age of this equipment, many of the O-rings were no longer standard, and some difficulty was experienced in obtaining them.

Since the electrical control system had been modified many times in the past, no up-to-date documentation was available on its operation. Procedures for the operation were pieced together from previous reports and determined from hands-on operation.

The system was assembled in MTS 5 in preparation for the proposed investigation of environmental effects upon nickel-base superalloys.

The Riehle-vacuum-furnace extensometer was evaluated for use with the Centorr vacuum system. Using the Instron X-Y chart drive system and a sensitivity of 1 mil/in. of chart, the signal varied near  $\pm 0.5$  mil over

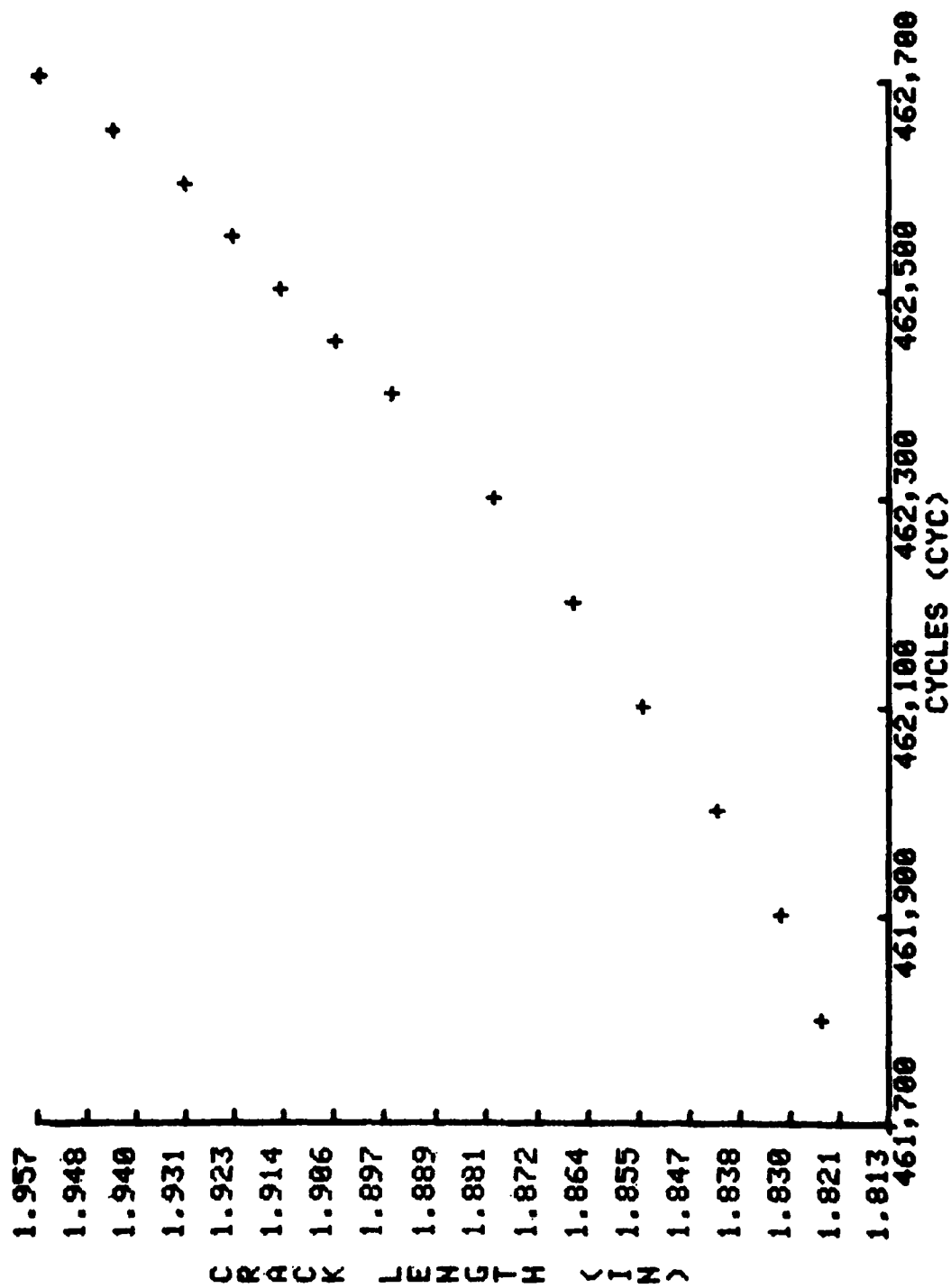


Figure 34. Plot of Crack-Length Versus Cycle-Count Data Listed in Table 15.

TABLE 15

## INPUT CRACK-GROWTH DATA

SPECIMEN TYPE	WOL	SPECIMEN THICKNESS	B=0.2182 INCHES	SPECIMEN WIDTH	W=2.548 INCHES	NOTCH CRACK LENGTH=0.6216 INCHES	CYCLES (CYC)	CK	LTH(IN)	IN A1(IN)	IN A2(IN)	MAX P(LBS)	PHIN/PNAX
+461,700	+1.813	+1.191	+1.191	+370.00	+0.100								
+461,800	+1.825	+1.203	+1.203	+370.00	+0.100								
+461,900	+1.832	+1.210	+1.210	+370.00	+0.100								
+462,000	+1.842	+1.221	+1.221	+370.00	+0.100								
+462,100	+1.855	+1.233	+1.233	+370.00	+0.100								
+462,200	+1.866	+1.245	+1.245	+370.00	+0.100								
+462,300	+1.880	+1.258	+1.258	+370.00	+0.100								
+462,400	+1.897	+1.275	+1.275	+370.00	+0.100								
+462,450	+1.906	+1.285	+1.285	+370.00	+0.100								
+462,500	+1.915	+1.294	+1.294	+370.00	+0.100								
+462,550	+1.924	+1.302	+1.302	+370.00	+0.100								
+462,600	+1.932	+1.310	+1.310	+370.00	+0.100								
+462,650	+1.944	+1.323	+1.323	+370.00	+0.100								
+462,700	+1.957	+1.335	+1.335	+370.00	+0.100								

STOP IN LINE 2234 PRIOR TO LINE 2236

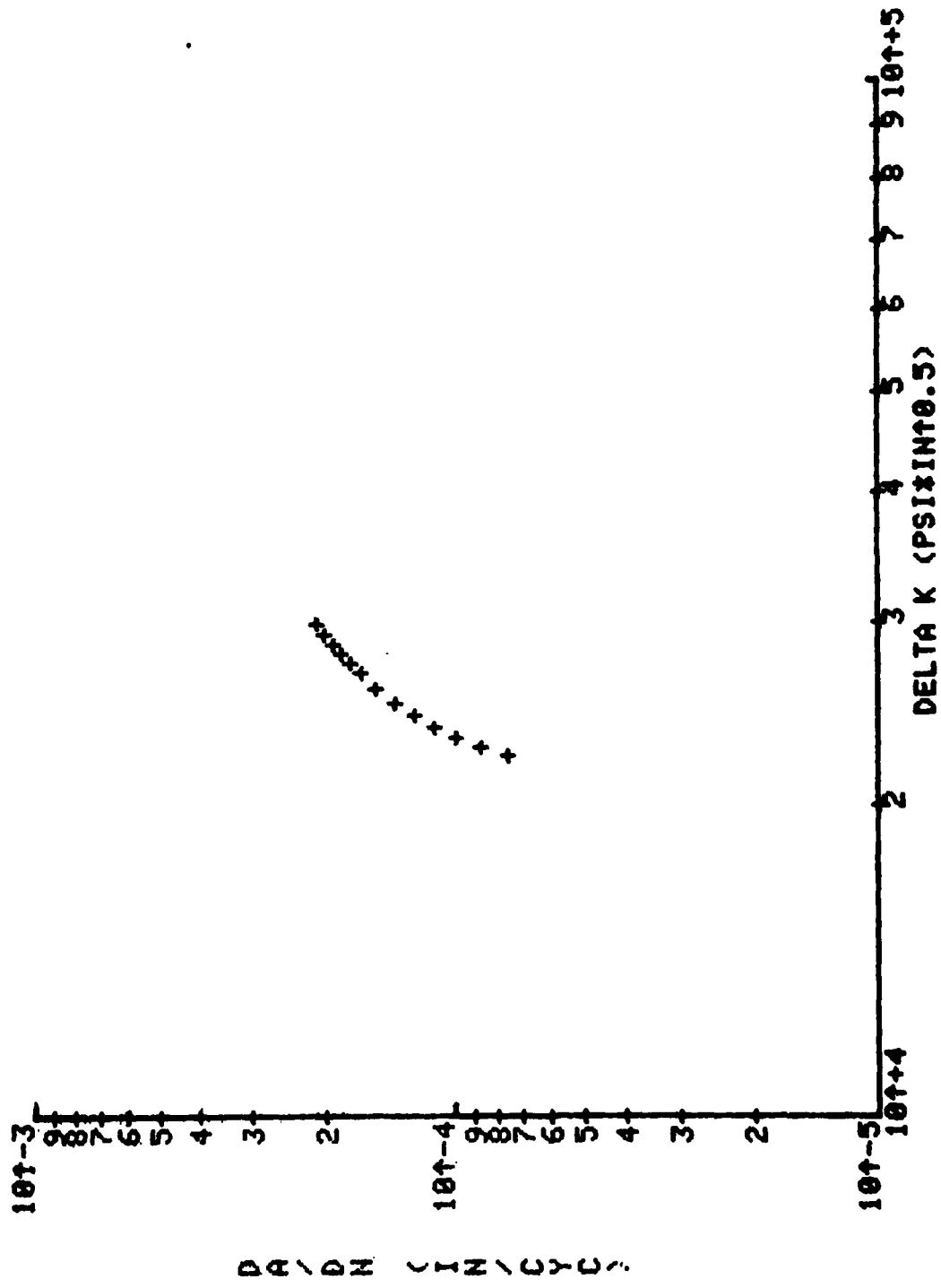


Figure 35. Plot of  $da/dN$  versus  $\Delta K$  for a Nine-Point Least-Squares Fit of Data in Table 15.

TABLE 16

CGR DATA REDUCED USING NINE-POINT LEAST-SQUARES FIT

'Delta K' and 'DA/DN' for type WOL  
LSF Quadratic Polynomial Method of Data Reduction  
9 fit data points

13 Points of Reduced Data		DELTA K(Psi*IN <sup>1.5</sup> )	DA/DN (IN/CYC)
CRACK LENGTH (IN)	CYCLES (CYC)		
+1.814	+461,700	+22,318	+7.514E-005
+1.822	+461,800	+22,707	+8.738E-005
+1.832	+461,900	+23,167	+9.962E-005
+1.842	+462,000	+23,702	+1.119E-004
+1.854	+462,100	+24,320	+1.241E-004
+1.866	+462,200	+24,987	+1.376E-004
+1.881	+462,300	+25,818	+1.527E-004
+1.897	+462,400	+26,755	+1.654E-004
+1.905	+462,450	+27,264	+1.756E-004
+1.914	+462,500	+27,829	+1.843E-004
+1.924	+462,550	+28,437	+1.929E-004
+1.934	+462,600	+29,090	+2.016E-004
+1.944	+462,650	+29,793	+2.103E-004

WOL 0.25=&lt;(A/W)&lt;=0.75

STOP IN LINE 7305 PRIOR TO LINE 7310

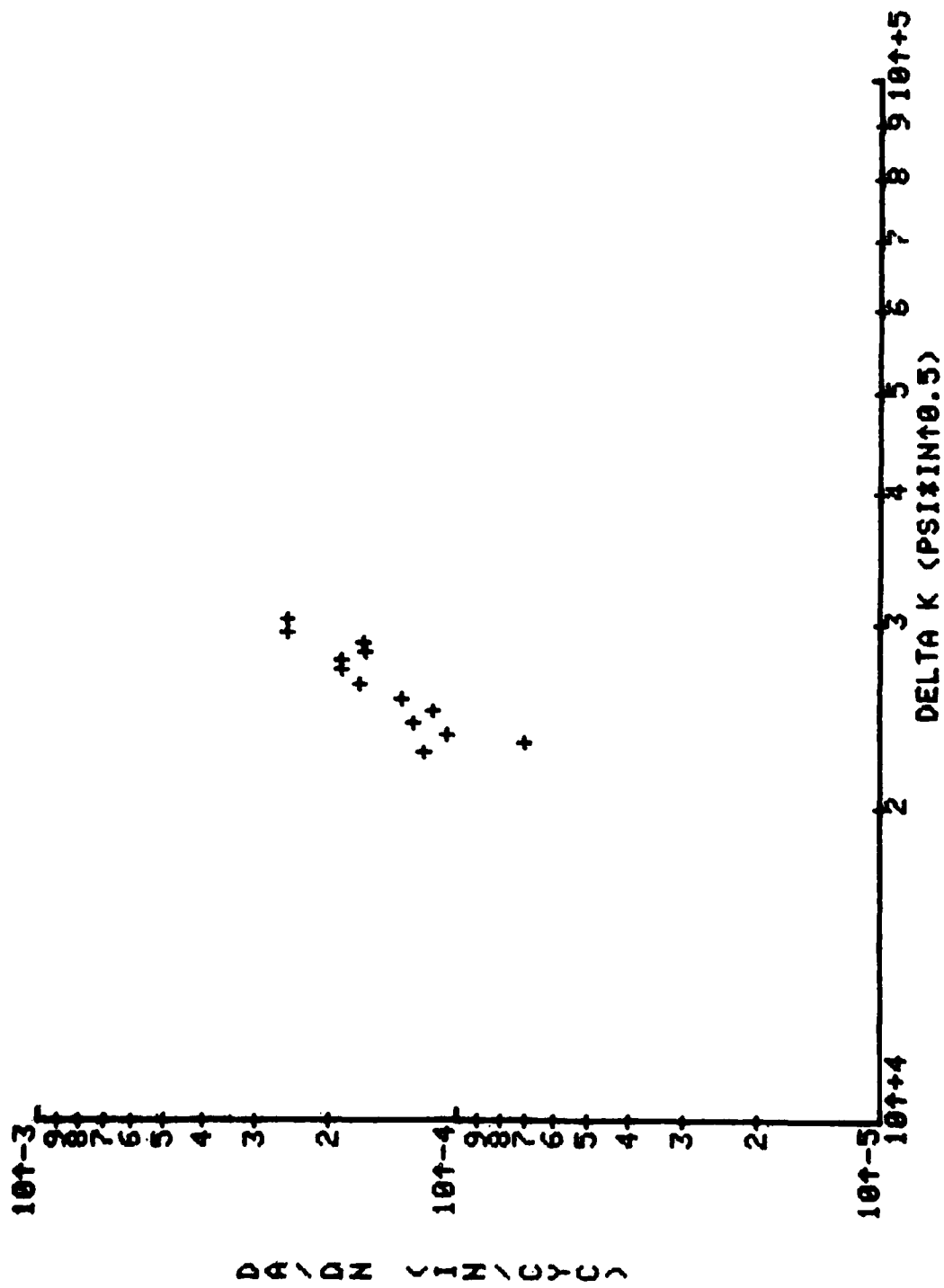


Figure 36. Plot of  $da/dN$  versus  $\Delta K$  for Secant Method of Data Reduction in Table 15.



CGR DATA REDUCED USING SECANT METHOD

## 'Delta K' and 'DA/DN' for type HOL Secant Method of Data Reduction

13 Points of Reduced Data CRACK LENGTH (IN) CYCLES (CYC)	DELTA K (PSI*IN <sup>1.5</sup> ) DA/DN (IN/CYC)
+1.819	+22,526
+1.828	+22,988
+1.837	+23,428
+1.849	+24,028
+1.861	+24,671
+1.873	+25,360
+1.888	+26,240
+1.901	+27,030
+1.911	+27,608
+1.920	+28,165
+1.928	+28,704
+1.938	+29,402
+1.951	+30,269
	+1.200E-004
	+7.000E-005
	+1.060E-004
	+1.270E-004
	+1.140E-004
	+1.350E-004
	+1.700E-004
	+1.860E-004
	+1.860E-004
	+1.640E-004
	+1.660E-004
	+2.500E-004
	+2.500E-004

**WOL 0.25= $\langle A/W \rangle \leq 0.75$**

STOP IN LINE 7305 PRIOR TO LINE 7310

a period of 65 hr. Changes in deflection took the form of steps because of the gear system used. With the Use of Automatic Timing and Controls Type 6101E-2-X LVDT electronics having a sensitivity of 1 mil/in. of chart, the stability was about  $\pm 0.7$  mil in 70 hr. In both cases, the cited results were the best attained.

b. Evaluation of Schenck Machine and Development of Instrumentation for Threshold Tests

The 300-kg Schenck constant-amplitude fatigue machine was examined for potential use in the ASTM E24.04.03 Round-Robin Low-Delta-K Fatigue-Crack-Growth Program. Electrical-resistance gages were attached to the load cell, and two separate four-active-arm bridges were formed using two SRL blue-box channels. The outputs were added in a third channel. Using this arrangement a sensitivity of 50 mV/lb was possible. When the dynamic-load signal was displayed on the scope, the noise present made it marginally possible to detect the 2-lb increments required by the program. A 1/4-in.-thick CT specimen of aluminum alloy was tested to assess the feasibility of the method. This indicated that meeting the program tolerance would be very difficult. In an attempt to overcome one of the problems, a stiff load cell was designed which could reduce the load on the specimen as the crack grew at such a rate that  $K_{max}$  and  $R$  would remain relatively constant for one setting of the machine. The stiff-load cell was made and calibrated. It yielded a linear response up to 80 lb and a sensitivity of 50 mV/lb.

The stiff-load cell was evaluated using a 0.25-in.-thick compact-tension specimen made of aluminum alloy. It was found that the load did not drop significantly with crack growth, indicating that other deflections in the loading system were playing a predominant role in determining load.

As a result it was determined that MTS 2 should be used in the program. A similar evaluation was made in MTS 2 with its 5000-lb. load cell and the 0.25-in.-thick Al specimen. The only apparent deficiency in the

MTS system was its inability to resolve the load easily to within  $\pm 2$  lb., as required by the program. A 1000-lb. load cell was ordered so that proper control of the threshold test could be achieved.

c. Electric-Potential Technique

An investigation of the electric-potential technique for measuring crack length was conducted. The specimen was a flat plate (3 1/2 in.  $\times$  2 in.  $\times$  3/32 in.) of aluminum with electrical leads attached as shown in Fig. 37. The current and potential leads were attached to the plate with screws in 0.070-in. tapped holes. The starter hole for the crack was 0.070 in., and the crack was simulated by a saw cut of  $\sim 5$  mils width. Potential measurements were made for several crack lengths which were produced without removing the leads to the plate. The circuit used for measuring potential is shown in Fig. 38. The calibration curve resulting from these measurements is shown in Fig. 39.

The variability in the potential measurement for the 1.6-in. crack was assessed under the following conditions:

<u>Test Conditions</u>	<u>Potential (V)</u> <u>(<math>\times 10^{-6}</math>)</u>
Initial setup	4.505
After reassembling specimen and equipment	4.710
After removal and replacement of leads	4.710
When room temperature was 24°C	4.653
When polarity was reversed	4.624
When room temperature was 21°C	4.701
When polarity was reversed	4.706



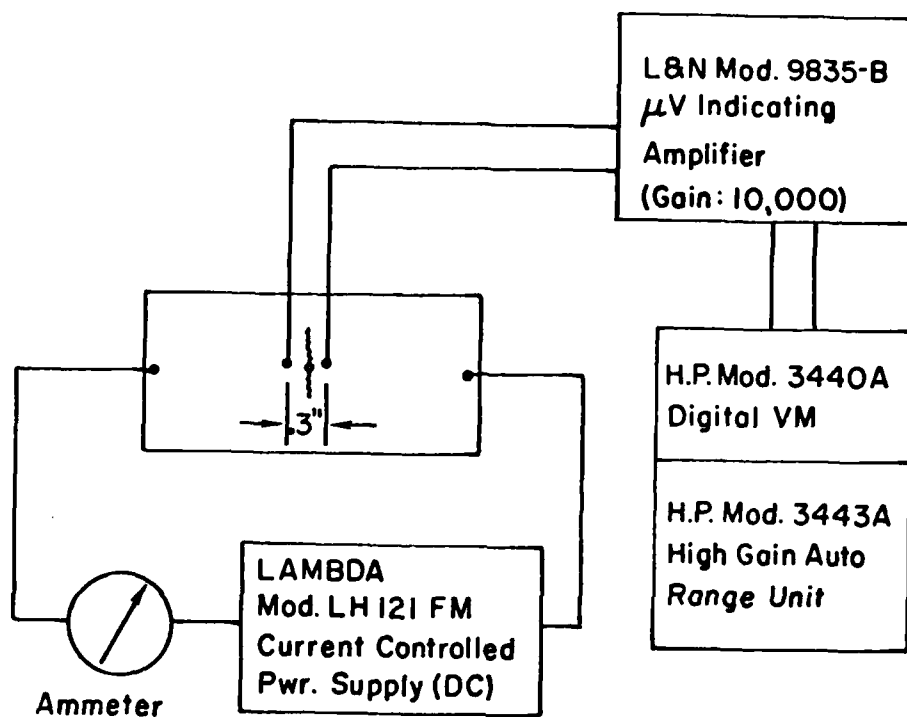


Figure 38. Circuit and Instrumentation Used for Potential Measurements.

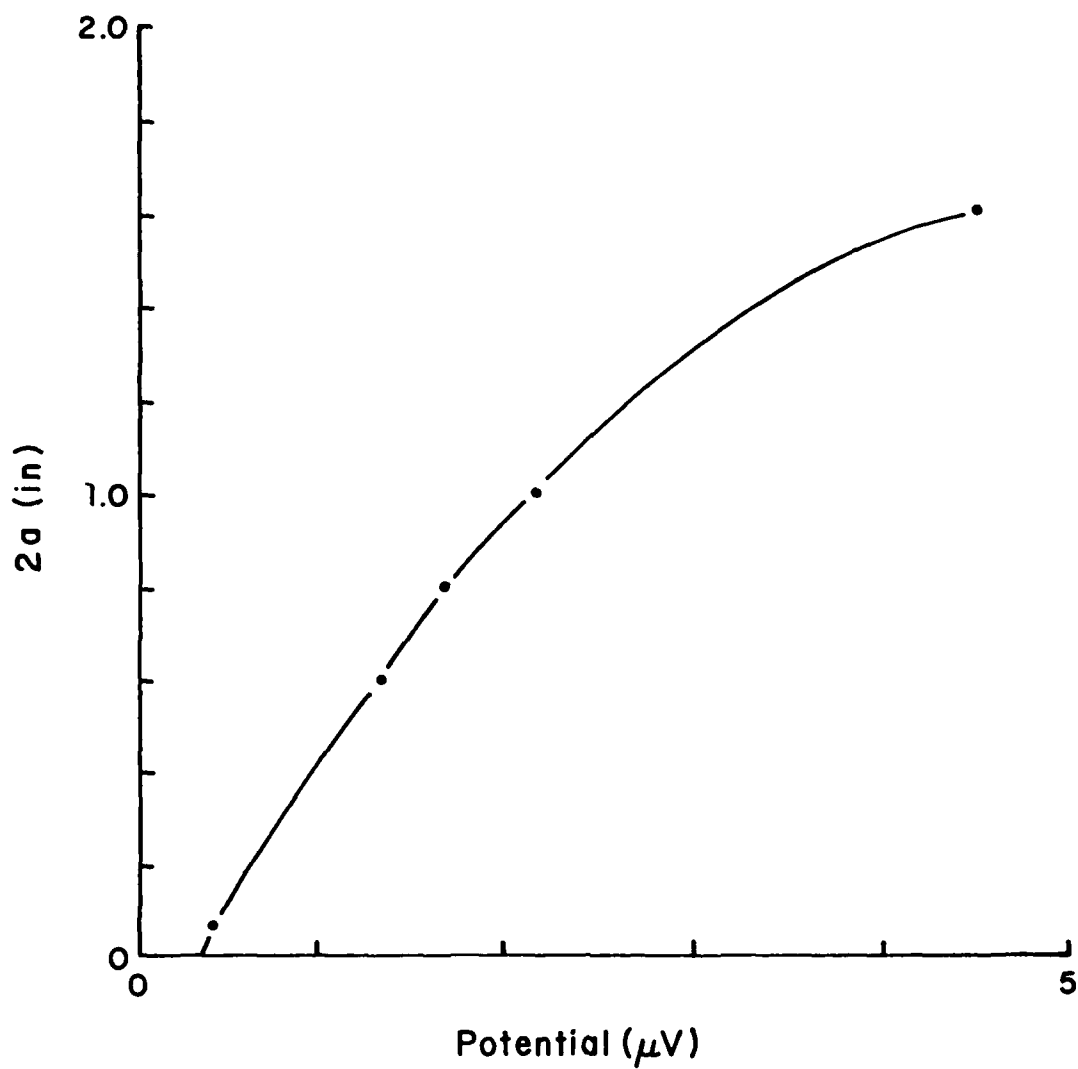


Figure 39. Calibration Curve of Total Crack Length as a Function of Electric Potential.

The variability in potential which resulted from some of the intangible factors in the system was  $0.2 \times 10^{-6}$  V which, for this crude evaluation, corresponded to 80 mils of total crack length.

These electric-potential measurements yielded the first set of consistent results that had been obtained after several AC and DC circuits were assembled to measure electric potential as a function of crack length in a representative laboratory specimen.

Bench testing of an electric-potential AC system<sup>46</sup> was done to develop an understanding of the system and to determine its operating characteristics, noise, drift, etc. The system was then installed in an MTS machine to determine what changes, if any, would occur during operation in the machine. An aluminum specimen was used in this testing, and the preliminary results indicated that no major problems existed at room temperature.

The next step was to determine the feasibility of operating at elevated temperatures using induction heating. This method of heating was chosen because of its anticipated use in an environmental chamber in the near future. The possible need for insulating the specimen from the grips and the MTS machine was investigated. Results obtained with a René 41 CT sample indicated that insulation was not required. Some rf was picked up by the electric-potential system and must be eliminated for this system to function properly.

#### d. Modulus Evaluation at Elevated Temperatures

A dial indicator was used to determine the translational motion of a tensile specimen in the MTS 6 load train during loading. When the lateral motion was minimized by rotating and manipulating the various

components in the load train, nonlinear behavior and hysteresis in the load-deflection curve were reduced and--in some cases--eliminated. Also the slope, i.e., modulus, of the curve was reproducible. The lowest lateral deflection which could be achieved was  $\approx 2$  mils.

Based upon the successful use of the dial indicator on the tensile specimen, the out-of-plane motion of a CT specimen was evaluated. Again, by minimizing the out-of-plane motion, reproducibility of compliance results could be obtained and fatigue crack growth of a specimen having unequal surface crack lengths would eventually produce surface cracks of similar lengths. However, this particular specimen eventually slid to one side in the grips, and then surface crack lengths became more unequal. Increased out-of-plane motion of the specimen also occurred after it had slipped in the grips.

e. Fatigue-Crack Extension of Tunneled Crack Formed Under Sustained Load

In extending the crack by fatigue loads in an IN100 C-specimen after testing in the creep frame at 1200 and 1350°F under sustained load, considerable difficulty was encountered. Cyclic crack growth continued in the center of the specimen (without observation) to the extent that critical conditions were reached and failure occurred. In attempts to remedy this situation, initial cyclic loads were of the magnitude used in the creep tests to encourage surface crack growth, and a clip-gage system was designed to measure compliance and, thus, approximate center crack growth. The gage consisted of beams contacting the pivot points on the E plates normally used in the creep tests. Resistance strain gages mounted to the beams provided a measure of the deflection occurring from the top to the bottom of the specimen, Fig. 40. By using compliance measurements better control was achieved in fatigue-crack growth after the sustained-load test. However, in several specimens the crack front did not straighten out and, although great care was maintained, the specimens failed during fatigue-crack growth.



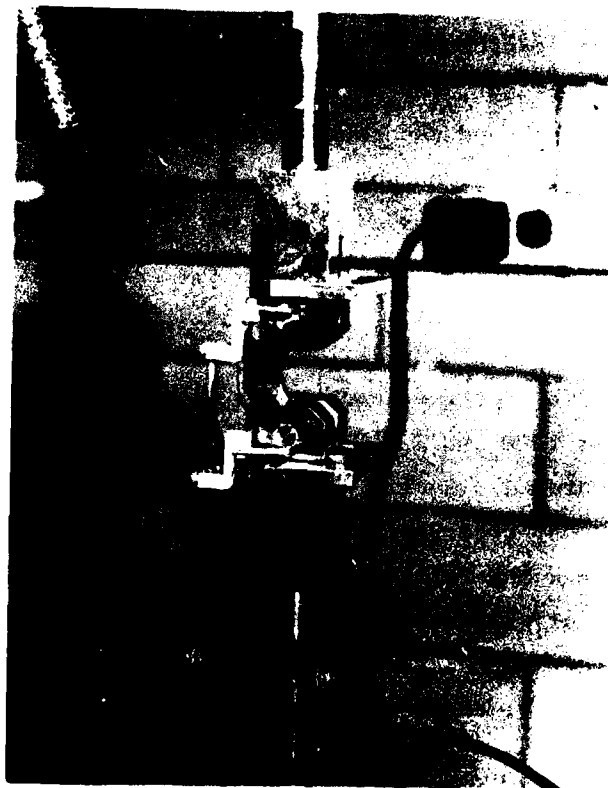


Figure 40. Measurement of Load-Line Deflection  
on C-Specimens.

f. Fabrication of Environment Chamber

One of the goals of this program was to develop a chamber for use on the MTS machines which would permit the control of environmental parameters. Several meetings were held to define the exact requirements of this chamber.

The main requirements which were considered are as follows:

- A. 1400<sup>0</sup>F "CAL-ROD" type heater
- B. 10<sup>-6</sup> Torr vacuum
- C. Gas-flow system
- D. View ports
- E. Extensometer use
- F. All internal-weld stainless-steel construction
- G. Accept CT specimen (W - 2 in.)

The main body of the chamber and the front and back doors have been fabricated and delivered to AFWAL/MLLN.

## REFERENCES

1. S. Floreen and R. H. Kane, "An Investigation of the Creep-Fatigue-Environment Interaction in a Ni-Base Superalloy," published in Fatigue of Engineering Materials 1980. Also Inco Research and Development Center Technical Paper 1020-T-OP dated August 1979.
2. K. Sadananda and P. Shahinian, "The Effect of Environment on the Creep Crack Growth Behavior of Several Structural Alloys," Materials Science and Engineering 43, 159 (1980).
3. R. M. Pelloux and J. S. Huang, "High Temperature Creep-Fatigue Crack Growth in Astroloy" Annual Technical Report on AFOSR-76-2928 dated February 1980.
4. S. Floreen and R. H. Kane, "Effects of Environment on High-Temperature Fatigue Crack Growth in a Superalloy," published in Metallurgical Transactions (1979).
5. M. N. Menon, "The Effect of Environment on the Creep and Stress Rupture Behavior of René 95," Journal of Materials Science 11, 984 (1976).
6. P. Shahinian, "Effect of Environment on Creep-Rupture Properties of Some Commercial Alloys," Transactions of the American Society for Metals 49, 862 (1957).
7. R. H. Cook and R. P. Skelton, "Environment-Dependence of the Mechanical Properties of Metals at High Temperature," International Metallurgical Reviews 19, 1741 (1975).
8. S. Floreen, "The Creep Fracture of Wrought Nickel-Base Alloys by a Fracture Mechanics Approach," Metallurgical Transactions 6A, 1741 (1975).
9. R. B. Scarlin, "Creep and Fatigue Crack Growth in Overaged Nickel-Base Alloys," Materials Science and Engineering 30, 55 (1977).
10. T. Ericson, "Review of Oxidation Effects on Cyclic Life at Elevated Temperature," unpublished paper, 1979. Dr. Ericson is at the Linköping Institute of Technology, Linköping, Sweden.
11. R. P. Wei, P. S. Pao, R. G. Hart, T. W. Weir, and G. W. Simmons, "Fracture Mechanics and Surface Chemistry Studies of Fatigue Crack Growth in an Aluminum Alloy," IFSM-79-98 (Institute of Fracture and Solid Mechanics, Lehigh University) or Technical Report No. 9, Office of Naval Research, Contract N00014-75-C-0543, NR 036-097, April 1979.
12. M. Gell and D. J. Duquette, "The Effects of Oxygen on Fatigue Fracture of Engineering Alloys," in Corrosion Fatigue, NACE-2 (National Association of Corrosion Engineers, Houston, TX, 1972), pp. 366-378.
13. G. W. Simmons, P. S. Pao, and R. P. Wei, "Fracture Mechanics and Surface Chemistry Studies of Subcritical Crack Growth in AISI 4340 Steel," Metallurgical Transactions 9A, 1147 (1978).

14. P. J. Bania and S. D. Antolovich, "Activation Energy Dependence on Stress Intesity in Stress-Corrosion Cracking and Corrosion Fatigue," Stress Corrosion-New Approaches, ASTM STP 610 (American Society for Testing and Materials, Philadelphia, PA, 1976), pp. 157-175.
15. R. Raj and S. Baik, "Creep Crack Propagation by Cavitation Near Crack Tips," Metal Science 14, 385 (1980).
16. D. A. Miller and R. Pilkington, "Diffusion and Deformation Controlled Creep Crack Growth," Metallurgical Transactions 11A, 177 (January 1980).
17. R. W. Balluffi and L. L. Seigle, "Growth of Voids in Metals During Diffusion and Creep," Acta Metallurgica 5, 449 (August 1957).
18. D. Hull and D. E. Rimmer, "The Growth of Grain-Boundary Voids Under Stress," Philosophical Magazine 4, 673 (June 1959).
19. R. Raj, H. M. Shih, and H. H. Johnson, "Correction to Intergranular Fracture at Elevated Temperature," Scripta Metallurgica 11, 839 (1977).
20. R. Raj and M. F. Ashby, "Intergranular Fracture at Elevated Temperature," Acta Metallurgica 23, 653 (June 1975).
21. J. W. Hancock, "Creep Cavitation Without a Vacancy Flux," Metal Science 10, 319 (1976).
22. F. A. McClintock and A. S. Argon, Mechanical Behavior of Materials (Addison-Wesley, Reading, MA, 1966).
23. A. Needleman and J. R. Rice, "Plastic Creep Flow Effects in the Diffusive Cavitation of Grain Boundaries," Acta Metallurgica 28, 1315 (1980).
24. K. Sadananda and P. Shahinian, "Creep-Fatigue Crack Growth," To be published in the Research Mechanics Monograph, Voids, Cavities, and Cracks in Metallic Alloys (J. H. Gittus, Ed.) (Applied Science Publishers, NY, 1981).
25. B. S. Majumdar and S. J. Burns, "Crack-Tip Shielding - An Elastic Theory of Dislocations and Dislocation Arrays Near a Sharp Crack," Acta Metallurgica 29 (4), 579 (1981).
26. R. Thomson and F. McClintock, "Fracture Criterion for Dislocation Shielded Cracks," private communication.
27. J. R. Rice and R. Thomson, "Ductile Versus Brittle Behavior of Crystals," Philosophical Magazine 29, 73 (1974).

28. K. Sieradski, private communication.
29. R. A. Oriani and P. H. Josephic, *Acta Metallurgica* 22, 1065 (1974).
30. B. S. Majumdar and S. J. Burns, "Griffith Crack Shielded by a Distribution of Dislocations," to be published.
31. S. M. Ohr and J. Narayan, "Electron Microscope Observation of a Shear Crack in Stainless Steel Single Crystals," *Philosophical Magazine A* 41, 81 (1980).
32. N. J. Petch, *Iron and Steel Institute* 173, 25 (1953).
33. N. J. Petch, "The Lowering of Fracture Stress Due to Surface Adsorption," *Philosophical Magazine* 1, 331 (1956).
34. H. D. Solomon and L. F. Coffin Jr., "Effects of Frequency and Environment on Fatigue Crack Growth in A286 at 1100°F," in Fatigue at Elevated Temperatures, ASTM STP 520 (American Society for Testing and Materials, 1973), p. 112.
35. R. L. Stegman and P. Shahinian, "Effect of Temperature on the Fatigue of Nickel at Varying Oxygen Pressures," in Fatigue at High Temperatures, ASTM STP 459 (American Society for Testing and Materials, Philadelphia, PA, 1969).
36. H. H. Smith, P. Shahinian, and M. R. Achter, "Fatigue Crack Growth Rates in Type 316 Stainless Steel at Elevated Temperatures as a Function of Oxygen Pressure," *Metallurgical Transactions* 245, 947 (1969).
37. S. J. Gregg, The Surface Chemistry of Solids (Rhinehold Publishing Company, NY, 1961).
38. R. M. Pelloux and J. S. Huang, "Creep-Fatigue-Environment Interactions in Astrology," Creep-Fatigue-Environment Interactions, Proceedings of TMS-AIME Meeting, Milwaukee, WI (Metallurgical Society of AIME, 1980).
39. R. C. Donat, T. Nicholas, and L. S. Fu, "An Experimental Investigation of Creep Crack Growth in IN100," presented at the 13th National Symposium of Fracture Mechanics, Philadelphia, PA, June 1980. To be published in a Special Technical Publication by the American Society for Testing and Materials.
40. S. J. Hudak, Jr., A. Saxena, R. J. Bucci, and R. C. Malcolm, "Development of Standard Methods of Testing and Analyzing Fatigue Crack Growth Rate Data," AFML-TR-78-40 (Air Force Materials Laboratory, Wright-Patterson Air Force Base, OH, May 1978).
41. H. Bernstein, "A Study of the J-Integral Method Using Polycarbonate," AFWAL-TR-81-4XXX (Air Force Wright Aeronautical Laboratories, Wright-Patterson Air Force Base, OH, 1981).

42. J. Ahmad, "Two Dimensional Linear Elastic Analysis of Fracture Specimens - User's Manual of a Finite Element Computer Program," AFWAL-TR-80-4008 (Air Force Materials Laboratory, Wright-Patterson Air Force Base, OH, February 1980).
43. J. Ahmad and N. E. Ashbaugh, "Finite Element Analysis of Some Full- and Partial-Ring Crack Propagation Test Specimens," to be published as an Air Force Wright Aeronautical Laboratories Technical Report.
44. T. J. Rudolphi, "An Integral-Equation Solution for a Bonded Elastic Body with an Edge Crack; Mode I Deformations," AFML-TR-78-113 (Air Force Materials Laboratory, Wright-Patterson Air Force Base, OH, July 1978).
45. N. E. Ashbaugh, "Material Evaluation: Part I - Mechanical Property Testing and Materials Evaluation and Modeling," AFML-TR-79-4127 (Air Force Materials Laboratory, Wright-Patterson Air Force Base, OH, September 1979).
46. R. P. Wei and R. L. Brazill, "An Assessment of AC and DC Potential Systems for Monitoring Fatigue Crack Growth," presented at the ASTM Symposium, Pittsburgh, PA, October 29-30, 1979.